C_{80} Endohedral Fullerenes: Rearranging Atoms in a Magnetic Field and Exploring the Interplay of their Spins with Subkelvin Magnetometry and X-rays

---

Dissertation

zur

Erlangung der naturwissenschaftlichen Doktorwürde
(Dr. sc. nat.)

vorgelegt der

Mathematisch-naturwissenschaftlichen Fakultät

der

Universität Zürich

von

Aram Kostanyan
aus Armenien

Promotionskommission

Prof. Dr. Thomas Greber (Vorsitz)
Dr. Cinthia Piamonteze
Prof. Dr. Jürg Osterwalder
Prof. Dr. Andrey Zheludev

Zürich, 2018

Abstract

Endohedral fullerenes are nanometer-sized molecules that consist of carbon cages with atoms or molecules inside. These endohedral units may behave as single atom magnets and are candidates for molecular spintronics and quantum computing.

Properties of nitride cluster fullerenes of type $R_3N@C_{80}$ (R = Ho, Dy, Tb, Gd, Lu, Sc) were studied by means of subkelvin magnetometry, X-ray magnetic circular dichroism (XMCD), and X-ray absorption spectroscopy (XAS).

The ground state of the spins of the paramagnetic rare earth atoms in the endohedral cage was modeled with pseudospins. This model is used to describe the field dependent magnetization of endofullerene ensembles and allows to extract the magnetic moment, and the magnetic coupling of the endohedral atoms.

For the case of $HoLu_2N@C_{80}$, the endohedral unit $HoLu_2N$ can be oriented in a magnetic field. The Ho magnetic moment is fixed parallel to the Ho-N axis and transfers the magnetic torque of an external magnetic field to the endohedral unit which in turn may rearrange. Cooling the sample with different rates in different applied magnetic fields allows the determination of an activation energy and an attempt frequency for the hopping motion of the endohedral unit.

The element specific magnetization is measured utilizing XMCD. This allows untangling the contributions of each atomic species of $Dy_2GdN@C_{80}$ in the total magnetic moment measured with a superconducting quantum interference device (SQUID).

Utilizing alternating current (AC) susceptometry and time-dependent direct current (DC) magnetization measurements, the magnetization lifetimes τ of the endofullerenes were measured for different temperatures down to 400 mK as obtained with a ^{3}He refrigerator and applied magnetic fields. From the temperature and field dependence of τ, different relaxation pathways were determined for $HoLu_2N@C_{80}$ and $Tb_2ScN@C_{80}$.

Zusammenfassung

Endofullerene sind Moleküle in der Größenordnung eines Nanometers, welche aus einer endohedralen Einheit (einzelnen Atomen oder Molekülen) und einem, sie umschließenden, Kohlenstoffkäfig bestehen. Die endohedralen Einheiten können sich wie monoatomare Magnete verhalten und sind geeignete Kandidaten für die Anwendung in molekularen Spintroniken und Quantencomputern.

Die Eigenschaften der Nitridgruppenfullerene vom Typus $R_3N@C_{80}$ ($R =$ Ho, Dy, Tb, Gd, Lu, Sc) wurden mittels Subkelvinmagnetometrie in einem angelegten magnetischen Feld, zirkularem magnetischem Röntgendichroismus (XMCD) und Röntgenabsorptionsspektroskopie untersucht (XAS).

Der Grundzustand des Spins der paramagnetischen Seltenen Erden innerhalb des endohedralen Käfigs wurde modelliert. Dieses Modell wurde verwendet um die feldabhängige Magnetisierung der gesamten Endofullerene zu beschreiben und das magnetische Moment der Atome zu extrahieren.

Für das Endofulleren $HoLu_2N@C_{80}$ kann die endohedrale Einheit $HoLu_2N$ in einem magnetischen Feld ausgerichtet werden. Das magnetische Moment von Ho ist parallel zu der Ho-N Achse fixiert und überträgt das magnetische Drehmoment eines externen magnetischen Feldes auf die endohedrale Einheit, welche im Gegenzug die Atome neu anordnen kann. Durch Kühlen der Probe, bei verschiedenen Kühlraten und magnetischen Feldern können Aktivierungsenergie und Frequenzfaktoren der sprunghaften Bewegung der endohedralen Einheit innerhalb des Kohlenstoffkäfigs bestimmt werden.

Die elementspezifische Magnetisierung wird mit XMCD gemessen. Dadurch konnte das mit einer Supraleitenden Quanten-Interferenz Apparatur (SQUID) gemessene gesamte magnetische Moment von $Dy_2GdN@C_{80}$ in die Einzelbeiträge separiert werden.

Die Magnetisierungslebensdauern τ der Endofullerene für verschiedene Temperaturen (bis hin zu $T = 400$ mK) wurden mittels Wechselstrom (AC)-Suszeptometrie und zeitabhängigen Gleichstrom (DC)-Magnetisierungsmessungen gemessen. Aus Temperatur und Feldabhängigkeit von τ konnten verschiedene Relaxationspfade ermittelt werden.

Contents

1. Introduction

The constant development of silicon-based electronics led to the miniaturization of electronic devices. In 1965 Moore predicted the rate of the miniaturization which states that every two years the number of transistors on a semiconductor chip will double [1]. This law did hold until 2015 where the limits of classical physics were met [2]. The integrated circuits reached several nanometers in size which halted further size reduction due to quantum effects and heat dissipation problems. To continue innovations, alternative concepts to the silicon-based transistors are required. The search started at the end of the 20th century.

Since the 1970s there was a growing interest in organic magnetic materials which later focused towards single molecules [3]. Molecules have several advantages over nanoparticles; they are more reproducible in their physical and magnetic properties. Furthermore, from molecules, single crystals can be formed and studied.

Bulk magnets consist of magnetic domains on the order of a micrometer. The magnetism is governed by the interaction between a large number of spins. Nanoparticles fall in-between bulk magnets and molecules regarding size ($50-200$ nm) and properties. They still exhibit an interaction between individual spins but are small enough to consist of only one domain. Molecules are tiny structures (≈ 1 nm) with enough complexity for tuning. They can be studied as single molecules or in ensembles of a considerable number as presented in this thesis.

Single-molecule magnets (SMMs) are characterized by superparamagnetic behavior, meaning slow magnetization relaxation and an opening of hysteresis below a blocking temperature. The first molecule characterized as an SMM was $\mathrm{Mn_{12}ac}$ ($[\mathrm{Mn_{12}O_{12}(CH_3COO)_{16}(H_2O)_4}]$) [4–8]. The twelve manganese atoms form an $S = 10$ ground state with an anisotropy barrier of 61 K. In principle, the unique properties of SMMs can be used for novel methods of computing like quantum computing.

Quantum computers have been demonstrated by Shor and Grover to outperform classical computers in factoring numbers and searching a database [9, 10]. Large-number factoring is the basis of today's encryption standards. A classical computer needs in average $\log_2 N$ queries to find an entry out of N entries whereas this task can be done in one single query by a quantum computer. Theoretically, it was shown in the example of Fe_8 and Mn_{12} that molecular magnets could be used for quantum computing [11]. Grover's algorithm requires only a superposition of the single-particle quantum states [12] which is already implemented [13]. SMMs are also candidates in applications for spintronics and high-density storage devices [14].

SMMs, nanometer-sized magnets containing one or several magnetic moments, allow for a high degree of customization by choosing the components. Typically, there are three main parameters to categorize an SMM. First, the highest temperature where hysteresis is still visible, the blocking temperature. Second, the coercive field which is the field value where the magnetization of the hysteresis crosses zero magnetization. This determines whether its a hard or soft magnet. Third, the magnetization reversal lifetime which is influenced by multiple factors.

Endohedral fullerenes, also called endofullerenes, are nanometer-sized molecules that comprise atoms or molecules in a carbon cage. The first endofullerene, reported, was $La@C_n$ [15, 16], following the discovery of the first fullerene C_{60} in 1985 [17]. The name fullerene credits the architect Buckminster Fuller as it resembles his geodesic domes. Endofullerene research led to the discovery of many different types of fullerenes some of which are shown in Fig. 1.1. Although the production price of endofullerenes is high—Designer Carbon Materials, Oxford University spin-off, in 2015 sold its first 200 μg ($\approx 10\times^{17}$ molecules) of the material, for £22,000—quantum computers do not require so many molecules. A modern CPU contains $\approx 10^{10}$ transistors.

In this thesis I will concentrate on the family of nitride cluster fullerenes (NCFs) with the characteristic formula $R_3N@C_{2n}$ (R = Sc, lanthanides, etc.; $2n = 68 - 96$), only the C_{80} cage for our case [18–20]. NCFs are remarkable in their properties, neither the carbon cage nor the endohedral unit is stable on its own, but together they form a very stable structure. The cage provides chemical, mechanical and electrostatic isolation. The encapsulated metal ions adopt a trivalent state. The central nitrogen atom and the carbon cage adopt -3 and -6 nominal charge, respectively.

From the considerable amount of possible combinations of atoms of the endohedral unit, we concentrated our attention on four paramagnetic rare earth ions: Gd, Tb, Dy, Ho. The criterion was to have the largest magnetic moment with respect to the R-N axis for the latter three atoms.

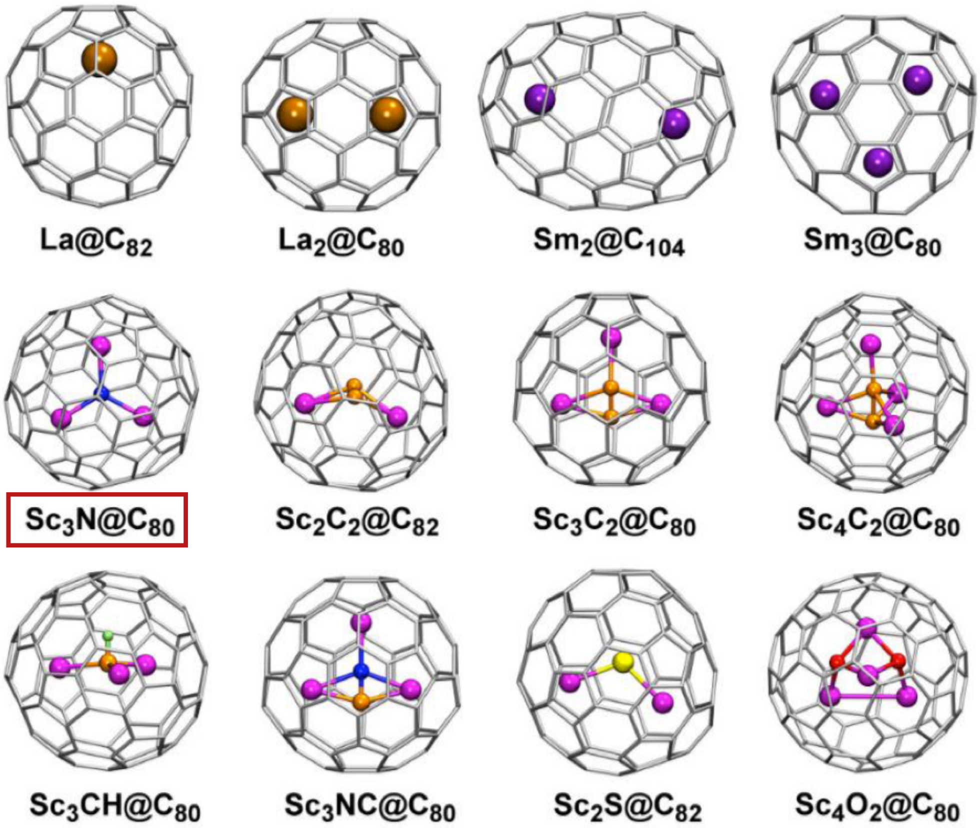

Figure 1.1. The varieties of endohedral fullerenes. The type of fullerene studied in this thesis is marked in red. Image courtesy: Alexey Popov.

What makes lanthanides so interesting to study is the structure of their 4f shell. The spin-orbit coupling in the open 4f shell is significantly larger than the ligand field splitting in contrast to the d-shell of the transition metals. Previous studies on lanthanide endofullerenes demonstrate the unique properties of the 4f shell [21–24].

An outstanding example is the complex of Dy based endofullerenes $\mathrm{Dy}_n\mathrm{Sc}_{3-n}\mathrm{N@C}_{80}$, where n = 1, 2, 3. In this example, the tunability of the magnetic properties of endofullerenes was demonstrated. All three of them show distinct magnetic properties and have different magnetic ground states. The endohedral unit with only one paramagnetic ion Dy $n = 1$ shows magnetization relaxation in zero field which was assigned to quantum tunneling. For $n = 2$ the ferromagnetic coupling of the two Dy ions hinders quantum tunneling and results in remanence of the magnetization. The third molecule, $n = 3$, shows the simplest realization of a frustrated, ferromagnetically coupled ground state [24].

Below follows a brief outline of the thesis. The experimental techniques and instrument along with the theoretical background of possible magnetization relaxation pathways are described in Chapter 2. The modeling of magnetization of endofullerenes for the static and time-dependent kinetics is shown in Chapter 3.

Chapter 4 describes in detail the properties of $HoLu_2N@C_{80}$ along with $Ho_2LuN@C_{80}$ and $HoSc_2N@C_{80}$. The possibility of orienting the endohedral $HoLu_2N$ unit in a magnetic field is discussed in the paper attached at the end of the chapter. Careful field cooling experiments allow the extraction of an energy barrier and attempt frequency for the endohedral rotation. Before that, the field-dependent magnetization for the endofullerenes is discussed along with the magnetization lifetime τ which were extracted utilizing AC susceptometry. From the temperature dependence of τ's possible magnetization relaxation pathways can be determined. The inferred relaxation processes for $HoLu_2N@C_{80}$ were compared with previous studies on $HoSc_2N@C_{80}$.

In Chapter 5 the effects of the interaction of different paramagnetic species in an endofullerene are studied on the example of $Dy_2GdN@C_{80}$ where Dy has strong magnetic anisotropy in contrast to isotropic Gd. The contribution of each of the species is extracted through the element specific magnetization employing X-ray circular magnetic dichroism (XMCD) at the SLS (Swiss Light Source) and compared to the integral magnetization measured with SQUID magnetometer. The magnetization curves show a hysteresis at subkelvin temperatures. The lowest temperature was possible to achieve thanks to the state of the art ^{3}He refrigerator. Utilizing AC susceptometry and time-dependent magnetization measurements, the magnetization lifetime τ was extracted.

In Chapter 6 the interaction of paramagnetic ions of the same species is studied for $Tb_2ScN@C_{80}$. Furthermore, the difference with $Dy_2ScN@C_{80}$ revels the properties of Kramer's ion Dy. The comparison of field dependent magnetization measured using XMCD and SQUID magnetometry is shown. The dynamics of magnetization for $Tb_2ScN@C_{80}$ is studied through AC susceptometry and time-dependent magnetization measurements in the temperature range from 400 mK to 30 K.

2. Methods and Laboratories

2.1. Synthesis of Endohedral Fullerenes

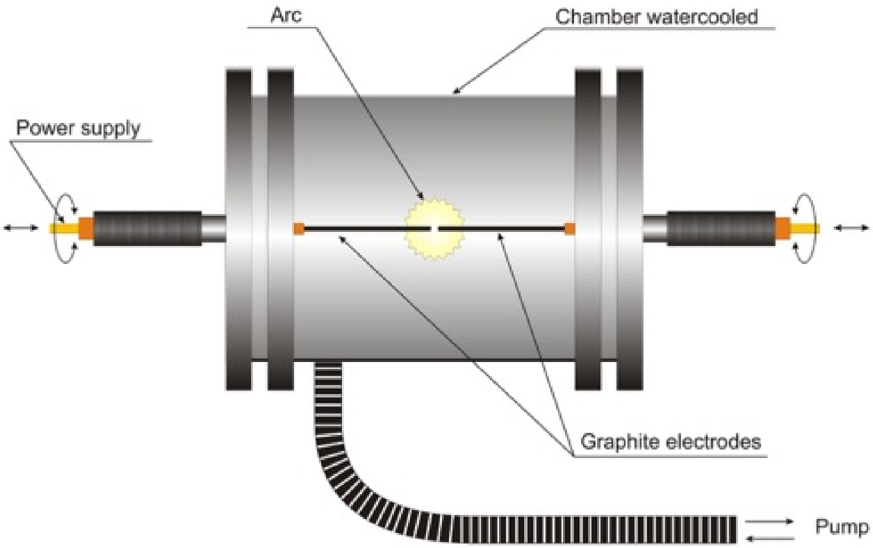

Figure 2.1. Generator for synthesizing endohedral fullerenes. Image courtesy: Alexey Popov.

Below follows a brief description of the synthesis of endofullerenes. I did not perform the synthesis myself. The fullerenes were provided from our collaborators in IFW Dresden: the group of Alexey Popov, especially thanks to the PhD student Christin Schlesier.

The synthesis of endofullerenes can be divided into three main strategies [25]. First, vaporization of the precursor materials for direct synthesis which is performed implementing various methods: laser ablation [15, 16], arc discharge [26], resistive heating [27], radio frequency furnace [28], and plasma-torch [29]. Second, implantation of atoms through the walls of the empty fullerenes [29]. Third, chemically opening the empty cages [30]. However, not all cages are stable without the endohedral unit [25]. The endofullerenes studied in this thesis were prepared with Krätschmer-Huffman arc-discharge method as it provides highest yields while still being relatively simple [31].

The essence of the Krätschmer-Huffman is the following. The hollow graphite electrodes are filled with desirable precursor materials and are placed in the generator shown in Fig. 2.1. The endofullerenes are produced in the arc between the carbon electrodes. The yields of specific endofullerenes can be controlled by tuning the relative quantities of precursors and conditions inside the generator.

The arc results in soot full of different types of empty cages, endofullerenes, and other carbon structures. The endofullerenes extracted from the soot are separated to achieve the highest purity, only one cage size and one type of endohedral unit. The most powerful method used for separation is the high-performance liquid chromatography (HPLC) [32].

2.2. SQUID Magnetometry and AC Susceptometry

2.2.1. MPMS 3 with ^{3}He Refrigerator

Figure 2.2. MPMS 3 SQUID magnetometer [33].

Quantum Design's MPMS 3 (Magnetic Property Measurement System) is a modern SQUID (Superconducting Quantum Interference Device) magnetometer with temperature control that allows continuous and smooth operation over a wide temperature range (1.8 K to 400 K) and several measurement methods. Three different measurement methods are possible, two DC: DC scan mode and VSM (Vibrating Sample Magnetometer) mode, and one AC susceptibility mode.

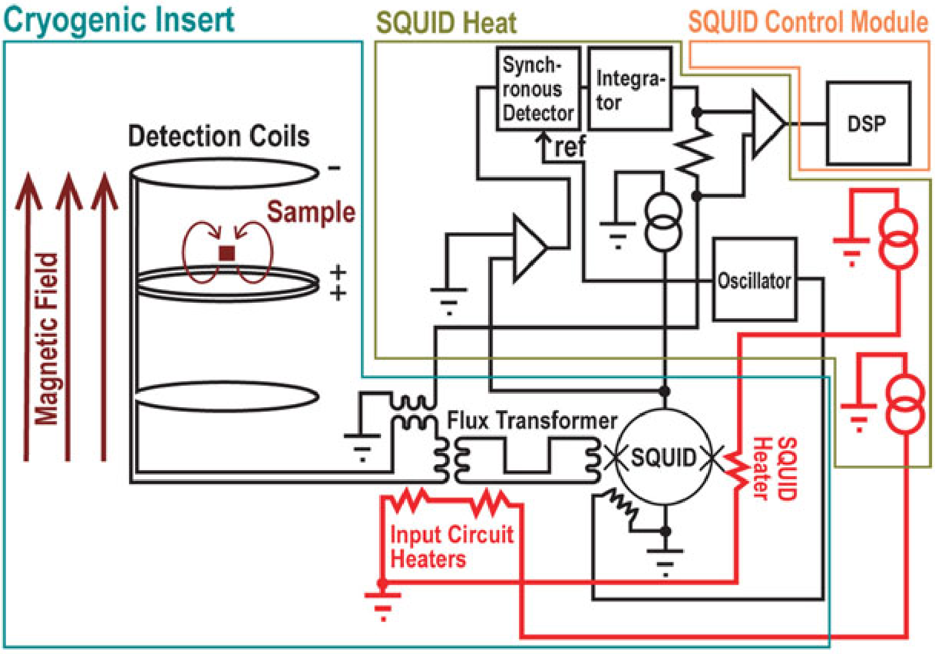

Figure 2.3. The simplified diagram of the SQUID detection system. Image source: instrument manual.

Figure 2.3 shows the simplified schematics of the detection system. The current in the detection coils is inductively coupled to the SQUID sensor which can be viewed as an extremely sensitive current-to-voltage converter. Heaters are mounted on both the detection coil and the SQUID circuits that allow increasing the temperature above the critical point to eliminate standing currents.

The SQUID sensor is biased with a slightly larger current than double the critical current I_c [34]. A change in the magnetic flux through the SQUID sensor induces a change in the voltage across the SQUID's Josephson junction. This voltage is used for the feedback to null the current in the detection coils. The SQUID voltage is inferred from the feedback current. The instrument's electronics amplify and digitize the SQUID voltage.

The detection coils have a configuration of a second-order gradiometer. This specific shape allows the SQUID to be non-responsive to uniform and linear magnetic field gradients. The dimensions of the coils are 17 mm in diameter and 8 mm in height.

The most sensitive magnetometry method available in the present system is the VSM mode. The sample vibrates with a frequency $\nu = 14$ Hz in the center of detection coils shown in Fig. 2.3. The frequency of 14 Hz was chosen to increase the sensitivity considering the mechanical vibrations of the instrument. A time dependent SQUID signal V is generated

$$V(t) = AB^2 \sin^2 \omega t$$

where A is a scaling factor, B is the amplitude of the sample vibration. This leads to a frequency of 2ω for the voltage V and thus a lock-in amplifier can be applied to isolate the signal.

The sensitivity of the VSM mode is $< 8 \times 10^{-11}$ A m^2 ($< 8 \times 10^{-8}$ emu), with less than 10 s averaging time, which corresponds to 8.6×10^{12} Bohr magnetons (μ_B). This measurement method will be referred to as DC.

DC scan mode simply scans the sample across the center of the detection coils. The moment is extracted by fitting an empirical function to the $m(z)$ signal where z is the sample position. This DC measurement method has a sensitivity of $< 6 \times 10^{-10}$ A m^2 ($< 6 \times 10^{-7}$ emu) which is less than VSM.

AC susceptibility measurements incorporate an oscillating magnetic field with the detection of the signal using the SQUID. The AC susceptometry has a frequency range from 0.1 Hz to 1000 Hz with amplitudes from 0.1 Oe to 10 Oe. The largest AC field amplitude is frequency dependent.

To perform any type of measurements, the sample should be centered, positioned at the center of the detection coils (Fig. 2.3). A real centering scan is shown in Appendix A.

Helium-3 Refrigerator

The lowest achievable temperature of MPMS3 is decreased by the incorporation of a so-called continuous flow Helium-3 refrigerator. The ^{3}He insert allows a temperature range from 400 mK to 2 K with a lifetime of 65 hours at the lowest temperature. The lifetime of the shot is temperature dependent and decreases with increased temperature.

The refrigerator includes a special insert which completely isolates ^{3}He and ^{4}He operation areas avoiding the possible mixing of the two gases. The ^{3}He sample holder is shown in Fig. A.3. The low temperatures are achieved in two steps. First, the ^{3}He gas is condensed to a liquid form in the ^{3}He sample area via the cryopumping effect. Next, it is pumped with a turbo-molecular pump which leads to evaporation of the liquid ^{3}He and the temperature decreases.

2.2.2. AC susceptibility

AC susceptometry is a technique that gives access to the magnetic susceptibility of the sample, $\mathrm{d}M/\mathrm{d}H$, at zero or a static field H_0 [3]. The primary advantage of this technique is that it allows for the investigation of the magnetization dynamics by varying the frequency ω, first time performed in the 1930s [35]. The AC current with a frequency ω flowing through the coils generates a small AC field h.

The oscillating magnetic field

$$H = H_0 + h\,\cos\omega t \tag{2.1}$$

changes the thermal equilibrium. To achieve this new equilibrium the system needs a time τ. If the frequency of the AC field oscillations is small, $\omega\tau \ll 1$, the isothermal susceptibility χ_T is measured. On the other hand, if $\omega\tau \gg 1$, the system has no time to exchange energy with the thermal bath to reach equilibrium, and the adiabatic susceptibility χ_S is measured. The description of these two extreme cases is easier than for $\omega\tau \approx 1$. The formula for the intermediate regime was proposed by Casimir and du Pré (1938) [36]

$$\chi(\omega) = \chi_S + \frac{\chi_T - \chi_S}{1 + i\omega\tau}. \tag{2.2}$$

If χ_T and χ_S are real, the real χ' and imaginary χ'' components of the susceptibility read:

$$\chi' = \chi_S + \frac{\chi_T - \chi_S}{1 + \omega^2\tau^2}, \qquad \chi'' = \frac{\chi_T - \chi_S}{1 + \omega^2\tau^2}\omega\tau. \tag{2.3}$$

In essence, χ_S may be interpreted as the susceptibility of an isolated system with no thermal dissipation while χ_T corresponds to the susceptibility in equilibrium with phonons.

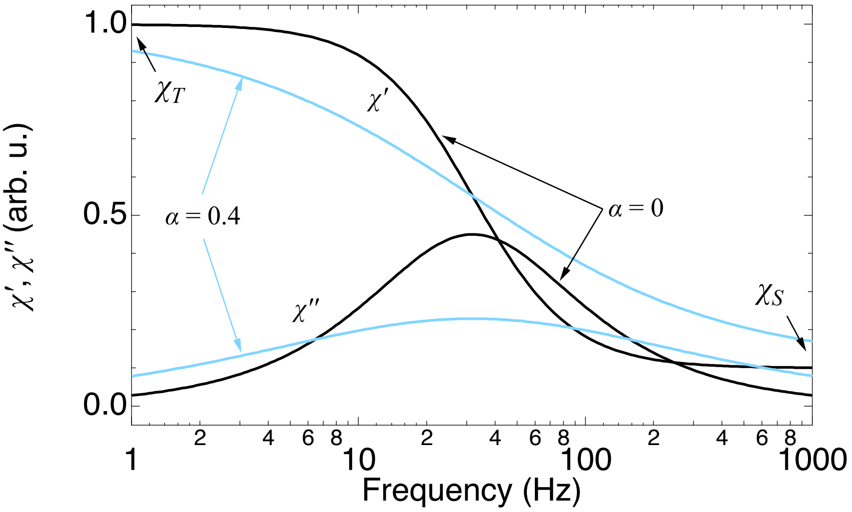

Figure 2.4. Theoretical frequency dependence of the real (in-phase) χ' and imaginary (out-of-phase) χ'' components of the magnetic susceptibility for two different α's. χ_T and χ_S are isothermal and adiabatic limits of the AC susceptibility, respectively.

If the relaxation process is characterized by a distribution of relaxation times τ which may be typical for powder samples of SMMs (single-molecule magnet) an empirical law allows to account for it was given by Cole and Cole [37]:

$$\chi(\omega) = \chi_S + \frac{\chi_T - \chi_S}{1 + (i\omega\tau)^{1-\alpha}} \tag{2.4}$$

and

$$\chi' = \chi_S + (\chi_T - \chi_S)\,\frac{1 + (\omega\tau)^{1-\alpha}\sin(\pi\alpha/2)}{1 + 2\,(\omega\tau)^{1-\alpha}\sin(\pi\alpha/2) + (\omega\tau)^{2-2\alpha}}, \tag{2.5}$$

$$\chi' = (\chi_T - \chi_S)\,\frac{(\omega\tau)^{1-\alpha}\cos(\pi\alpha/2)}{1 + 2\,(\omega\tau)^{1-\alpha}\sin(\pi\alpha/2) + (\omega\tau)^{2-2\alpha}}. \tag{2.6}$$

The wider the distribution of relaxation times τ the larger is α. Figure 2.4 shows the theoretical frequency dependence of the real χ' and imaginary χ'' components of the AC susceptibility. χ'' exhibits a peak with a maximum corresponding to the frequency $\omega\tau = 1$ and approaches zero for $\omega \to 0$ and $\omega \to \infty$ in contrast to χ' which approaches its limiting values χ_T and χ_S. Figure 2.4 also demonstrates the broadening the features for distribution of different τ's corresponding to $\alpha = 0.4$.

The simplest way of extracting the relaxation time τ is using the formula: $\tau = \omega^{-1}$ but as demonstrated in Sec. 4.5 this method is not as accurate as a simultaneous fit of equations 2.5 and 2.6 to χ' and χ'', respectively.

2.3. X-ray Absorption Spectroscopy and X-ray Circular Magnetic Dichroism

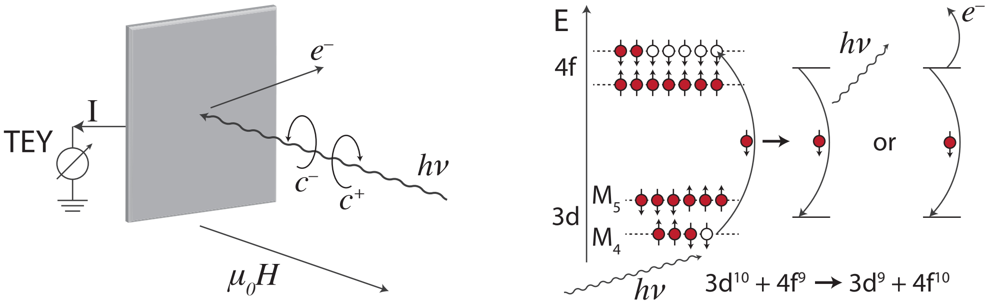

Figure 2.5. Left: Geometry of X-ray absorption spectroscopy. Right: X-ray absorption process with two different relaxation ways: fluorescence or emission of an auger electron.

X-ray Absorption Spectroscopy (XAS) is a widely used technique for analysis of the local chemical state of the atoms by probing core levels. However, it is a demanding technique as synchrotron radiation is required which allows photon energy dependent absorption measurements. Incorporation of circularly polarized light allows the determination of spin and orbital expectation values [38–40]. The absorption intensity depends on the orientation between x-ray angular momentum and the magnetic moment.

Figure 2.5 shows the schematics of the absorption measurements. The X-ray shining on the sample excites an electron from a core level (3d) into an unoccupied level (4f). The excitation is followed by a relaxation process. There are two possible relaxation ways: the excited electron relaxes, and a photon with corresponding energy is emitted (fluorescence), or the relaxation of the excited electron leads to the emission of an Auger electron from higher levels.

The XAS presented in this thesis was studied by measuring the total electron yield (TEY) from a variety of Auger processes.

A compelling method for probing the size and the direction of the magnetic moment of atoms with chemical sensitivity is X-ray magnetic circular dichroism (XMCD).

The maximum of the dichroism is when the x-ray angular momentum is parallel or antiparallel to the magnetic moment. XMCD requires spin-orbit coupling, as the photon angular momentum does not directly couple with the electron spin but is mediated via orbital angular momentum. It is constructed by the subtraction of an XAS spectrum with a c^- polarization from XAS with c^+ polarization [41].

2.3.1. X-Treme beamline

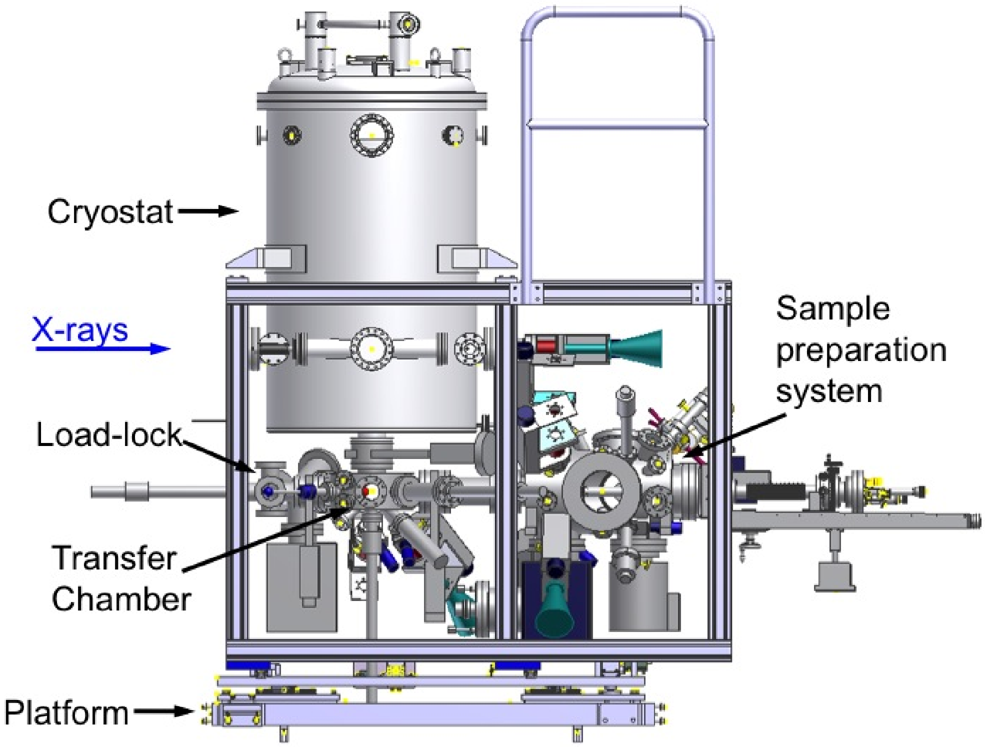

Figure 2.6. X-Treme end station located at Swiss Light Source (SLS), Paul Scherrer Institute (PSI).

The X-Treme (X-ray absorption spectroscopy at high magnetic fields and low temperature) beamline is located at X07MA position of the Swiss Light Source (SLS) synchrotron at the Paul Scherrer Institute (PSI). The illustration of the end station is shown in Fig. 2.6 showing the measurement chamber with the cryostat, load-lock, transfer chamber and the sample preparation system. It is capable of producing high flux soft X-rays with various polarizations (circular plus, circular minus and linear polarization in any angle between 0 and 90 degrees) from an Apple-II undulator source [42]. The end station provides ultra-high vacuum (UHV) along with a 2D vector magnet with a maximum of 7 T along the beam and a lowest temperature of 2 K. The provided energy range is between 400 and 2000 eV with 0.1 eV energy resolution at 700 eV. The flux at the sample is typically 10^{12} photons/s at 700 eV.

2.3.2. Data Treatment

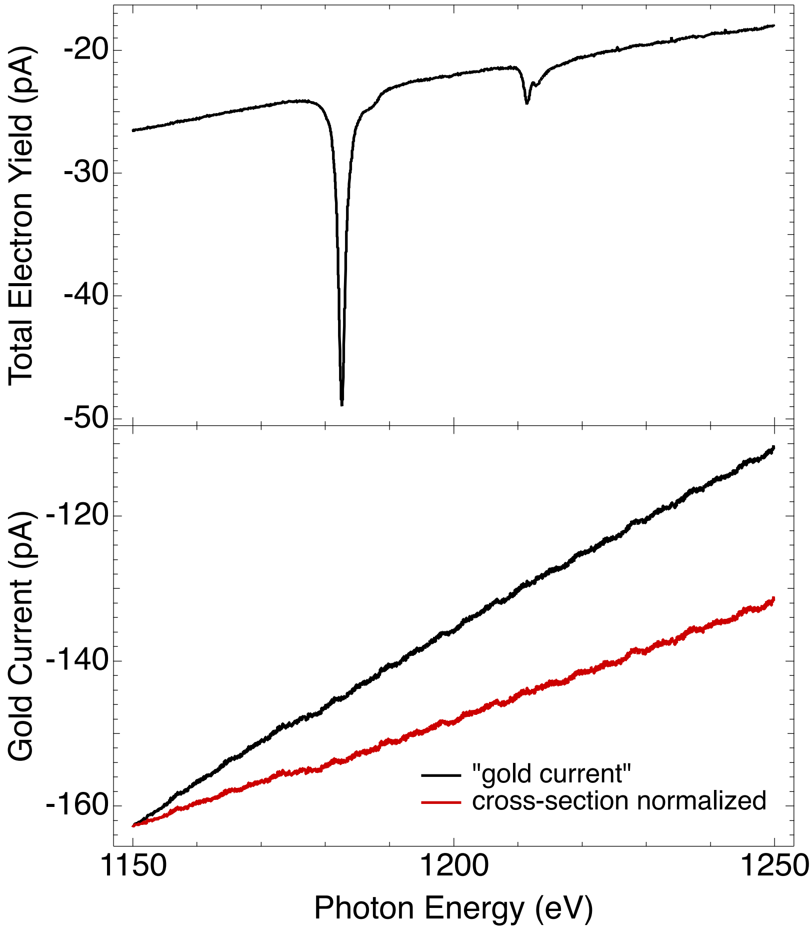

Figure 2.7. Top: Total electron yield (TEY) measured on $Dy_2GdN@C_{80}$ on an Al substrate. Bottom: Gold mesh current before and after cross-section normalization, where the relative cross section at 1150 eV was set to one.

The measured total electron yield (TEY) contains the information about the absorption properties of the sample but is also affected by other sources not originating from the sample. Typically the X-ray flux is not constant during absorption measurements. It depends on several factors: the X-ray energy, the ring current top-ups induce a zig-zag in the TEY signal, the undulator and monochromator settings.

The TEY is normalized by the current measured on a gold mesh which is positioned after the last mirror on the X-ray path. However, due to photon energy dependence of the cross section of gold another systematic error for the photon flux is introduced.

This can be eliminated by normalizing the gold mesh current with the gold cross section as it can be obtained from NIST [43].

Figure 2.7 shows the total electron yield (TEY) measured on $Dy_2GdN@C_{80}$ on an Al substrate and the gold mesh current as a function of photon energy before and after the cross section normalization. As seen from the graph, the consideration of the Au cross section changes for the present example the nominal value of the flux by about 25%/100 eV. Therefore, the cross section correction is crucial for sum rule analysis performed on lanthanide $M_{4,5}$ edges (Chapter 5). With the Au cross section normalization applied the expectation value of 0 for the orbital moment $\langle L_z \rangle$ of Gd^{3+} could be obtained.

The normalization of the TEY by the corrected gold mesh current is followed by subtraction of the background. The background is subtracted by fitting a polynomial with a data mask to the measured spectra. The data mask excludes the absorption peaks from the fits, so only the background is fitted.

The XAS spectra are measured with the on-the-fly mode which measures the TEY while continuously changing photon energy. This leads to different energy intervals for every spectrum. The measured signal may also contain noise which can be decreased by averaging multiple data point into one. Therefore, after the background subtraction, the spectra are interpolated to a common energy grid by interpolation of the data with pre-averaging that allows the addition and subtraction of two different spectra. The essence of pre-averaging, if the density of initially measured absorption spectra is larger than that of required for further analysis, is that the whole energy range of measurement is divided into small parts with equal intervals and the data points in that interval are averaged to a single point corresponding to that interval. Afterward, these average points per interval are used for interpolation with desired energy step. The interval size of averaging is taken smaller than the desired energy step for interpolation.

Typically, more than one absorption spectra are measured with the same parameters for the same sample. In this case, all the curves are used for pre-averaging before the interpolation which is done after normalization and background subtraction.

Figure 2.8 shows the X-ray absorption spectra (XAS) and X-ray magnetic circular dichroism (XMCD) of endohedral Gd in $Dy_2GdN@C_{80}$ for circularly plus and minus polarized light after the analysis outlined above. The measurements were done at $T = 2$ K at X-treme beamline, SLS (Sec. 2.3.1). The total absorption spectra I_{tot} is constructed from the sum of the two polarities I^+ (red) and I^- (blue) and the

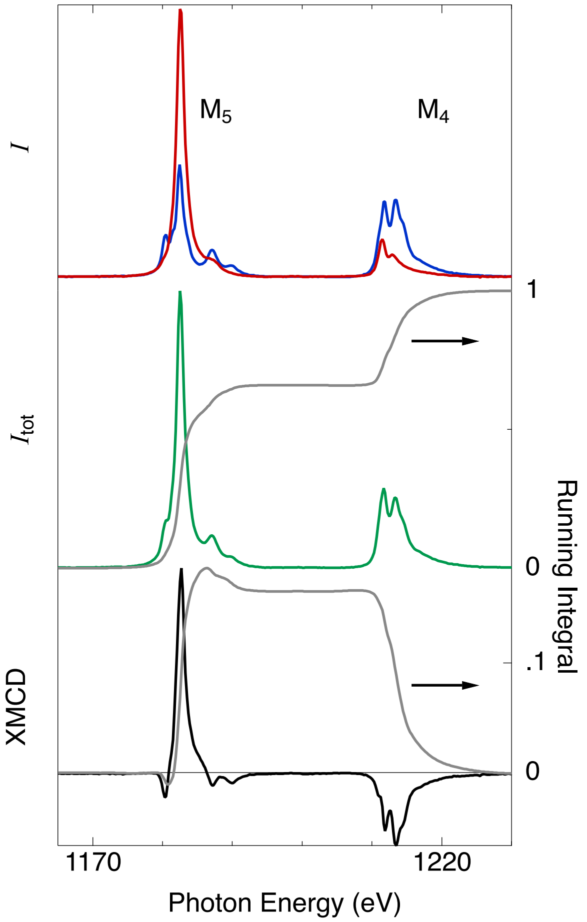

Figure 2.8. Top: Polarization-dependent X-ray absorption spectra (XAS) of Gd in $Dy_2GdN@C_{80}$—background subtracted and normalized TEY—I^+ (red) and I^- (blue); measured at the Gd $M_{4,5}$-edges at 6.5 T. Middle: Sum of XAS of both X-ray helicities from the top panel, I_{tot}. Bottom: XMCD spectrum, $I^+ - I^-$. The grey lines are the running integrals for corresponding spectra used for sum rule analysis.

XMCD is $I^+ - I^-$. In the next section, these spectra will be used for calculation of the expectation values of orbital $\langle L_z \rangle$, total spin $\langle S_z \rangle$ and magnetic dipole $\langle T_z \rangle$ operators.

2.3.3. Sum Rule Analysis

The spin and angular momenta can be separately determined form the XMCD spectra because XMCD depends on the spin-orbit coupling. Here the relation of the XMCD signal integrated over of a spin-orbit-split core-level edge with the ground-state expectation values of the orbital $\langle L_z \rangle$, total spin $\langle S_z \rangle$ and magnetic dipole $\langle T_z \rangle$ operators is shown [38, 39]. The XMCD spectroscopy can be viewed as shell specific probe of the magnetic moment of the valence electrons. The ground-state expectation value of the orbital angular momentum $\langle L_z \rangle$, where z is parallel to the propagation direction of x-rays, implicitly gets:

$$\frac{A^{\mathrm{XMCD}}}{(3/2)A^{\mathrm{tot}}} = \frac{1}{2}\,\frac{l(l+1)+2-c(c+1)}{l(l+1)(4l+2-n)}\,\langle L_z \rangle \tag{2.7}$$

where l and c are the azimuthal quantum numbers of the valence and core shells respectively, n is the number of electrons in the valence shell, A^{tot} and A^{XMCD} are the areas, the running integrals over the two spin-orbit split edges corresponding to the total absorption and XMCD, respectively (Fig. 2.8).

For example, for the $M_{4,5}$ edges, the excitations from 3d core level to 4f valence shell, of Gd^{3+} $4\mathrm{f}^7$ the above mentioned constants are: $l = 3$ (4f), $c = 2$ (3d) and $n = 7$.

The ground-state expectation value of the spin-depend part can be expressed as:

$$\begin{aligned}\frac{A^{\mathrm{XMCD}}_{M_5} - A^{\mathrm{XMCD}}_{M_4}(c+1)/c}{(3/2)A^{\mathrm{tot}}} = &\ \frac{l(l+1)-2-c(c+1)}{3c(4l+2-n)}\,\langle S_z \rangle \\ &+ \frac{l(l+1)[l(l+1)+2c(c+1)+4]-3(c-1)^2(c+2)^2}{6lc(l+1)(4l+2-n)}\,\langle T_z \rangle\end{aligned} \tag{2.8}$$

where $A^{\mathrm{XMCD}}_{M_5}$ and $A^{\mathrm{XMCD}}_{M_4}$ ($A^{\mathrm{XMCD}} = A^{\mathrm{XMCD}}_{M_5} + A^{\mathrm{XMCD}}_{M_4}$) are the areas, running integrals over the XMCD of M_5 and M_4 edges respectively (Fig. 2.8).

The $M_{4,5}$ edges of lanthanides. These systems closely follow the LSJ coupling of the Hund's rule ground state. Thus the $\langle T_z \rangle$ can be analytically calculated [44]:

$$\begin{aligned}\langle T_z \rangle = &\ \langle M \rangle\,(l-n+1/2) \\ &\times \frac{3(S-J)^2(S+J+1)^2 - L(L+1)[L(L+1)+2S(S+1)+2J(J+1)]}{2(2l+3)(2l-1)(2L-1)SJ(J+1)}\end{aligned} \tag{2.9}$$

and

$$\langle S_z \rangle = \langle M \rangle \frac{J(J+1) + S(S+1) - L(L+1)}{2J(J+1)}, \tag{2.10}$$

where L, S and J are total orbital angular momentum quantum number, total spin angular momentum, and total angular momentum quantum number, respectively.

The ratio of $\langle S_z \rangle$ to $\langle T_z \rangle$ is constant within LSJ theory, and they can be separated.

However, this analytical expression is not precise enough for our needs. The error in the sum rule analysis is calculated for lanthanides [40]. The deviation from the sum rules for Ce is $\approx 60\%$ and increases with the number of electrons for less than half-filled $4f$ shell. The deviation sharply decreases for half and more filling of the $4f$ shell. The deviation is smaller than 10%. For calculations of the sum rules used in this thesis the ratio of $\langle S_z \rangle$ to $\langle T_z \rangle$ is taken from the calculation s performed in the literature [40]. In Chapter 5 the sum rule analysis is presented with and without this correction.

2.4. Magnetization Relaxation Pathways

This section briefly presents the background of magnetization relaxation pathway. The time constant for reaching the equilibrium macroscopic magnetization of the system in a given direction is called relaxation time [45]. The relaxation time parallel to the direction of a static field is called longitudinal relaxation time T_1 on which we will concentrate our attention in this thesis. We start the discussion of the magnetization relaxation pathways after a brief introduction to the origins of axial asymmetry.

The ligand field of the central nitrogen ion of the endohedral units discussed in this thesis lifts the degeneracy of Hund's ground state. For the lanthanides of interest in the ground state maximum $\pm J_z$ is favored [21, 22, 24]. The ligand induces axial symmetry of the magnetic moment which may point only towards or away from the central nitrogen with an energy barrier separating these two orientations. At zero external magnetic field $\pm J_z$ states are energetically degenerate. The detailed discussion of the magnetic properties of endofullerenes is presented in Sec. 3.

2.4.1. Quantum Tunneling of Magnetization (QTM)

Two main types of systems should be considered. First, systems with an even number of electrons where the mixing of the $\pm J_z$ levels is allowed thus QTM as well. Second, systems with an odd number of electrons, Kramer's ion. For Kramer's ions, the mixing of $\pm J_z$ states and QTM is forbidden. However, in the presence of perturbations (transverse anisotropy, dipolar interactions, or nuclear hyperfine coupling) the mixing of ground states becomes possible so as QTM [46], as seen for $DySc_2N@C_{80}$ [23].

The quantum tunneling process does not require input or release of energy from the interactions with phonon bath to proceed. This leads to the temperature independence of QTM. However, QTM is field dependent as the Zeeman splitting reduces the mixing of the ground state. The following formula is typically used for fitting:

$$\tau^{-1} = \frac{\tau_{\mathrm{QTM}}^{-1}}{1 + BH^2} \tag{2.11}$$

where τ_{QTM} (zero field tunneling time) and B are fitting parameters [47, 48].

If the tunneling between the $\pm J_Z$ levels is hindered (Zeeman splitting, Kramer's ions, etc.), the magnetic moments have to climb over the anisotropy barrier between the $\pm J_Z$ states induced by the ligand field. The equilibrium is reached in an exponential manner with a characteristic relaxation time

$$\tau = \tau_0 \exp \frac{E_A}{k_B T} \tag{2.12}$$

where E_A and τ_0 are the barrier height and the attempt time respectively, k_B is the Boltzmann constant and T is the temperature.

However, if the magnetic moments exhibit time dependent hyperfine or dipolar interactions the time dependent magnetization deviates from exponential and takes the following form [49]:

$$m(t) = m_0[1 - (t/\tau)^{1/2}].$$

2.4.2. Temperature Dependent Relaxation

In contrast to QTM, the below-presented relaxation processes require an exchange of energy with the surrounding (energy is needed to go over the barrier) and there-

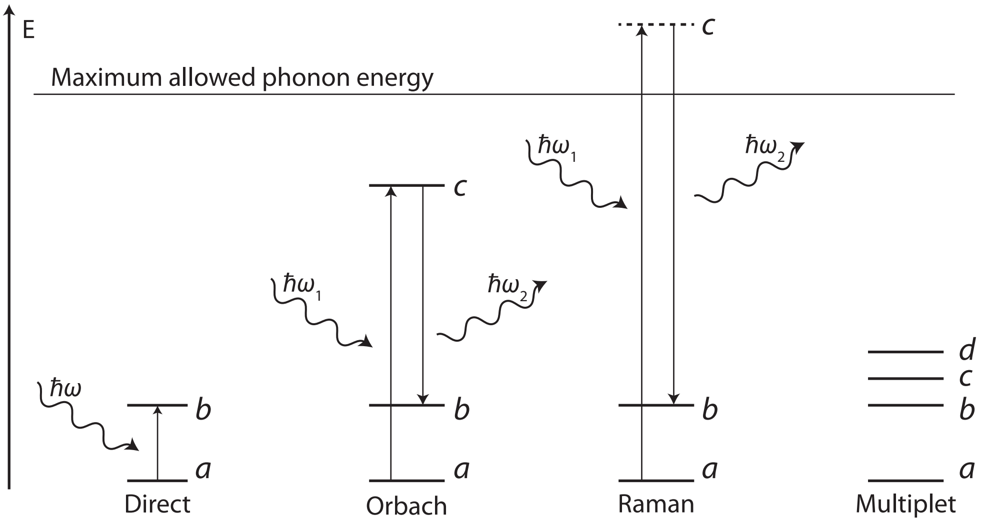

Figure 2.9. Schematics of the energy levels of spin-lattice relaxation processes mediated by absorption or/and emission of a phonon with an energy $\hbar\omega$. a and b are electronic spin ground states between which the relaxation process happens. c is the excited electron state, for Raman, it is larger in energy than the largest allowed phonon level.

fore show temperature dependence. Below is a brief explanation of the following relaxation processes: direct, Raman and Orbach [50–54].

The mechanism of magnetization relaxation was suggested to consist of modulation of the ligand field through the motion of the ions influenced by vibrations [55]. However, as the perturbation is strictly electrical in origin, it cannot act on the spin directly. The interaction is mediated by spin-orbit interaction.

To numerically calculate the influence of distortions of the electrical, ligand field induced by lattice vibrations, Orbach suggested expanding the electric potential in powers of strain about the equilibrium position [46, 56, 57].

2.4.2.1. The Direct Process

A direct transition from initial to final state mediated by emission or absorption of a phonon with the same energy as the level difference as shown in Fig. 2.9. The probability of this process is governed by the first order elements of the expansion of the electric potential. The relaxation rate τ^{-1} is proportional

$$\tau^{-1} \propto \coth(\hbar\omega/2k_BT). \tag{2.13}$$

For non-Kramers ions with degenerate zero-field levels, the energy difference between the initial and final states correspond to the Zeeman splitting:

$$\tau^{-1} \propto H^3 \coth(\mu\mu_0 H/2k_B T) \tag{2.14}$$

or when $(\mu\mu_0 H/2k_B T) \ll 1$, where H is the magnetic field, temperature T, magnetic moment μ, Eq. 2.14 can be approximated by

$$\tau^{-1} \propto H^2 T. \tag{2.15}$$

For Kramers ions with vanishing strain matrix elements at zero-field the admixture of excited states are due to external magnetic field

$$\tau^{-1} \propto H^5 \coth(\mu\mu_0 H/2k_B T) \tag{2.16}$$

or when $(\mu\mu_0 H/2k_B T) \ll 1$ Eq. 2.16 can be approximated by

$$\tau^{-1} \propto H^4 T. \tag{2.17}$$

2.4.2.2. The Two-Phonon Orbach Process

Let us assume, that the magnetic ion has several energy levels as shown in Fig. 2.9, the ground state levels a, b and the excited state c. The energy of the level c is within the allowed phonon frequency range. The transitions between the two low-lying states a and b are mediated through the excited state c. For a spin at level a, it is possible to absorb a phonon, and through a direct process, it can transition to the excited level c with energy Δ. Then the spin can emit another phonon with respective frequency and relax to state b. This is called Orbach process. It is field independent unless field alters the value of Δ. Orbach processes are a result of two subsequent direct transitions. Thus, it is also proportional to the first order expansion of the potential. Typically the transition from a to a higher level c has a smaller probability than the subsequent relaxation to b. The characteristic relaxation time for an Orbach process is:

$$\tau^{-1} \propto \Delta^3[\exp(\Delta/k_B T) - 1]^{-1} \tag{2.18}$$

where the $[\exp(\Delta/k_BT) - 1]^{-1}$ factor is the phonon occupation number or Bose factor. In the limit $\Delta \gg k_BT$, the previous equation can be simplified to

$$\tau^{-1} \propto \exp(-\Delta/k_BT). \tag{2.19}$$

2.4.2.3. The Two-Phonon Raman Process

We consider a two-phonon Raman-type process. The magnetic ion makes a transition between the ground states a and b accompanied by a virtual absorption of a phonon with energy $\hbar\omega_1$ and emission a phonon of energy $\hbar\omega_2$, provided the conservation of energy $|\hbar\omega_1 - \hbar\omega_2| = \hbar\omega$, where $\hbar\omega$ is the energy difference between initial and final states. Physically this means that the lattice vibrations of frequencies ω_1, ω_2 can combine to create a crystal potential vibrating at frequency $\omega = |\omega_1 - \omega_2|$.

Two types of Raman processes are distinguished which are called "first order" and "second order". Their names are coming from the nature of the perturbation involved.

First-order Raman process arises when the second-order expansion of the crystal potential has matrix elements between states a and b.

Second-order Raman process. A phonon causes a 'virtual' transition from one of the ground states to an excited level c. This is followed by another 'virtual' transition from the excited level c down to the other ground state. The transitions are referred to as 'virtual' (unlike the Orbach process) because the energy of the excited level c is outside of allowed phonon frequencies. The two types of Raman transitions are typically hard to distinguish.

For a non-Kramers ion the Raman process has the temperature dependence:

$$\tau^{-1} \propto T^7 \tag{2.20}$$

And for a Kramers ion the relaxation time is

$$\tau^{-1} \propto a_7T^7 + a_9T^9 \tag{2.21}$$

where a_7 and a_9 are proportionality coefficients.

2.4.2.4. Multiplet Ground State

Another important case described by Blume and Orbach is when the excited levels are very close to the ground state levels a and b [58]. In this case, the proportionality of τ can be written as:

$$\tau^{-1} \propto T^5. \tag{2.22}$$

To sum up all the above presented ideas in one relatively simplified formula, the magnetization relaxation time τ may be written as:

$$\tau^{-1} = \frac{\tau_{\mathrm{QTM}}^{-1}}{1 + BH^2} + A_1 H^4 T + A_2 H^2 T + \tau_o^{-1}\, e^{-\Delta_{\mathrm{eff}}/k_B T} + CT^n \tag{2.23}$$

where τ_{QTM} is the zero-field resonant quantum tunneling time, a fitting constant B. The second and third terms correspond to direct scattering for Kramers H^4 and non-Kramers H^2 ions. The fourth term represents the two-phonon Orbach process.

The last term is the temperature dependence of Raman process with typical values of the exponent n:

$n = 7$	non-Kramers doublet
$n = 9$	Kramers doublet
$n = 5$	multiplet with small splitting

3. Modeling the Magnetization

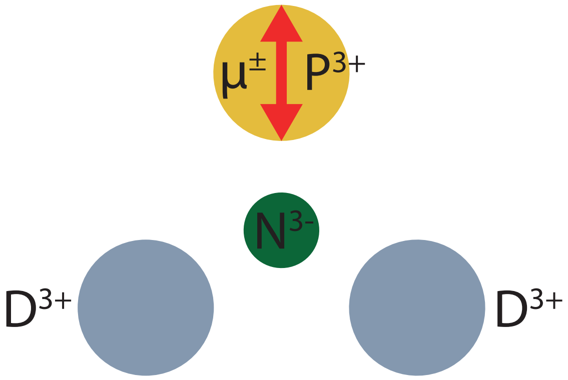

Figure 3.1. Schematic view of the endohedral unit of type PD_2N, where P and D are paramagnetic and diamagnetic ions respectively. The ions are bound to the central nitrogen ion. The up-down arrow indicates the possible directions of the magnetic moment with the field lines of the dipolar field.

In this thesis, ensembles with a large number of molecules ($\approx 10^{17}$) are studied for their magnetic properties as a function of external magnetic field and temperature. The outlined statistical description with pseudospin model (see below) allows the extraction of the magnetic moment μ of the paramagnetic ion with the number of molecules in the ensemble.

In the second part of this chapter, the modeling of in-field cooling for hop-rotation of the endohedral unit is discussed. The extraction of the energy barrier E_A and the attempt frequency ν of the hop-rotation of the endohedral unit is shown [59].

3.1. Pseudospin Model

In this thesis, the magnetic moment $\vec{\mu}$ of endohedral lanthanide ions are studied. The ground state of the paramagnetic ion P in $R_3N@C_{80}$, where R is a rare earth ion that can be a paramagnet P or a diamagnet D (Fig. 3.1), can be described with a "pseudospin" that consists of a total angular momentum of + or $-J_z$, where the z-axis points to the central nitrogen ion. For Tb, Dy and Ho in $R_3N@C_{80}$ J_z assumes its maximum value of 6, 15/2 and 8 that translates to magnetic moments of 9, 10 and 10 μ_B, respectively. The reason for this is the ligand field that lifts the degeneracy of the Hund's ground states $^7F_6$, $^6H_{15/2}$, $^5I_8$. As a ground state, the maximum J_z is favored for these lanthanides [21, 22, 24]. The higher multiplets are separated by an energy of several hundred kelvin [60, 61]. At zero external magnetic field the $\pm J_z$ states are degenerate.

The pseudospin model has been applied to determine the magnetic moments of the ions Dy^{3+} in $DySc_2N@C_{80}$ [21, 24], Ho^{3+} in $HoLu_2N@C_{80}$ [59] and Tb^{3+} in $TbNC@C_x$ [62, 63]. The endohedral unit of the first two molecules consists of a single paramagnetic ion, Dy^{3+} or Ho^{3+}, and two diamagnetic rare earth ions linked together with the central N^{3-} ion as shown in Fig. 3.1. In the ground state, they are a good system where the pseudospin model can be applied for the determination of the magnetic moment. For simplicity, the word "spin" would be used for the total angular momentum of an ion. The validity of the pseudospin model (due to a large separation of the ground state multiplet) is backed by the comparison of *ab initio* calculations of magnetic properties of $Dy_2ScN@C_{80}$ [61] with the measurements [24]. They both yield similar results in the interaction energy of the two dysprosium ions.

3.2. Isotropic Pseudospin System

The ensembles studied in this thesis consist of a large number of molecules ($\approx 10^{17}$) which do not have any preferential orientation. The magnetic moments of the ions inside the molecule can point in every direction with equal probability. This leads to an isotropic distribution of magnetic moments or as described here pseudospins.

However, before describing the magnetization of an isotropic system, we start with a more straightforward case where all the pseudospins are oriented parallel to the magnetic field.

3.2.1. The Collinear Case

The most straightforward scenario (Fig. 3.2) is when all pseudospins are oriented along the external magnetic field, we call it the collinear case. This scenario is very

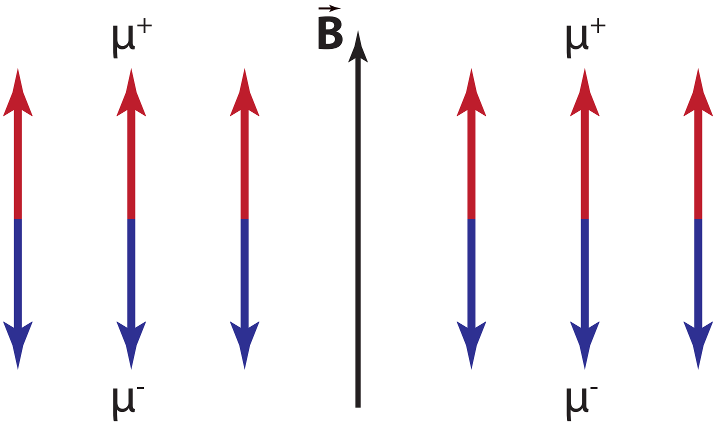

Figure 3.2. Collinear, parallel, orientation of pseudospins with the magnetic field $\vec{B}$. μ^+ and μ^- are respectively the parallel and antiparallel orientations of the magnetic moment $\vec{\mu}$.

similar to the non-interacting Ising model.

The magnetic moment $\vec{\mu}$ in the collinear case is either parallel μ^+ $\theta = 0°$ or antiparallel μ^- $\theta = \pi$ to the external magnetic field $\vec{B}$, where θ is the angle between the external magnetic field $\vec{B}$ and the moment $\vec{\mu}$.

The two-fold degeneracy of the two orientations of the magnetic moment μ is lifted by the Zeeman splitting induced by the external magnetic field. The Zeeman energy for the spin up μ^+ and spin down μ^- is:

$$E_\uparrow = -\mu B \text{ and } E_\downarrow = \mu B. \tag{3.1}$$

At zero Kelvin all the pseudospins would orient parallel to the magnetic field corresponding to the lowest energy state leaving the excited state with antiparallel orientation empty. However, at finite temperature, the excited states would be thermally occupied. The population probabilities obey Boltzmann statistics.

The probability of the spin up, parallel, $N_\uparrow$ and spin down, antiparallel, $N_\downarrow$ states follows the Boltzmann distribution:

$$p_\uparrow = \frac{e^{-E_\uparrow/k_B T}}{Z_{\text{col}}} \text{ and } p_\downarrow = \frac{e^{-E_\downarrow/k_B T}}{Z_{\text{col}}}, \tag{3.2}$$

where Z_{col} is the partition function of the collinear system:

$$Z_{\text{col}} = e^{-E_\uparrow/k_BT} + e^{-E_\downarrow/k_BT}. \tag{3.3}$$

Thus, the number of pseudospins in the spin-up and spin-down states for the total number of spins $N = N_\uparrow + N_\downarrow$ are:

$$N_\uparrow = N\frac{e^{-E_\uparrow/k_BT}}{Z_{\text{col}}} \text{ and } N_\downarrow = N\frac{e^{-E_\downarrow/k_BT}}{Z_{\text{col}}}. \tag{3.4}$$

Using the equations above, the total magnetic moment of the collinear system can be calculated:

$$\mu_{\text{col}} = (N_\uparrow - N_\downarrow)\,\mu = N\mu\,\frac{e^{-E_\uparrow/k_BT} - e^{-E_\downarrow/k_BT}}{e^{-E_\uparrow/k_BT} + e^{-E_\downarrow/k_BT}}\,. \tag{3.5}$$

The absolute value of the Zeeman energy for the collinear case of a magnetic moment μ in an external magnetic field B is $E_Z = \mu B$. Thus, $E_\uparrow = -E_Z$ and $E_\downarrow = E_Z$. Using this expression the previous formula for μ_{col} can be expressed as:

$$\mu_{\text{col}} = N\mu\,\frac{e^{E_Z/k_BT} - e^{-E_Z/k_BT}}{e^{E_Z/k_BT} + e^{E_Z/k_BT}} = N\mu\,\tanh\frac{E_Z}{k_BT}\,. \tag{3.6}$$

After plugging in the expression for the Zeeman energy, we get to the final formula for magnetization of the collinear model of pseudospins,

$$\mu_{\text{col}} = N\mu\,\tanh\frac{\mu B}{k_BT}\,. \tag{3.7}$$

3.2.2. The Non-Collinear Case

In case the axis of pseudospins is at an angle θ to the direction of the external magnetic field (Fig. 3.3) in Eq. 3.7 one should consider the projection of the moment μ on the magnetic field $\mu\cos\theta$. Eq. 3.7 transforms into:

$$\mu_\theta(T,B) = N\mu\,\cos\theta\,\tanh\frac{\mu\,\cos\theta\,B}{k_BT}\,. \tag{3.8}$$

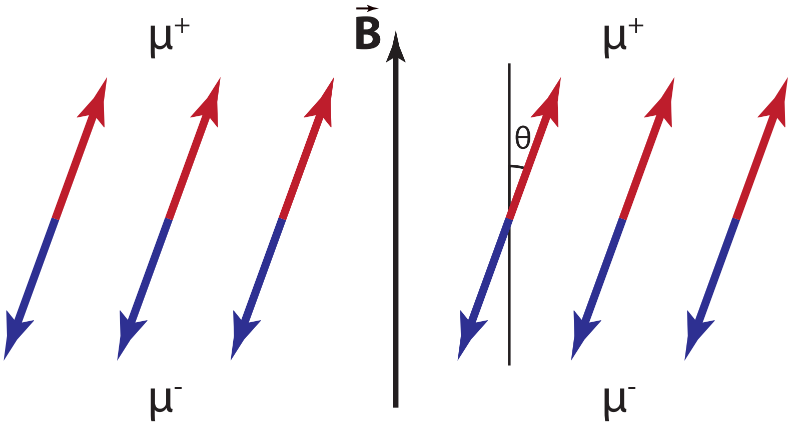

Figure 3.3. The non-collinear case with an angle θ between the magnetic field $\vec{B}$ and the pseudospin $\vec{\mu}$.

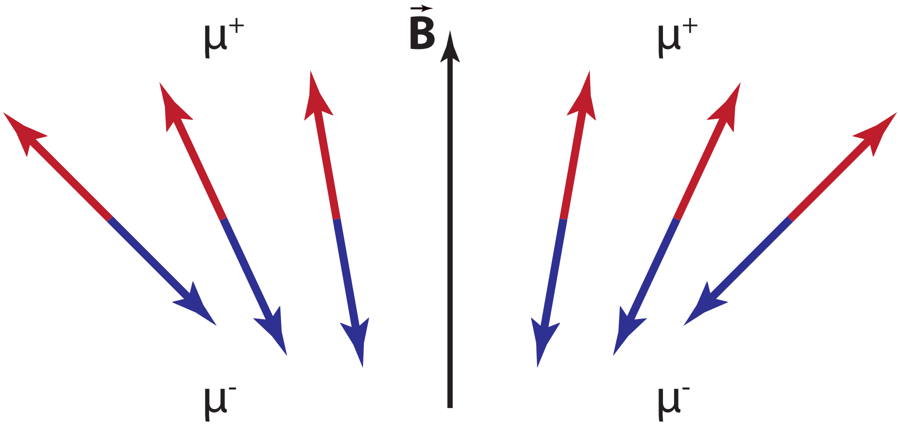

Figure 3.4. The isotropic distribution of pseudospins in space. The pseudospins point equally in all directions.

3.2.3. Isotropic Distribution of Pseudospins

Now, the final step is to model our system in question. The system is a collection of isotropically distributed in space endohedral fullerenes. Every solid angle $\mathrm{d}\Omega$ contains the same number of pseudospins. To calculate the magnetization of our system we need to average it over a sphere 4π; with Eq. 3.8 follows [24]:

$$\begin{aligned}\mu_{\text{iso}}(T,B) &= \frac{\int_{2\pi}\mu_\theta \,\mathrm{d}\Omega}{\int_{2\pi}\mathrm{d}\Omega} = \int_0^{\pi/2} \mu_\theta \sin\theta \,\mathrm{d}\theta \\ &= N\mu \int_0^{\pi/2} \tanh\frac{\mu B\,\cos\theta}{k_B T}\,\cos\theta\,\sin\theta\,\mathrm{d}\theta. \end{aligned} \tag{3.9}$$

The integration was performed over a 2π hemisphere as the two hemispheres are symmetric with respect to the external magnetic field which points along the z-axis.

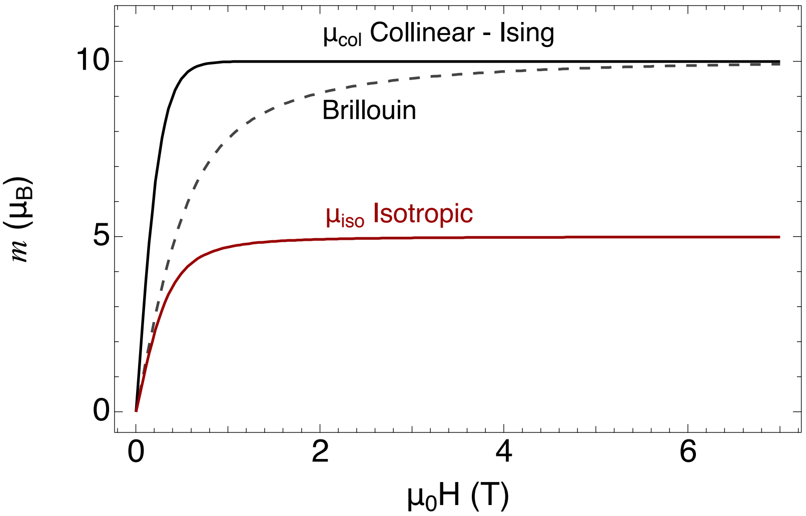

Figure 3.5. Calculated mean magnetization per moment as a function of magnetic field of isotropic μ_{iso} (Eq. 3.9) and collinear μ_{col} (Eq. 3.7) pseudospin systems along with a Brillouin function. All three curves were generated with the same parameters: magnetic moment of the pseudospin $\mu = 10\ \mu_B$, $T = 1.8$ K.

Figure 3.5 shows calculated magnetization curves for isotropic μ_{iso} (Eq. 3.9) and collinear μ_{col} (Eq. 3.7) pseudospin systems along with a Brillouin function with the same parameters. Both collinear and isotropic systems reach saturation faster than the Brillouin function. There is also a significant difference between the collinear and isotropic systems. The average magnetic moment of μ_{iso} at saturation is half of the nominal moment of the pseudospin. Whereas, μ_{col} and Brillouin function do achieve their full value at saturation.

3.3. Orientation of the Pseudospin System in Thermal Equilibrium

The endohedral unit at high temperatures is subject to free hop-rotation between the conformers. A conformer is a structure with the same orientation of the carbon cage but different orientation of the endohedral unit inside the carbon cage. Unlike the example discussed in the isotropic pseudospin system (Sec. 3.2.3), we use here a magnetic moment, pseudospin, $\vec{\mu}$ which can point in any direction (full rotational symmetry) and is represented as a vector of fixed length μ.

At $T = 0$ K and absence of external magnetic field due to the rotational symmetry the distribution of pseudospins is isotropic. Now apply a magnetic field in which all the pseudospins are parallel due to lack of thermal energy. This scenario represents the collinear case discussed earlier in Sec. 3.2.1. At finite temperature $T > 0$ the distribution of pseudospins deviates from the collinear case and tends to isotropic distribution due to thermal energy. Finally, the system reaches isotropic distribution at an applied magnetic field only when $T \to \infty$.

The motion of endohedral unit was previously studied with molecular cluster dynamics performed for the NMR shifts of ^{13}C with molecular dynamics trajectory [64] and DFT-based Born-Oppenheimer molecular dynamics (BOMD). Simulations for $\mathrm{YSc_2N@C_{80}}$ [60] indicate the possible conformers inside the cage. Metal atoms are positioned similarly to the center of the hexagon and are slightly shifted towards the hexagon-pentagon (5/6) edge. The conformers depend on the symmetry of the molecule C_3; $C_{S,a}$; $C_{S,b}$; etc. [25].

The number of possible orientations of the pseudospins in the system is quite high. For each molecule the number of conformations inside the cage is ≈ 60, the number of molecules in the measured ensemble is extremely high ($\approx 10^{17}$) and the time scale of hopping is tiny ($\approx$ picoseconds [60]) compared to the measurement time scale. Thus for further modeling, the endohedral unit is approximated to be freely rotating inside the cage at high temperatures.

For simplicity, let us discuss a system with only one magnetic ion in the endohedral unit. This model is later applied for $\mathrm{HoLu_2N@C_{80}}$ (Sec. 4.7 and [59]). As mentioned earlier, the concept of the pseudospin can be applied to the magnetic moment of the Ho.

In the absence of an external magnetic field, all conformers are equally favorable. At high temperature, the orientation of the pseudospins is isotropic at an absence of magnetic field. The zero-field cooling keeps the isotropic distribution at low temperatures when the endohedral unit is frozen, i.e., does not change its orientation, which was discussed earlier in Sec. 3.2.3.

The application of external magnetic field breaks the spherical symmetry and induces a bias along the field direction. At $\theta = 90^\circ$ the two orientations of the pseudospin are degenerate and the magnetic torque acting of the pseudospin is maximum where θ is the polar angle between the pseudospin and the magnetic field $\vec{B}$. The torque tries to align the pseudospin parallel to the field where the Zeeman energy E_Z reaches its highest negative value.

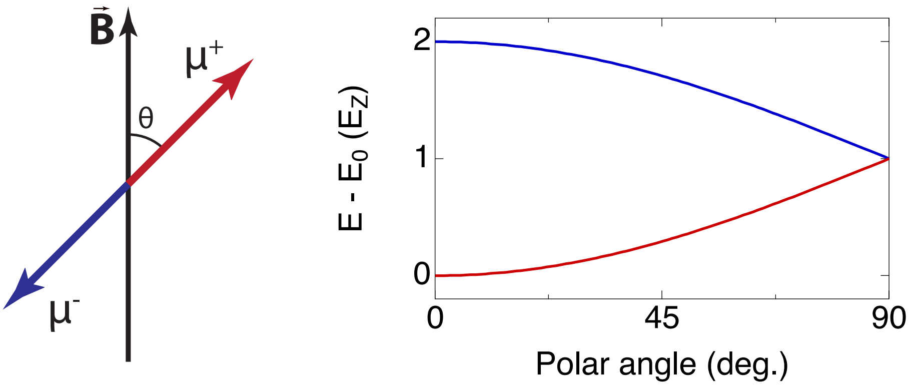

Figure 3.6. Left: Orientation of the pseudospin axis at an angle θ relative to the external magnetic field $\vec{B}$. Red indicates the lower energy orientation, while blue is marked for the higher energy state. Right: The Zeeman energy E_Z of the pseudospin depending on the angle θ. The red (blue) curve corresponds to the lower energy state, red arrow (higher energy state, blue arrow) from the left panel. The E_Z is zero for $\theta = 90°$ and reaches its maximum value at $\theta = 0°$.

The (Zeeman) energy of the pseudospin $\vec{\mu}$ depends on the angle θ: $E - E_0 = E_Z(1 \mp \cos\theta)$ (Fig. 3.6), where $E_Z = \mu B$ and E_0 is the energy level without Zeeman splittings.

Using the Boltzmann statistics, we can calculate the partition function Z_E of the equilibrium distribution by integrating over a hemisphere as the two hemispheres are symmetric. The partition function Z_E gets:

$$\begin{aligned} Z_E &= \int_{2\pi} \left\{\exp\left[-E_Z\left(1-\cos\theta\right)/k_BT\right] + \exp\left[-E_Z\left(1+\cos\theta\right)/k_BT\right]\right\} \mathrm{d}\Omega \\ &= 2\pi \int_0^{\pi/2} \left\{\exp\left[-E_Z\left(1-\cos\theta\right)/k_BT\right] + \exp\left[-E_Z\left(1+\cos\theta\right)/k_BT\right]\right\} \sin\theta \, \mathrm{d}\theta \\ &= 2\pi \frac{1-\exp\left(-2E_Z/k_BT\right)}{E_Z/k_BT}. \end{aligned} \tag{3.10}$$

The equilibrium magnetization μ_E (Eq. 3.11) is derived using the partition function Z_E (Eq. 3.10) and is shown in Fig. 3.7 as a function of k_BT/E_Z:

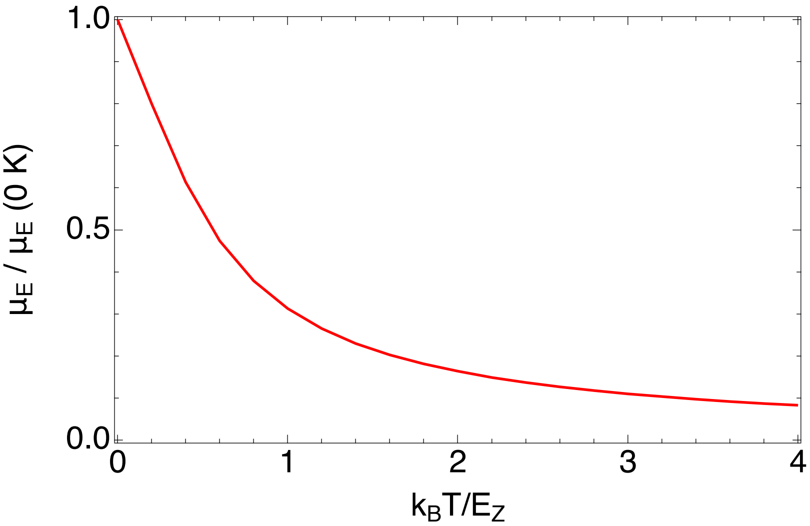

Figure 3.7. Equilibrium magnetization μ_E of pseudospin system as a function of k_BT/E_Z (Eq. 3.11).

$$\begin{aligned}\mu_E =& N\mu\frac{2\pi}{Z_E}\\ &\times\int_0^{\pi/2}\left\{\exp\left[-E_Z\left(1-\cos\theta\right)/k_BT\right]-\exp\left[-E_Z\left(1+\cos\theta\right)/k_BT\right]\right\}\sin\theta\,\mathrm{d}\theta\\ =& N\mu\frac{E_Z/k_BT-1+\left(E_Z/k_BT+1\right)e^{-2E_Z/k_BT}}{E_Z/k_BT\left(1-e^{-2E_Z/k_BT}\right)}.\end{aligned} \tag{3.11}$$

The angular distribution of the pseudospins is subject to change depending on the ratio of the temperature and the Zeeman energy k_BT/E_Z. At $T=0$ K all pseudospins are parallel to the field similar to the collinear case discussed in the Sec. 3.2.1. Contrary to $T=0$ K, the distribution of pseudospins approaches the isotropic case discussed in Sec. 3.2.3 when the thermal energy dominates against the Zeeman energy $k_BT/E_Z \gg 1$.

3.3.1. Angular Distribution of Pseudospins

In reality, the endohedral unit rotates only at high temperatures and is frozen below a specific freezing temperature T_F. Below T_F the endohedral unit does not have enough energy to go over the energy barrier E_A between the conformations within the time scale of the measurement. If the sample is cooled at an applied magnetic field, the torque on the magnetic moment of the endohedral unit can change the distribution of moments away from isotropic.

In contrast to the isotropic distribution (Eq. 3.9 in Sec. 3.2.3), where there are the same number of pseudospins in every solid angle dΩ, for the pseudospin system in the equilibrium the number of pseudospins in dΩ depends on the polar angle θ. The system has an axial symmetry with respect to the external field $\vec{B}$, and the distribution does not depend on the azimuthal angle ϕ.

Below the T_F, when the endohedral units are frozen, the distribution of the magnetic moments does not change irrespective of the magnetic field applied. The distribution stays the same as it was at T_F. Of course, at T_F the endohedral units do not stop changing their conformation immediately. The characteristic time increases exponentially with decreasing temperature and eventually becomes extremely long compared to the measurement time scale.

To describe the magnetization of the system below the freezing temperature T_F, the angular distribution of the pseudospins as a function of the polar angle θ should be determined.

The number of pseudospins pointing in the dΩ at a polar angle θ is:

$$\begin{aligned} n_\Omega &= \frac{\exp\left[-E_Z\left(1-\cos\theta\right)/k_BT\right]+\exp\left[-E_Z\left(1+\cos\theta\right)/k_BT\right]}{Z_E} \\ &= \frac{E_Z}{k_BT}\frac{\exp\left[-E_Z\left(1-\cos\theta\right)/k_BT\right]+\exp\left[-E_Z\left(1+\cos\theta\right)/k_BT\right]}{1-\exp\left(-2E_Z/k_BT\right)}. \end{aligned} \tag{3.12}$$

Another way of writing the pseudospin density distribution n_θ is to look at the number of pseudospins pointing at spherical segment of the thickness dθ at the polar angle θ, from Eq. 3.12 we get

$$n_\theta = n_\Omega \sin\theta. \tag{3.13}$$

Figure 3.8 shows the plots of Eq. 3.12 and 3.13 respectively. As expected, n_Ω equals one and does not depend on the polar angle θ when $E_Z/k_BT \ll 1$, meaning that in every dΩ in a random direction there are the same number of pseudospins. For the isotropic case the density distribution on the spherical segment n_θ (Eq. 3.13)

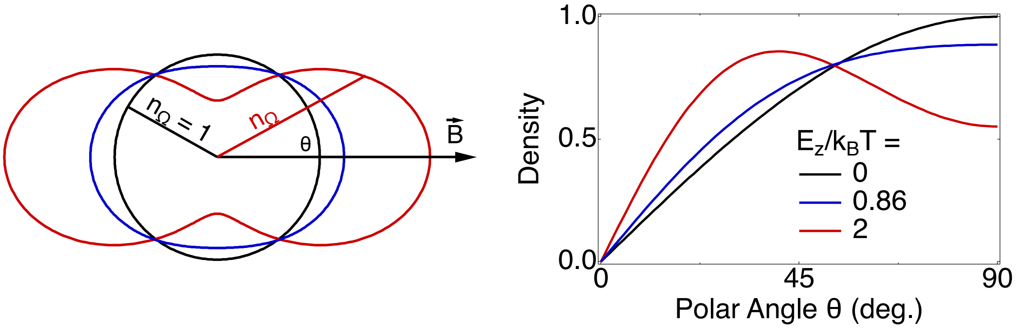

Figure 3.8. Left: The polar diagram of the angular density distribution plotted from the Eq: 3.12. The three curves share the same E_Z/k_BT ratio from the right panel plotted from the Eq: 3.13. The length of the vector from the center of the circle to the corresponding curve n_Ω is proportional to the angular density at that polar angle θ. As expected, for isotropic distribution (black circle) n_Ω, radius of the circle, is one indicating that all directions are symmetric. Right: Angular density distribution dependence from the Eq. 3.13 on the polar angle considering the spherical segment. The $E_Z/k_BT = 0.86$ corresponds to the E_Z and the freezing temperature T_F of HoLu$_2$N@C$_{80}$ for temperature sweeping rate 5×10^{-4} K s^{-1} discussed in the Sec. 4.7 [59].

has a sinusoidal shape. This is very similar to the magnetization of isotropically distributed system Eq. 3.9.

The effect of external magnetic field on the angular distribution n_Ω when $E_Z/k_BT > 1$ is visible in Fig. 3.8 left in the deviation of n_Ω from an circular, isotropic, distribution. The distribution is elongated along the magnetic field. As seen from the graph n_Ω increases with increasing E_Z/k_BT along the field direction $\theta \approx 0°$.

The same effect is also visible in the n_θ curve in Fig. 3.8. The integral of all the three curves is the same indicating at the conservation of the number of pseudospins. Smaller θ are getting larger weight with increasing the E_Z/k_BT ratio.

For similarity with the isotropic case, the magnetization of a free rotating system μ_E 3.11 can be rewritten

$$\mu_E = N\mu \int_0^{\pi/2} n_\Omega \tanh \frac{E_Z \cos\theta}{k_BT} \cos\theta \sin\theta \, \mathrm{d}\theta. \tag{3.14}$$

When $n_\Omega = 1$ the Eq. 3.14 becomes the already known equation for the magnetization of the isotropically distributed pseudospins Eq. 3.9.

3.3.2. Magnetization Below the Freezing Temperature

Below the freezing temperature T_F, the angular distribution n_Ω of the pseudospins does not change and has the same shape as at T_F. To describe the magnetization below the T_F, n_Ω at T_F should be considered. Therefore, for angular distribution we have

$$n_\Omega(T_F) = \frac{E_Z}{k_B T_F} \frac{\exp\left[-E_Z\left(1-\cos\theta\right)/k_B T_F\right] + \exp\left[-E_Z\left(1+\cos\theta\right)/k_B T_F\right]}{1-\exp\left(-2E_Z/k_B T_F\right)}. \tag{3.15}$$

Therefore, the magnetization μ_F of the frozen pseudospin system for $T < T_F$ gets:

$$\mu_F = N\mu \int_0^{\pi/2} n_\Omega(T_F) \tanh\frac{E_Z \cos\theta}{k_B T} \cos\theta \sin\theta \, \mathrm{d}\theta. \tag{3.16}$$

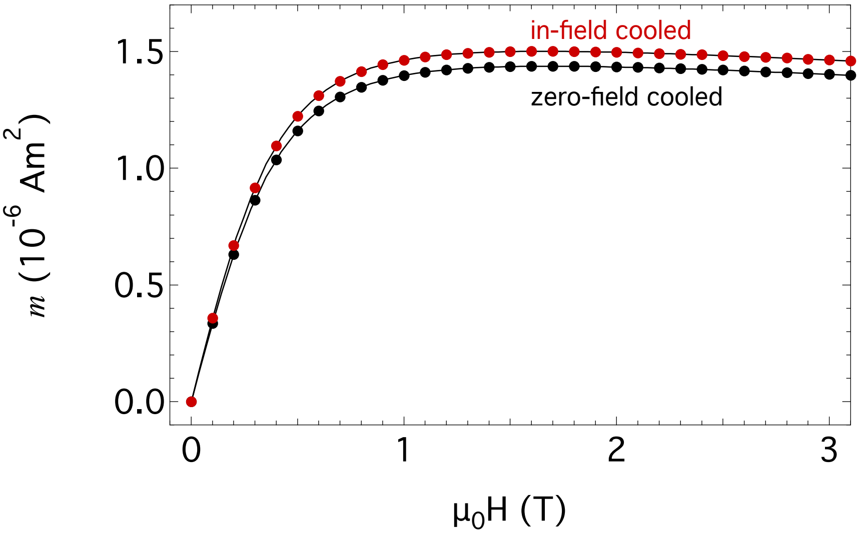

Figure 3.9. Magnetization m of TbSc$_2$N@C$_{80}$ as a function of the external magnetic field at $T = 1.8$ K (raw data). Both zero-field (black circles) and in-field $\mu_0 H = 7$ T (red circles) cooled data were fitted (solid lines) simultaneously with the isotropic pseudospin μ_{iso} Eq. 3.9 and frozen pseudospin μ_F model below the T_F Eq. 3.16. The fits additionally include a linear diamagnetic background. The best fit parameters are: number of Tb ions (molecules) $N = (3.7 \pm 0.01) \times 10^{16}$, Tb magnetic moment 9 ± 0.005 μ_B, $T_F = 60.2$ K for $B = 7$ T and the background $\chi = -(4.77 \pm 0.005) \times 10^{-8}$ $\mathrm{A\,m^2\,T^{-1}}$. The temperature sweep rate was 5×10^{-2} $\mathrm{K\,s^{-1}}$. The mass of the sample is 76.5 μg calculated with 1223.7 g/mol molar mass of the molecule.

The freezing temperature T_F can be extracted by fitting the magnetization curves below T_F as shown in Fig. 3.9. A set of magnetization curves are measured for the

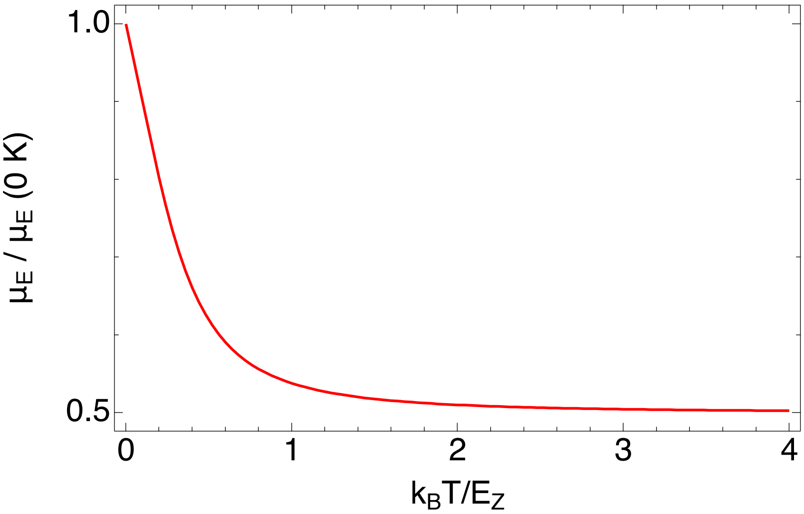

Figure 3.10. Saturation magnetization $\mu_{\text{sat}}(T_F)$ (Eq. 3.17) as a function of k_BT/E_Z. If $k_BT/E_Z \gg 1$ it is the isotropic case. As expected, the saturation magnetization of an isotropic system is the half of the collinear one. In $k_BT/E_Z \ll 1$ case, the Zeeman energy dominates over thermal energy making the system similar to the collinear case discussed earlier.

system. The magnetization m *versus* external magnetic field $\mu_0 H$ of a zero-field and in-field cooled samples are measured. A simultaneous fit is performed for these two curves. The zero-field cooled, isotropic, sample is fitted with the Eq. 3.9 and in-field cooled with the Eq. 3.16. The magnetic moment, the number of pseudospins and a linear diamagnetic background are linked to one another during the fits to have the same value for zero-field and in-field cooled samples. Only the T_F is not linked with the zero-field cooled sample, as the concept of T_F is not applicable there. All these parameters can be extracted from the fits.

Figure 3.10 shows the saturation magnetization of the pseudospin system calculated from Eq. 3.17. The Eq. 3.17 is in turn derived from the Eq. Eq. 3.11.

$$\mu_{\text{sat}}(T_F) = N\mu \frac{\left[1 - \exp\left(-E_Z/k_BT\right)\right]\left[\left(E_Z/k_BT + 1\right)\exp\left(-E_Z/k_BT\right) + E_Z/k_BT - 1\right]}{E_Z/k_BT\left[1 - \exp\left(-2E_Z/k_BT\right)\right]} \tag{3.17}$$

In Fig. 3.10 the system transitions from isotropic to collinear case depending of the ratio k_BT_F/E_Z. If $k_BT_F/E_Z \gg 1$, the system freezes with an isotropic distribution of pseudospins as discussed earlier. In the opposite case when $k_BT_F/E_Z \ll 1$, the Zeeman energy dominates over the thermal energy and the system is able to reach its maximum saturation magnetization achieved by the collinear orientation of the

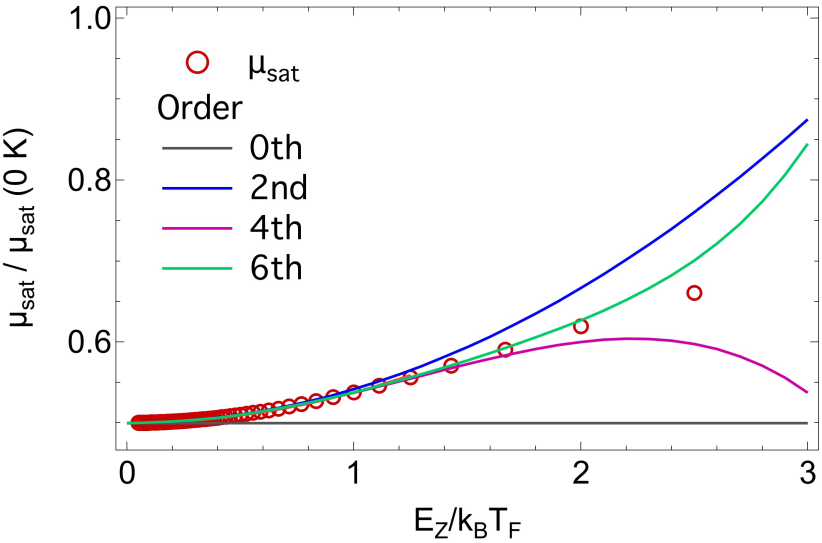

Figure 3.11. The Taylor expansion of saturation magnetization μ_{sat} vs E_Z/k_BT_F. 0th, 2nd, 4th and 6th order approximations are shown. For $E_Z/k_BT_F \leq 1$ a parabolic dependence of μ_{sat} from E_Z/k_BT_F can be used.

pseudospins. In this case, all pseudospins are parallel to the external magnetic field.

For small E_Z/k_BT values, the Eq. 3.17 can be approximated by Taylor expansion

$$\mu_{\text{sat}} = N\mu\left[\frac{1}{2} + \frac{1}{24}\left(\frac{E_Z}{k_BT}\right)^2 - \frac{1}{240}\left(\frac{E_Z}{k_BT}\right)^4 + \frac{17}{40320}\left(\frac{E_Z}{k_BT}\right)^6 + \dots\right]. \quad (3.18)$$

Figure 3.11 shows the dependence of the normalized saturation magnetization and its Taylor expansion of 0th, 2nd, 4th and 6th order on E_Z/k_BT_F. The 0th order is a constant and equals to 1/2. This is the saturation magnetization of the isotropic system. Adding more terms, the 2nd order can already be used to describe the system with $E_Z/k_BT_F \leq 1$ with less than 2% deviation between the analytical result and the 2nd order Taylor expansion. $E_Z/k_BT_F \leq 1$ is the range achievable with our endofullerenes and the MPMS3 system. Of course, higher orders give more accuracy, but given the capacity of modern computers, the full analytic function without approximations is more desirable.

Figure 3.12 shows the magnetization of the pseudospins as a function of k_BT/E_Z with three different freezing points. The system stays in thermal equilibrium until its freezing point. Below the freezing point T_F, the distribution of pseudospins stays at the value of T_F, and the magnetization continues to increase following Eq. 3.16.

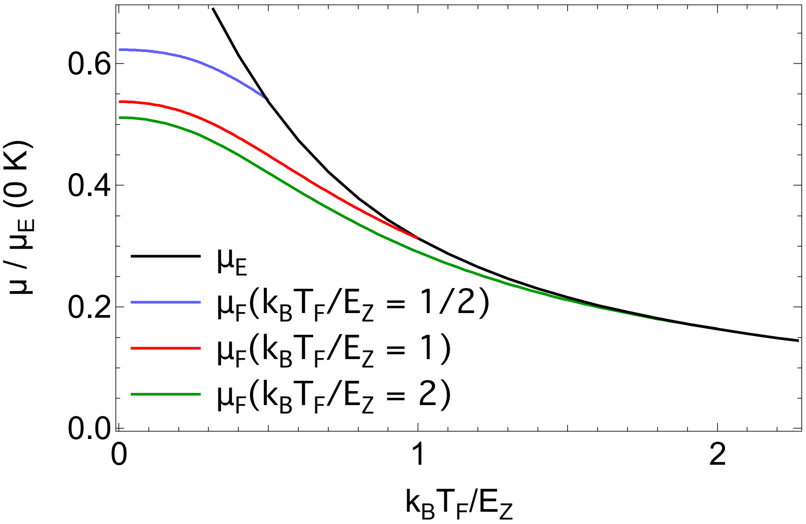

Figure 3.12. Magnetization of a pseudospin system as a function of $k_B T/E_Z$. The black line is a calculated curve of the equilibrium magnetization Eq. 3.14. The effect of the freezing is demonstrated with the model magnetization below T_F μ_F Eq. 3.16 for three different $k_B T_F/E_Z$ values—blue: 1/2, red: 1 and green 2.

3.4. Kinetics

The effect of in-field cooling depends on the cooling rate. The slower the sample is cooled, the larger the effect of the increase in saturation magnetization is. The kinetics of the system can be described by an energy barrier E_A and an attempt frequency ν [59, 65]. The dependence of the freezing temperature T_F on the cooling rate can be extracted.

As described earlier, the magnetic moment, the number of pseudospins, the diamagnetic background and the freezing temperature T_F can be extracted from the magnetization curves below T_F. All other parameters except the freezing temperature T_F do not depend on the cooling rate β of the in-field cooled sample. From the cooling rate β dependence of the freezing temperature $T_F(\beta)$ the energy barrier E_A between the conformers and the attempt frequency ν can be extracted.

For simplicity, only one energy barrier E_A and one attempt frequency ν is taken into account in the model. In the kinetic model an assumption that the thermal equilibrium is approached with an exponential function $\Delta\mu(\Delta t) = \Delta\mu_E \exp(-\Delta t/\tau)$ is made, where $\Delta\mu_E$ is the deviation from the equilibrium magnetization described with Eq. 3.14. In Fig. 3.12 $\Delta\mu_E$ would be the difference between the black equilibrium curve μ_E and one of the μ_F curves below the freezing point. $\Delta\mu_E$ increases with lowering the temperature below T_F.

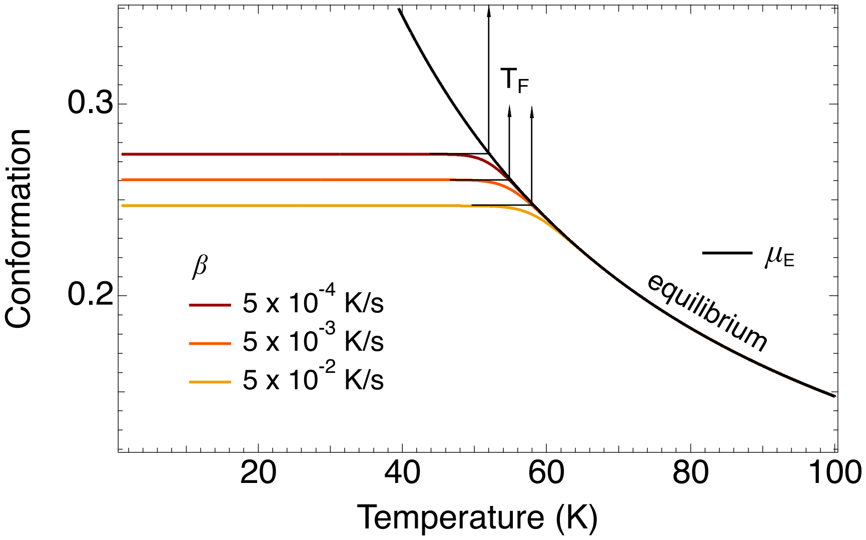

Figure 3.13. Simulations of conformational change during cool down. Equilibrium magnetization (black) μ_E and the freezing of conformational change with corresponding freezing temperature T_F. The parameters for the simulation are: energy barrier $E_A = 2145$ K, attempt frequency $\nu = 1.8 \times 10^{14}$ s^{-1}, cooling rate β of 5×10^{-2} K s^{-1}, 5×10^{-3} K s^{-1} and 5×10^{-4} K s^{-1}. These parameters match with the simulations performed for the paper presented in Sec. 4.7 [59].

The time constant τ responsible for reaching the equilibrium and depends on the energy barrier E_A, attempt frequency ν and the temperature. τ is determined from the differential equation of relaxation over a single barrier

$$\mathrm{d}\mu = -\mu\nu\, e^{-E_A/k_B T}\mathrm{d}t. \tag{3.19}$$

After taking τ so that the magnetization at the $t = \tau$ $\mu(\tau)$ is e times smaller than at time zero $t = 0$, the expression for the time constant τ is

$$\tau = \frac{1}{\nu\, e^{-E_A/k_B T}}. \tag{3.20}$$

Time evolution of the system can be described as:

$$\mu(t + \Delta t) = \mu(t) + \Delta\mu_E(1 - e^{-\Delta t/\tau})\,, \tag{3.21}$$

where $\mu(t)$ and $\mu(t + \Delta t)$ are the magnetization of the system at time t and $t + \Delta t$ respectively, Δt is an experimental time step, $\Delta\mu_E = \mu_E(t + \Delta t) - \mu(t)$ is the deviation of the magnetization from equilibrium.

The simulation of the conformational change for cooling the system across the freezing temperature T_F is shown in Fig. 3.13 using Eq. 3.21 with the cooling rate $\beta = -\frac{\mathrm{d}T}{\mathrm{d}t}$. The parameters of the simulation in Fig. 3.13 match with that used in Sec. 4.7 and the paper [59]. The values of the parameters are: magnetic moment of the pseudospin $\mu = 9.55\ \mu_B$, the external magnetic field strength of 7 T during in-field cooling and warming, energy barrier $E_A/k_B = 2145$ K and attempt frequency $\nu = 1.8 \times 10^{14}\ \mathrm{s}^{-1}$. The simulations were performed for three different cooling rates β $5 \times 10^{-2}\ \mathrm{K\,s^{-1}}$, $5 \times 10^{-3}\ \mathrm{K\,s^{-1}}$ and $5 \times 10^{-4}\ \mathrm{K\,s^{-1}}$.

The conformation shown in Fig. 3.13 is connected with the angular distribution n_Ω. When $T \to \infty$, the equilibrium magnetization is zero $\mu_E = 0$ and the distribution of pseudospins is isotropic; $n_\Omega = 1$ irrespective of θ. At low temperatures the $T \to 0$ $\mu_E = 1$ which corresponds to the collinear case (Sec. 3.2.1).

The magnetization in the frozen state $T < T_F$ is governed by the angular distribution of pseudospins n_Ω which in turn depends on T_F where the angular distribution freezes at $n_\Omega(T_F)$. $n_\Omega(T_F)$ corresponds to the distribution of the system in equilibrium at temperature T_F.

The magnetization of the system falls behind μ_E as the conformation of the system does not have enough time to change by going over the energy barrier E_A. The simulations for different cooling rates β demonstrate this. The slower the system is cooled, the more time it has to adopt itself and align closer to the conformation, angular distribution, of the freely rotating pseudospin system.

The freezing temperature T_F can be inferred from these simulations. T_F was defined as the temperature the equilibrium magnetization μ_E has the same value as the maximum of value reached during the simulations (Fig. 3.13). T_F only weekly depends on the applied magnetic field as the energy barrier E_A is much bigger than the Zeeman energy E_Z.

However, the temperature interval ΔT where the deviation from equilibrium (free hop-rotation) is noticed, to the point where the change in conformation stops (frozen conformation) is smaller in simulations (ΔT_s) than in measurements (ΔT_m). ΔT_m is defined as the full width at half maximum of the derivative from m_i/m_z, where m_i/m_z is the ratio of temperature dependent magnetization of in-field m_i and zero-field m_z cooled samples (Fig. 4 (a) in [59]). ΔT_s is defined as the full width at half maximum of the second order derivative from the freezing of conformational change shown in Fig. 3.13 (colored curves). ΔT_s roughly corresponds to the temperature interval from the point that magnetization falls short from the equilibrium magnetization μ_E to the point where the simulated conformational change is flat (colored curves in Fig. 3.13).

From the calculations we get: $\Delta T_m \approx 15$ K and $\Delta T_s \approx 5.5$ K. The reason could be the simplicity of the model compared to the actual energy landscape inside the fullerenes. As an outlook, two barrier simulations could be implemented. Preliminary tests with two barrier system showed a less sharp transition in temperature.

4. $HoLu_2N@C_{80}$, $Ho_2LuN@C_{80}$ and $TbSc_2N@C_{80}$

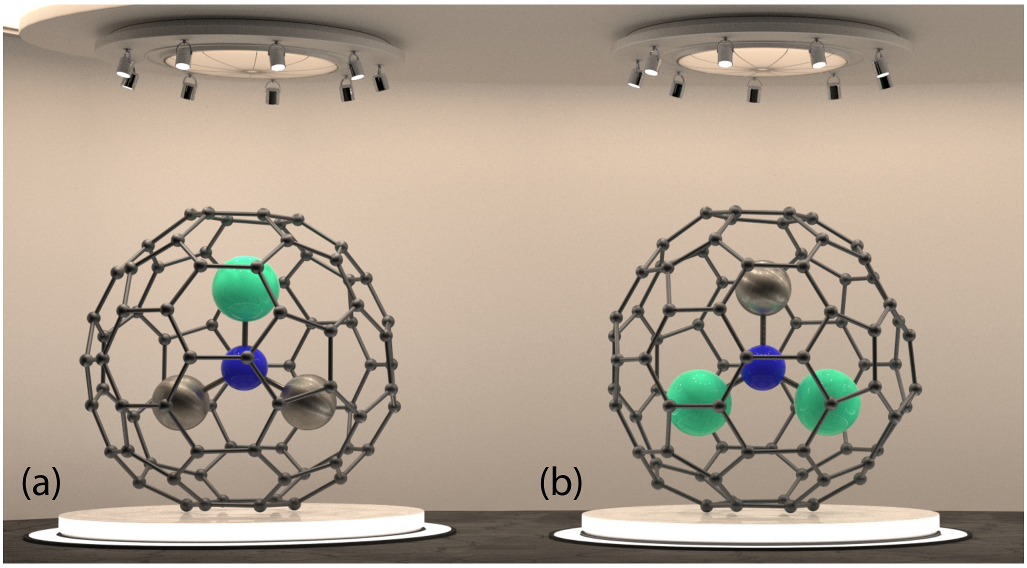

Figure 4.1. Ball-and-stick model of $HoLu_2N@C_{80}$ (a), $TbSc_2N@C_{80}$ (a) and $Ho_2LuN@C_{80}$ (b). The endohedral units with rare earth ions (Ho, Tb, Lu, Sc) at the corners of a triangle with nitrogen in the center is encapsulated in a C_{80} cage. Image courtesy: Rasmus Westerström.

4.1. Introduction

The magnetic properties of $HoLu_2N@C_{80}$, $Ho_2LuN@C_{80}$ and $TbSc_2N@C_{80}$ were investigated by a superconducting quantum interface device (SQUID). These fullerenes belong to the family of nitride cluster fullerenes (NCFs) with characteristic formula $R_3N@C_{2n}$ (R = Sc, lanthanides, etc.; $2n = 68 - 96$) [18–20].

From the paramagnetic lanthanide ions with axial symmetry with respect to R-N axis, those with largest magnetic moments were chosen. This criterion satisfies the three rare earth ions: Tb, Dy, and Ho.

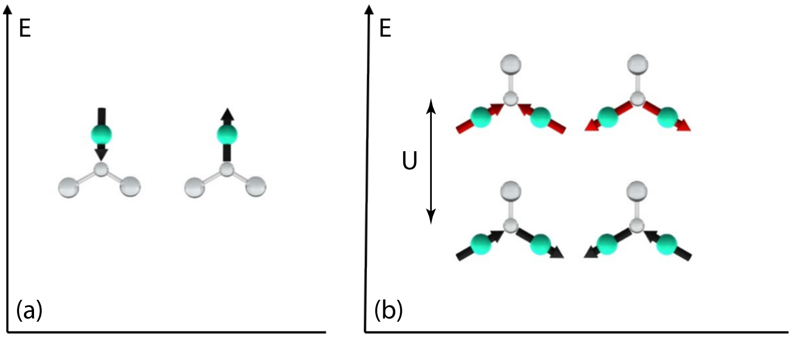

Figure 4.2. The ground state energy levels for $HoLu_2N@C_{80}$ and $Ho_2LuN@C_{80}$ at zero external magnetic field. The energy U is the sum of dipole and exchange barriers for $Ho_2LuN@C_{80}$.

Previous studies of $Ho_3N@C_{80}$ and $Tb_3N@C_{80}$ demonstrate the effect of the strong ligand field on the individual, ferromagnetically coupled R moments within the (R_3N) cluster [21]. While the studies on $Dy_xSc_{3-x}N@C_{80}$, where $x = 1 - 3$, demonstrate quantum tunneling ($x = 1$), remanence ($x = 2$) with long magnetization relaxation times [due to the separation energy U shown in Fig. 4.2(b)] and ground state frustration ($x = 3$) [23, 24]. $HoSc_2N@C_{80}$ also shows strong magnetic anisotropy with magnetization relaxation times in the order of milliseconds [66].

A model of $HoLu_2N@C_{80}$-I_h is shown in Fig. 4.1 (a). I_h corresponds to icosahedral symmetry which is the most abundant isomer. Hereafter, we will omit the isomeric label I_h. The endohedral unit $HoLu_2N^{6+}$ is encapsulated in a C_{80}^{6-} cage. The stability of the cage is achieved by migration of six electrons from the endohedral unit, two electrons from each rare earth ion. The third valence electron of the ions is involved in the bond with the central nitrogen. This ensures a closed shell for the nitrogen atom. Otherwise, it would also be paramagnetic.

The only paramagnetic species in $HoLu_2N@C_{80}$ is the Ho^{3+} ion (Fig. 4.1). The magnetic moment of Ho can point only towards or away from the central nitrogen N^{3-} due to the strong ligand field imposed by the latter [Fig. 4.2 (a)]. The ligand field, in turn, lifts the 17 fold degeneracy of isotropic Ho $^5I_8$ Hund ground state. As for $HoSc_2N@C_{80}$ [66], the ground state assumes $J_z = \pm 8$ with maximum theoretical magnetic moment of $\mu = 10\ \mu_B$, $2 \times \langle S_z \rangle + \langle L_z \rangle$ where $\langle S_z \rangle = 2$ and $\langle L_z \rangle = 6$. Thus, the concept of pseudospin (Sec. 3) can be used for describing the magnetic properties of $HoLu_2N@C_{80}$ [22, 59, 66].

$TbSc_2N@C_{80}$ has a very similar structure to $HoLu_2N@C_{80}$, one magnetic and two diamagnetic ions in the cage connected via a nitrogen ion [67]. The $^7F_6$ Hund ground state of Tb^{3+} is split by the ligand field and assumes $J_z = \pm 6$ with a nominal magnetic moment of $\pm 9\ \mu_B$ along the Tb-N axis.

$Ho_2LuN@C_{80}$, on the other hand, has two paramagnetic Ho ions and one diamagnetic Lu positioned in the corners of an approximately equilateral triangle. The Ho ions in $Ho_2LuN@C_{80}$, similar to $HoLu_2N@C_{80}$, assume, in the ground state, a total angular momentum of $J_z = \pm 8$ with a nominal magnetic moment of $\mu = 10\ \mu_B$ pointing along the Ho-N axis. The magnetic moment of the Ho ions also obeys the pseudospin model. The ferromagnetic and antiferromagnetic configurations of the two moments are separated by an energy U due to dipolar and exchange interaction as shown in Fig. 4.2.

In this chapter field and temperature dependence of the equilibrium magnetization for $HoLu_2N@C_{80}$ and $Ho_2LuN@C_{80}$ are discussed. The preparation of drop-cast samples is discussed in the Appendix B. The magnetization lifetime measured via AC susceptibility of these two molecules is compared with previously studied $HoSc_2N@C_{80}$ [66]. The switching of the molecular conformation of $HoLu_2N@C_{80}$ is reported in the attached paper [59] at the end of the chapter together with $TbSc_2N@C_{80}$. More measurements on $TbSc_2N@C_{80}$ were previously performed in the Ph.D. thesis of Roland Stania [67].

4.2. Field Dependent Magnetization of $HoLu_2N@C_{80}$ and $Ho_2LuN@C_{80}$

Magnetization m of $HoLu_2N@C_{80}$ and $Ho_2LuN@C_{80}$ as a function of field and temperature measured with a SQUID device are shown in Fig. 4.3 (a) and (c) with their respective reduced magnetization in the panel (b) and (d). The measurements of $HoLu_2N@C_{80}$ were performed in the temperature range between 1.8 K and 2.4 K. For $Ho_2LuN@C_{80}$ the temperature range was wider, i.e., between 1.8 K and 8 K in 16 steps.

The magnetization curves of $HoLu_2N@C_{80}$ [Fig. 4.3 (a)] and $TbSc_2N@C_{80}$ (Fig. 3.9) were fitted with the pseudospin model for isotropic distribution Eq. 3.9 [59]. The model is discussed in more detail in Chapter 3. The best fit parameters for $HoLu_2N@C_{80}$ are: $N = (2.02 \pm 0.005) \times 10^{17}$, $\mu = 9.55 \pm 0.02\ \mu_B$, $\chi^d = 3 \times 10^{-8}$ Am^2/T and for $TbSc_2N@C_{80}$ the parameters are: $N = (3.7 \pm 0.01) \times 10^{16}$, $\mu = 9 \pm 0.005\ \mu_B$ and $\chi^d = -(4.77 \pm 0.005) \times 10^{-8}$ Am^2/T where N is the number of

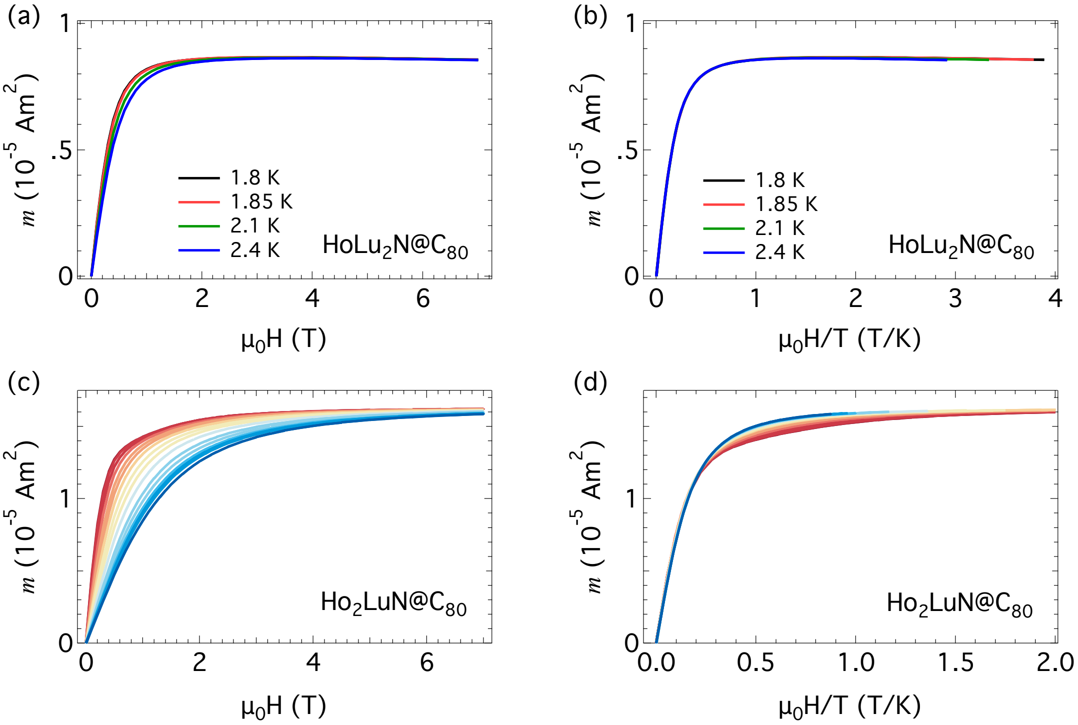

Figure 4.3. (a) and (c): Raw magnetization m of $HoLu_2N@C_{80}$ (a) and $Ho_2LuN@C_{80}$ (c) *versus* external magnetic field measured between 1.8 K and 2.4 K for $HoLu_2N@C_{80}$ and 1.8 K and 8 K in 16 steps for $Ho_2LuN@C_{80}$. (b) and (d): Reduced magnetization of $HoLu_2N@C_{80}$ (b) and $Ho_2LuN@C_{80}$ (d). The data curves for $Ho_2LuN@C_{80}$ in (d) in contrast to $HoLu_2N@C_{80}$ in (b) do not scale. This indicates the interaction between the Ho magnetic moments in $Ho_2LuN@C_{80}$.

magnetic moments or in this case number of molecules, μ is the magnetic moment of the paramagnetic ion and χ^d is the subtracted linear diamagnetic background. χ^d was inferred from the magnetization between 5 T and 7 T, and fits to Eq. 3.9. The masses of the samples are calculated from the saturation magnetization and are similar for $HoLu_2N@C_{80}$ 0.5 mg, $Ho_2LuN@C_{80}$ $\approx$ 0.3 mg and $TbSc_2N@C_{80}$ 76.5 μg.

Fig. 4.3 (b) shows the reduced magnetization of $HoLu_2N@C_{80}$. As seen from the graph it scales with $X = \mu_0 H/T$. However, for $Ho_2LuN@C_{80}$ [Fig. 4.3 (d)] the magnetization does not scale in the central part of the graph. This is an indication of the dipolar and exchange interaction energy U [Fig. 4.2 (b) between the two Ho moments that does not depend on X. Nevertheless, the curves scale at low X ($k_B T \gg U$) and at high X where the curves are degenerate $k_B T \ll U$ (all states are in the ground state doublet).

The magnetic moments of Ho and Tb are consistent with $J_z = 8$ and $J_z = 6$ ground states. The Hund degeneracy is lifted, and the Tb and the Ho ions assume the largest J_z in the Coulomb field of a negative point charge.

4.3. Temperature Dependence of the Magnetization

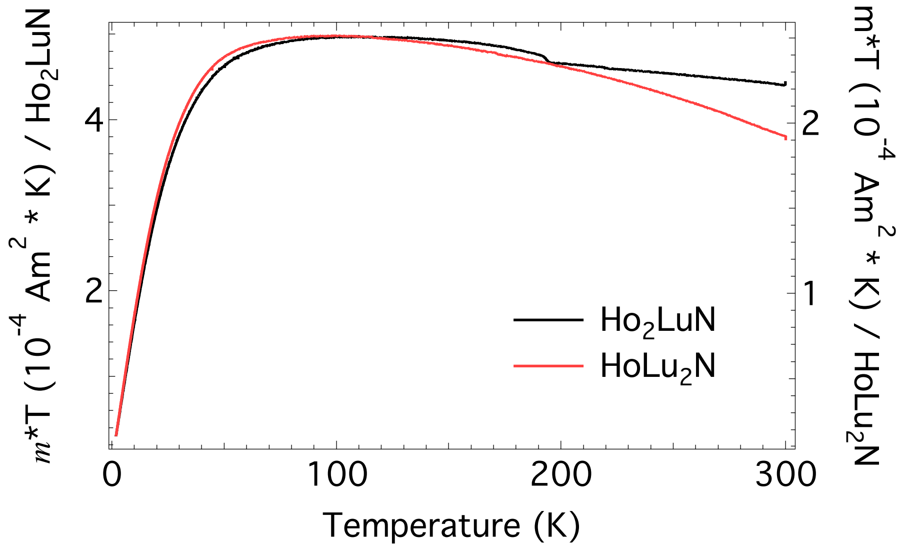

Figure 4.4. Magnetization times temperature $m \times T$ *versus* temperature for $HoLu_2N@C_{80}$ (red) and $Ho_2LuN@C_{80}$ (black). Both, the red and the black lines show paramagnetic behavior with a temperature independent diamagnetic part. The diamagnetic part dominates at higher temperatures making the slope negative. The kink at ≈ 185 K for $Ho_2LuN@C_{80}$ (black) could indicate the freezing of the cage rotation [68].

Figure 4.4 shows the temperature dependence of magnetization multiplied by temperature for $HoLu_2N@C_{80}$ and $Ho_2LuN@C_{80}$. This graph demonstrates the deviation from Curie behavior for temperatures below 50 K. At higher temperatures due to the presence of a temperature independent diamagnetic background the slope becomes negative. The population of higher J_z states may also contribute to the negative slope, but due to high energy separation, their contribution is neglected. As discussed in the following chapters this high-temperature behavior can be used to estimate the diamagnetic background.

The main difference between $HoLu_2N@C_{80}$ and $Ho_2LuN@C_{80}$ is the kink at 185 K for the latter molecule. The temperature dependence of $Ho_2LuN@C_{80}$ is different before and after the kink. This could be a hint to the freezing of the C_{80} cage rotation. The kink was reproduced several times for both cooling and warming across it. A similar transition at 250 K is reported previously for C_{60} [68]. It is not yet fully understood why the effect is visible in $Ho_2LuN@C_{80}$ and not in $HoLu_2N@C_{80}$.

4.4. AC Susceptibility

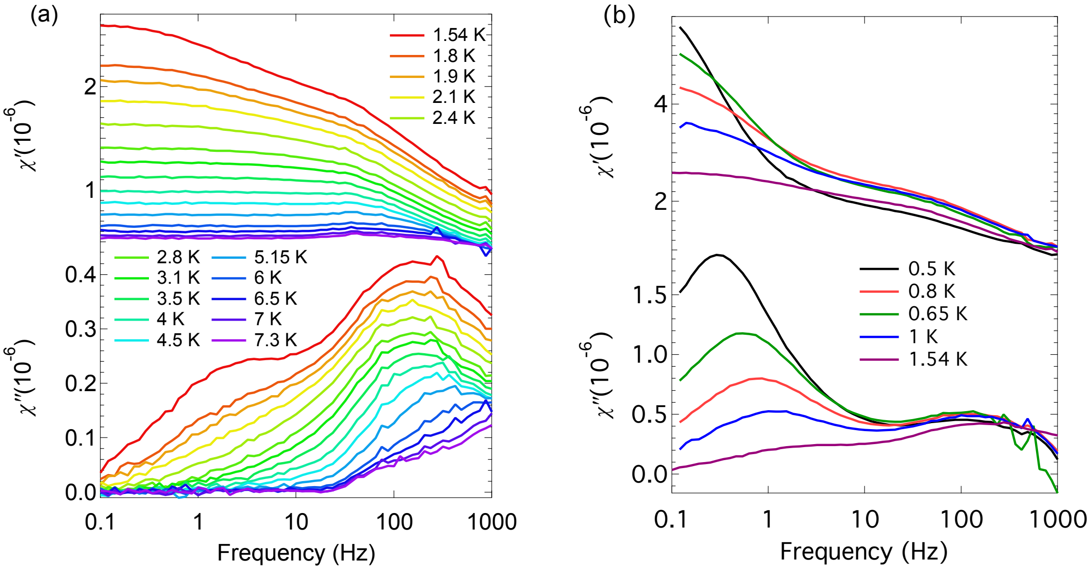

Figure 4.5. Real (in-phase) (top) and imaginary (out-of-phase) (bottom) component of AC susceptibility of HoLu$_2$N@C$_{80}$ measured at ≈ 0 T magnetic field. The measurements were performed in the temperature range of 1.8 K to 7.3 K in 15 steps (a) and in (b) the ^{3}He cryostat was used to achieve 0.5 K to 1.54 K temperatures. AC driving field amplitude was 1 mT up to 420 Hz and then it was lowered to 0.25 mT due to the equipment.

The fast relaxation of magnetization can be studied employing AC susceptometry discussed in more details in the section 2.2.2. Figure 4.5 (a) shows the frequency dependence of the real (in-phase) χ' (top) and the imaginary (out-of-phase) χ'' (bottom) component of AC susceptibility for HoLu$_2$N@C$_{80}$. In the left panel, the measurements are performed in the temperature range of 1.8 K to 7.3 K in 15 steps. Increasing the temperature even higher makes the relaxation process faster than the measurement limits of equipment used.

The χ' and χ'' show a typical behavior for a resonance, and even two resonances are visible at low temperatures. χ' is flat for low frequencies followed by a decline in the resonance. χ'', in contrast, shows a peak at the resonance and is close to zero otherwise. At 1.55 K there are two peaks visible in the χ'' graph. The lower temperature peak fades pretty fast with the increase of the temperature.

The higher frequency peak has a constant position until about 3 K. Above 3 K it starts shifting to higher frequencies. This indicates a decrease in the magnetization lifetime. Decreasing the temperature to 500 mK utilizing the ^{3}He cryostat [Fig. 4.5 (b)] leaves the higher frequency peak intact while the lower one increases in amplitude and shifts to the lower side of the spectrum.

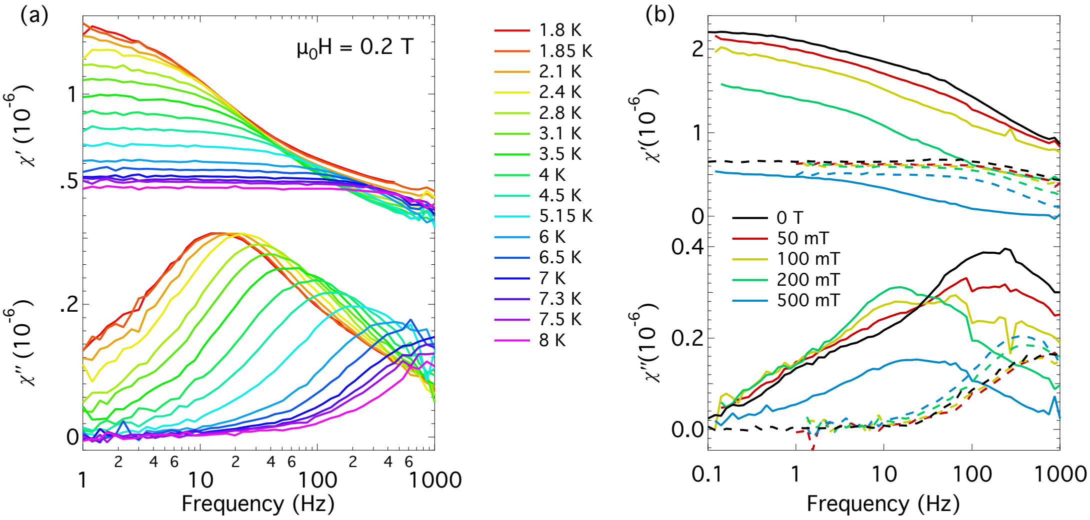

Figure 4.6. (a) Real (in-phase) (top) and imaginary (out-of-phase) (bottom) component of AC susceptibility of $HoLu_2N@C_{80}$ measured at 200 mT applied magnetic field in the temperature range of 1.8 K to 8 K in 16 steps. The panel (b) shows the field dependence of the AC susceptibility components measured at 1.8 K (solid lines) and 6 K (dashed lines). The 0 T data was taken from Fig. 4.5. The AC driving field amplitude was 1 mT up to 420 Hz (a) and 90 Hz (b), and then it was lowered to 0.25 mT due to the equipment limitations which resulted in a kink in the data (b).

The lower frequency resonance could correspond to inter-molecular interaction. The interaction of two Ho ions in the neighboring molecules. This hypothesis could be tested with dilution experiments.

On the other hand, the higher frequency peak could correspond to the actual magnetic lifetime of the Ho ion itself. The frequency of the peak in χ'' is related to the lifetime of the magnetic state. At low temperatures, the frequency does not change indicating quantum tunneling. The temperature dependent thermally activated processes start to dominate at higher temperatures.

Figure 4.6 shows the AC susceptibility data for $HoLu_2N@C_{80}$ for different temperatures and applied magnetic fields. Figure 4.6 (a) corresponds to measurements at 200 mT field and a temperature range of 1.8 K to 8 K. However, in Fig. 4.6 (b) the temperature is fixed to 1.8 K and 6 K while the magnetic field is different for each measurement.

The comparison of in-field and zero-field AC measurements reveals changes in the resonance frequency. The temperature independence of the peak position below 3 K is canceled. This is a hint of the effects of the external magnetic field. The application of magnetic field lifts the ground state degeneracy thus voiding the possibility of quantum tunneling of the magnetization.

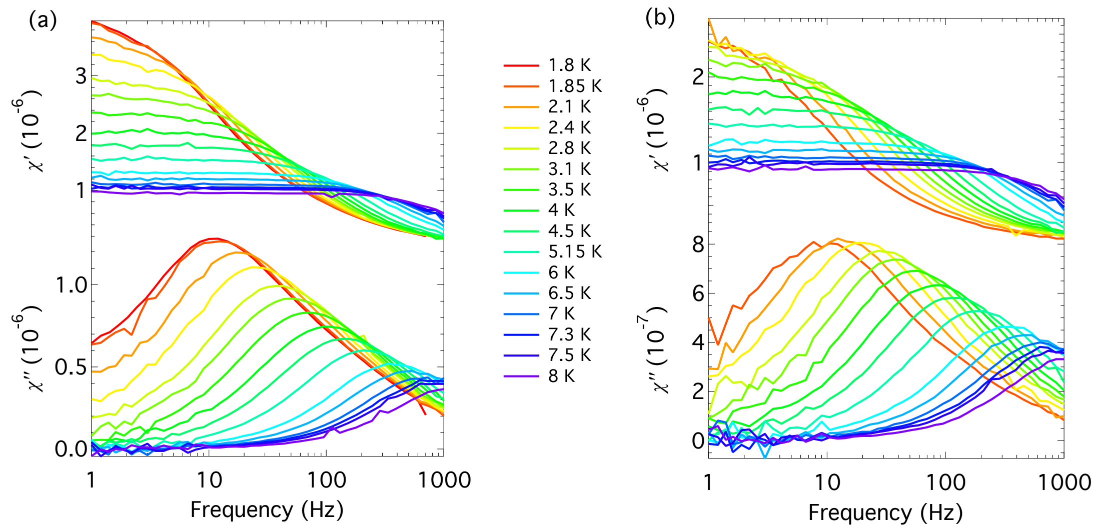

Figure 4.7. Real (in-phase) (top) and imaginary (out-of-phase) (bottom) component of AC susceptibility of $Ho_2LuN@C_{80}$ measured at ≈ 0 T (a) and 200 mT applied magnetic field (b) in the temperature range of 1.8 K to 8 K in 16 steps.

However, magnetic fields of different strengths have a different effect on the lifetime as demonstrated in Fig. 4.6 (b). An exception is the low-frequency peak (≈ 2 Hz) that is visible as a shoulder at 1.8 K which does not change its position. Application of 50 mT ($E_Z = 0.34$ K for a 10 μ_B moment) is enough to hinder quantum tunneling of magnetization and induce a difference in magnetization lifetime τ at 1.8 K. Already at a field of 100 mT, there is a factor of 10 decrease in τ, seen in χ'' peak frequency, compared to 0 T. However, the further increase in field strength does not slow the relaxation significantly. A field of 500 mT only reduces the signal amplitude. Further increase in the field to 1 T decreases the amplitude even more.

The picture is slightly different at 6 K. Whereas 50 mT field does not have the same drastic effect as at 1.8 K, the increase of the magnetic field to 500 mT has a marginal effect of slowing the relaxation compared to 200 mT. Also, the amplitude reduction for increasing field is not present.

While the ground state splitting due to external magnetic field can slow the relaxation by suppressing quantum tunneling, further increase of the magnetic field does increase the effect of other relaxation pathways: direct process, etc. discussed in more details in Sec. 2.4.

The effect of the applied DC magnetic field on AC susceptibility measurements on $Ho_2LuN@C_{80}$ is not as dramatic as for its sibling $HoLu_2N@C_{80}$. Figure 4.7 shows the χ' and χ'' measured at the zero (< 0.5 mT) and in 200 mT applied DC magnetic field. The measurements were performed in the temperature range of 1.8 K to 8 K.

The effect of the applied magnetic field is decreasing the overall amplitude of χ'' but increasing the relative intensities of higher temperature measurements.

The comparison of temperature dependent magnetization lifetimes of $HoLu_2N@C_{80}$, $Ho_2LuN@C_{80}$ and $HoSc_2N@C_{80}$ will be discussed in the next section.

4.5. Magnetization Relaxation Time Extraction

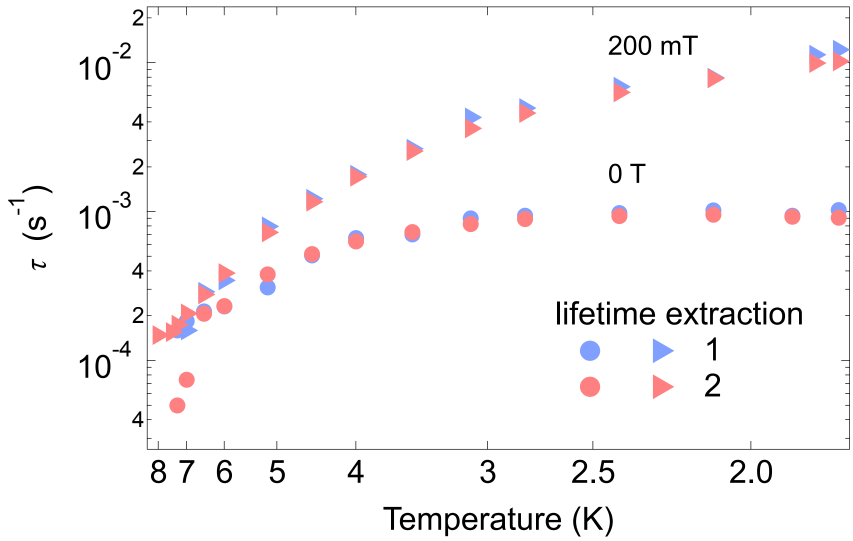

Figure 4.8. Two different methods (**1**–Eq. 4.1, **2**–Eq. 2.5 and 2.6.) for extracting magnetization relaxation times from AC susceptibility data. The shown example is for $HoLu_2N@C_{80}$ measured at zero (Fig. 4.5) and in an applied constant field of 200 mT [Fig. 4.6 (a)].

The magnetization relaxation times for $HoLu_2N@C_{80}$ shown in Fig. 4.8 were extracted from the AC susceptibility measurements [$\mu_0 H = 0$ T: Fig. 4.5 (a) and $\mu_0 H = 200$ mT: Fig. 4.6 (a)] in two ways. The detailed description of AC susceptometry is presented in Sec. 2.2.2.

Method **1** involves the fitting a polynomial around the apex of the χ" curve and extracting the frequency of the peak ν_p. The magnetization relaxation time τ is then calculated from ν_p using Eq. 4.1.

$$\tau = \frac{1}{\omega} = \frac{1}{2\pi\nu_p} \tag{4.1}$$

The second method **2** incorporates a simultaneous fit of Eq. 2.5 and 2.6 to real (in-phase) χ' and imaginary (out-of-phase) χ'' components of AC susceptibility respectively. The fit parameters are linked together to have the same values.

The extracted relaxation times match reasonably well with each other but method **1** has more scatter than method **2**. Method **2** allows a better fit to Eq. 2.23 as seen from χ^2 value shown in the next section. The τ's shown in the next section for $HoLu_2N@C_{80}$ at 0 T and 200 mT and $HoSc_2N@C_{80}$ at 200 mT were obtained using method **2** while for $Ho_2LuN@C_{80}$ method **1** was used.

4.6. Magnetization Relaxation Times

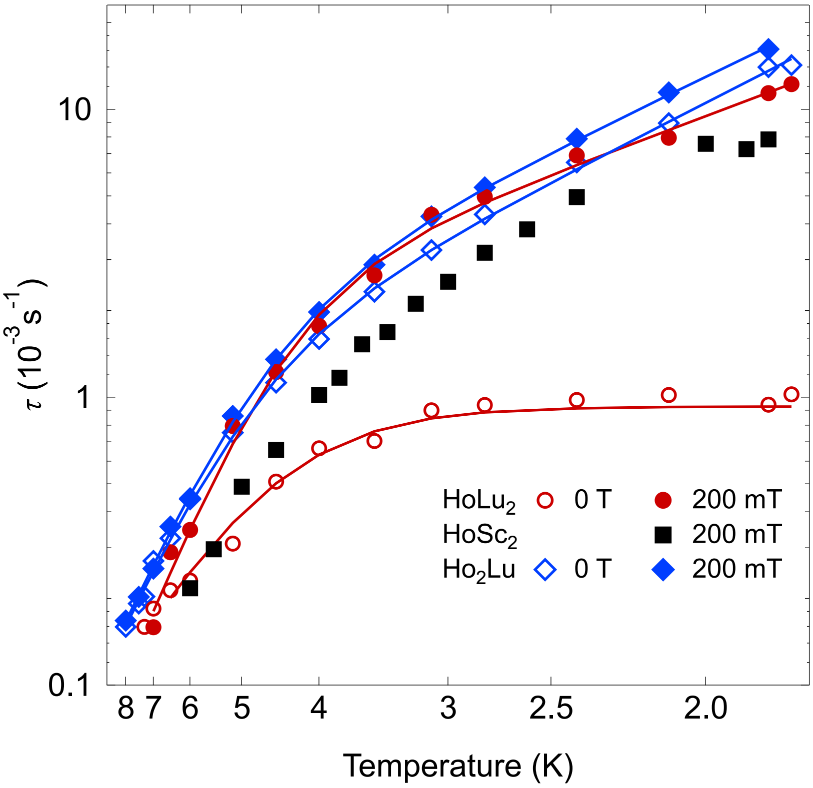

Figure 4.9. Magnetization relaxation times for $HoLu_2N@C_{80}$ (red) and $Ho_2LuN@C_{80}$ (blue) at zero (open symbols) and 200 mT (full symbols) applied magnetic field. The relaxation times for $HoSc_2N@C_{80}$ were reported previously and were measured at 200 mT magnetic field [66]. The solid lines are the fit of Eq. 4.3 and 4.2 with respective colors.

The temperature and field dependence of magnetization relaxation time τ allows the identification of specific relaxation pathways described in Sec. 2.4. Figure 4.9 shows the temperature dependence of the magnetization relaxation times τ for

$HoLu_2N@C_{80}$ ($\mu_0 H$ = 0 T, 200 mT), $Ho_2LuN@C_{80}$ ($\mu_0 H$ = 0 T, 200 mT) and $HoSc_2N@C_{80}$ ($\mu_0 H$ = 200 mT) [66]. The determination of τ's is described in the previous section.

In this section, the magnetization relaxation times for the above mentioned molecules are fitted to the functions of different possible relaxation pathways (Sec. 2.4). χ^2 of the fit is used to identify the most probable and dominant process for the corresponding molecule and applied DC magnetic field. Furthermore, simultaneous fits are also performed for the same molecule but different DC fields to decrease the number of variables and range of their possible values.

Equation 2.23 contains the characteristic temperature and field dependence for quantum tunneling, direct, two-phonon (Raman) and Orbach processes. As the number of parameters in Eq. 2.23 are too many, the equation is split into relatively small parts and fitted separately to the τ curves. The quality of the fit is judged from the χ^2 value.

At zero field, the fast spin-reversal between J_z and $-J_z$ states occurs via resonant quantum tunneling. This process does not require energy and thus, the characteristic time τ_{QTM} is temperature independent.

The application of magnetic field splits the degeneracy of $\pm J_z$ states lowering the rate of spin-reversal—first part of Eq. 2.23—as the moments now have to go over the thermal barrier which is described as an Orbach process. At higher magnetic field a faster relaxation process emerges between two non-degenerate J_z states provided there is a phonon to carry the energy difference—direct relaxation process. Another temperature dependent relaxation process mediated by double scattering on phonons is the Raman process.

The above-described processes involved in Eq. 2.23 are split into smaller groups for better fitting and are summarized in the equations below:

$$\tau^{-1} = \tau_1^{-1}\, e^{-\Delta_{\mathrm{eff},1}/k_B T} + \tau_2^{-1}\, e^{-\Delta_{\mathrm{eff},2}/k_B T} \tag{4.2}$$

$$\tau^{-1} = \tau_{\mathrm{QTM}}^{-1} + \tau_o^{-1}\, e^{-\Delta_{\mathrm{eff}}/k_B T} \tag{4.3}$$

$$\tau^{-1} = \tau_{\mathrm{QTM}}^{-1} + AT + \tau_o^{-1}\, e^{-\Delta_{\mathrm{eff}}/k_B T} \tag{4.4}$$

$$\tau^{-1} = \tau_{\mathrm{QTM}}^{-1} + C\,T^{n} \tag{4.5}$$

$$\tau^{-1} = \tau_{\mathrm{QTM}}^{-1} + AT + C\,T^{n} \tag{4.6}$$

where τ_{QTM} is quantum tunneling time, Δ_{eff} is the effective barrier during Orbach process with its prefactor τ_0, the coefficient for direct scattering A which is proportional to H^2 or H^4 (Eq. 2.23), and the exponential factor n with its coefficient C of the Raman scattering. As the relaxation times τ span over an order of magnitude, weighting of 10% of the corresponding τ value was used for each point for better fitting and χ^2 calculation.

The best fit parameters of the relaxation times to Eq. 4.2–4.6 are shown in Table 4.1.

To understand the effect of the diamagnetic ion in the endohedral cage a comparison between $HoLu_2N@C_{80}$ and previously studied $HoSc_2N@C_{80}$ is shown here. For better results, the τ values of $HoSc_2N@C_{80}$ were further fitted here to more functions than presented previously [66].

From individual fits $HoLu_2N@C_{80}$ at zero DC field, all functions showed close values of χ^2 while giving a slight preference to Eq. 4.3. The temperature dependence of τ shows sign of two distinct processes: one of them being temperature independent. The only temperature-independent component of Eq. 2.23 is the quantum tunneling. Tunneling fits well with the picture of one single magnetic moment in zero DC field tunneling between $+J_z$ and $-J_z$. The double Orbach fit returns small value for the Δ_{eff} making one of the processes similar to a quantum tunneling. The identification of the second process at this stage is not so trivial as the different in χ^2 between different processes is not so big.

	$HoSc_2N$	$HoLu_2N$		Ho_2LuN	
	200 mT	0 T	200 mT	0 T	200 mT
Double Orbach Eq. 4.2					
χ^2	4.6	1.02	2.1	2.48	0.956
τ_1 ($\times 10^{-6}$ s)	6.5	9.2	4.5	5.3	5.4
$\Delta_{\mathrm{eff},1}/k_B$ (K)	22.1	21.6	27.5	28.7	28.5
τ_2 ($\times 10^{-4}$ s)	8.9	9	10	4.5	6.5
$\Delta_{\mathrm{eff},2}/k_B$ (K)	4.1	0.07	4.1	6.3	6
QTM + Orbach Eq. 4.3					
χ^2	12 [66]	1	27	41.3	33.24
τ_{QTM} (ms)	7	0.9	8.3	12	11.6
τ_1 ($\times 10^{-5}$ s)	1.7(2)	0.97	1.3	2.5	2
$\Delta_{\mathrm{eff},1}/k_B$ (K)	16.5(6)	21.2	19.7	16	18.4
QTM + Direct + Orbach Eq. 4.4					
χ^2	-	-	10.4	-	-
τ_{QTM} (ms)	-	-	inf	-	-
A	-	-	60	-	-
τ_1 ($\times 10^{-5}$ s)	-	-	8.9	-	-
$\Delta_{\mathrm{eff},1}/k_B$ (K)	-	-	23	-	-
QTM + Raman Eq. 4.5					
χ^2	2.85 [66]	1.4	2.31	5.25	4.1
τ_{QTM} (ms)	13	9.7	12.4	38	28
C	4.4	1.84	2.2	6.8	3.5
n	3.86	4.12	3.9	3.2	3.6
QTM + Direct + Raman Eq. 4.6					
χ^2	-	-	0.26	-	-
τ_{QTM} (ms)	-	-	1.8	-	-
A	-	-	47	-	-
C	-	-	0.94	-	-
n	-	-	4.35	-	-

Table 4.1. Best fit parameters of relaxation times (Fig. 4.9) to the Eq. 4.2–4.6.

The zero field relaxation times τ for $HoSc_2N@C_{80}$ were not reported in the previous study as frequency of the χ'' peak was beyond the capabilities of the equipment ($\nu > 1.5$ kHz) [66]. However, from a zero DC field χ'' frequency scan at 2 K, the τ could be estimated to be at least a factor of ten shorter than $HoLu_2N@C_{80}$. The reason could be the increased radius of Lu compared to Sc (Shannon radii of Lu^{3+} and Sc^{3+} are 0.745 Å and 0.86 Å, respectively) [69]. The increased radius of the Lu ion pushes the N and Ho ions closer increasing the axial ligand field which in turn increases the tunneling barrier [62, 70]. The increase in the diamagnetic ion radius also increases the splitting between lowest and first excited states of the ligand field splitting of the Ho magnetic moment [60].

In an applied magnetic field the temperature-independent quantum tunneling is hindered the three compounds, $HoLu_2N@C_{80}$, $Ho_2LuN@C_{80}$ and $HoSc_2N@C_{80}$, show fairly similar magnetization reversal times. Moreover, $Ho_2LuN@C_{80}$ at zero field also has similar relaxation times to the in-field τ's of other compounds. The reason could be the dipolar and exchange interaction of the two Ho ions in the same cage which also hinders the quantum tunneling. The probability of double tunneling is low, the tunneling of the two Ho magnetic moment at the same time.

As seen from Table 4.1 and in the previous study of $HoSc_2N@C_{80}$ the τ data at 200 mT fit best to Eq. 4.5. In contrast, the τ's of in field $HoLu_2N@C_{80}$ fit better to a double Orbach process (Eq. 4.2) if the number of possible pathways is limited to two. However, a definitive conclusion can not be made from this as double Orbach has one more fitting parameter 4 *versus* 3 for others.

However, the origins of the 4.1 K barrier are not very clear as the Orbach process is field independent. Moreover, the Zeeman energy for a moment of 10 μ_B at 200 mT field is 1.35 K. Therefore, this barrier cannot be attributed to the Zeeman splitting considering that Δ_{eff} is the barrier height over which the spin has to go, not the difference in energy between the initial and final states.

Increasing the number of pathways, parameters also increases the quality of the fit (QTM + Direct + Raman or Orbach in Table 4.1). The fit for τ of $HoLu_2N@C_{80}$ at 200 mT achieves its minimum χ^2 when fitted with Eq. 4.6. Still, the better χ^2 in this case is not a definitive answer to the exact number of pathways as more parameters typically lead to a better fit.

To minimize the number of fitting parameters, the unique field dependence of the relaxation pathways was considered. A simultaneous fit, global fit, which links together some of the parameters for zero and 200 mT DC field measurements, was performed for the $HoLu_2N@C_{80}$ data (Fig. 4.9). Best fit parameters are shown in Table 4.2.

In Eq. 2.23 for a non-Kramers ion the only field dependent parts are the quantum tunneling and direct scattering. Therefore, in the fit process, the parameters of Raman scattering were linked to being the same for both zero field and 200 mT field measurements.

The fits converge to two main scenarios. First one with lower χ^2 where larger τ's are attributed only to the increased quantum tunneling time with no contributions from direct processes. The second one, with greater χ^2, cancels the contribution from tunneling at an applied field and includes direct scattering.

QTM + Raman + Direct Eq. 4.6

		χ^2	τ_{QTM} (ms)	A	C	n
$HoLu_2N@C_{80}$	0 T	7.06	0.95	0 (h)	2.2	3.94
	200 mT		12.5	0		
	0 T	10.9	0.91	0 (h)	1.13	4.2
	200 mT		inf (h)	45		

Table 4.2. Parameters of a simulations fits for magnetization relaxation times of $HoLu_2N@C_{80}$ at zero and 200 mT constant magnetic field with Eq. 4.6. The acronym (h) indicates the parameter being held during the fits while the parameters for Raman (C, n) are linked together for both fields.

Considering all the different types of fits above, our picture also matches with previous studies on $HoSc_2N@C_{80}$ indicating the relaxation process to consist of quantum tunneling and Raman processes. The effect of the diamagnetic ion is mainly essential for the zero field magnetization relaxation time τ. The zero field relaxation time of $HoSc_2N@C_{80}$ was inferred from χ'' curve found in the supplementals [66].

4.7. Switching Molecular Conformation with the Torque on a Single Magnetic Moment

The model of magnetization used in the following paper [59] is discussed in details in Chapter 3. The citations are stand-alone.

Switching Molecular Conformation with the Torque on a Single Magnetic Moment

Aram Kostanyan,[1,*] Rasmus Westerström,[1,2] Yang Zhang,[3] David Kunhardt,[3] Roland Stania,[1,†] Bernd Büchner,[3]
Alexey A. Popov,[3] and Thomas Greber[1,‡]
[1]*Physik-Institut, Universität Zürich, Winterthurerstrasse 190, CH-8057 Zürich, Switzerland*
[2]*Division of Synchrotron Radiation Research, Institute of Physics, University of Lund, SE-221 00 Lund, Sweden*
[3]*Leibniz Institute of Solid State and Materials Research, Dresden, D-01069 Dresden, Germany*

(Received 23 June 2017; revised manuscript received 26 October 2017; published 5 December 2017)

For the endohedral fullerene molecule $HoLu_2N@C_{80}$, it is shown that the endohedral $HoLu_2N$ unit may be oriented in a magnetic field. The Ho magnetic moment is fixed in the strong ligand field and aligns along the holmium-nitrogen axis. The torque of a magnetic field on the Ho magnetic moment leads to a hopping bias of the endohedral unit inclining to an orientation parallel to the externally applied field. This endohedral cluster distribution remains frozen below the onset of thermally induced rotation of the endohedral units. We derive an analytical statistical model for the description of the effect that scales below 7 T with the square of the external field strength, and that allows us to resolve the freezing temperature of the endohedral hopping motion. The freezing temperature is around 55 K and depends on the cooling rate, which in turn determines an activation energy for the hopping motion of 185 meV and a prefactor of $1.8 \times 10^{14}\ \mathrm{s}^{-1}$. For $TbSc_2N@C_{80}$ we find the same behavior with a 3.5% higher freezing temperature.

DOI: 10.1103/PhysRevLett.119.237202

The needle of a compass easily orients in a magnetic field because the torque scales with the sum of the electronic moments that are frozen in the lattice of the ferromagnetic needle. Still, magnetic moments of single atoms may be oriented and if the torque is transferred to the surrounding of the moment, as it is a molecule or a crystal, macroscopic rotation may result as well. In order to search for this orientation effect in the single atom limit, the ratio X between Zeeman energy and thermal energies $\mu B/k_B T$ has to be considered. For an atomic moment μ of 10 μ_B and a magnetic field of 1 T, X is larger than one below 7 K. This scaling argument limits expectations to see B field induced rotation due to a single paramagnetic atom. For example, the alignment of rare-earth-containing liquid crystals in B fields of about 1 T and above room temperature [1] must be a cooperative phenomenon, where more than one moment is involved. For isolated paramagnetic atoms in molecules, so far, no changes of the molecular conformation upon application of a magnetic field have been demonstrated. Here we report the alignment of the endohedral unit of $HoLu_2N@C_{80}$ [Fig. 1(a)] in an externally applied magnetic field. With careful field and temperature dependent magnetization measurements, a single magnetic moment effect on the molecular conformation is shown. The endohedral unit is subject to thermally activated hop rotation between equivalent low energy conformations [2,3], way below the freezing temperature of the carbon cages in a solid, which is 250 K for the case of solid C_{60} [4]. The magnetic field exerts a torque on the Ho^{3+} ion that is transferred to the endohedral unit because of the magnetic anisotropy, i.e., the alignment of the Ho magnetic moment in a strong ligand field, that is the base of single molecule [5,6] and single atom magnetism [7,8].

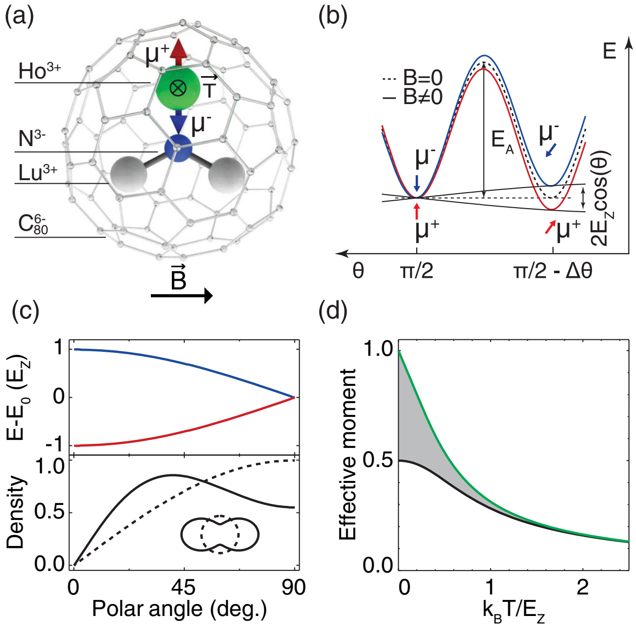

FIG. 1. (a) Ball-and-stick model of $HoLu_2N@C_{80}$. A $\vec{B}$ field exerts a torque $\vec{T}$ on the Ho magnetic moment $\vec{\mu}$. (b) The energy barrier E_A separates preferred orientations separated by $\Delta\theta$, while the Zeeman energy imposes a bias for magnetic moments parallel to the $\vec{B}$ field. (c) (top) Zeeman splitting and (bottom) angular density distribution dependence on the polar angle. The equilibrium angular density distribution for $E_Z = 0$ (dashed line) and $k_BT/E_Z = 1/2$ (solid line) are shown. The inset is the polar diagram of the two distributions. (d) Effective magnetic moment in thermal equilibrium vs k_BT/E_Z for freely rotating endohedral units (green) and for frozen, isotropically distributed magnetic moments (black). The magnetization of in-field cooling should lie within the green and the black curves in the shaded area.

$HoLu_2N@C_{80}$ endofullerenes were produced by arc-discharge synthesis using corresponding metal oxides and guanidine thiocyanate as the nitrogen source. The resultant soot was preextracted with acetone and further Soxhlet-extracted with CS_2. The separation of different fullerenes was performed by two-step high pressure liquid chromatography. The complete separation of $HoLu_2N@C_{80} - I_h$ from $Lu_3N@C_{80} - I_h$, I_h being the most abundant isomer with icosahedral symmetry, was not possible without significant loss of material; thus, the sample used for this Letter contained 20% of diamagnetic $Lu_3N@C_{80} - I_h$ [2]. Hereafter we will omit the isometric label I_h.

The magnetization measurements were performed in a Quantum Design MPMS3 Vibrating Sample Magnetometer (VSM). The sample is drop cast from toluene solution [9] that results in a black powder, and from the saturation magnetization we calculate a mass of 0.5 mg $HoLu_2N@C_{80}$. A temperature independent diamagnetic background of -3×10^{-8} Am^2/T was inferred from the low temperature magnetization data between 5 and 7 T.

Figure 1(a) shows the model of $HoLu_2N@C_{80}$. The endohedral unit consists of a triangle with 3 trivalent rare earth ions on its vertices, in the present case two diamagnetic Lu^{3+} and one paramagnetic Ho^{3+} ion. In the center of the triangle sits a nitrogen 3^- ion that lifts the 17-fold degeneracy of the isotropic Ho $^5I_8$ Hund ground state. As for $HoSc_2N@C_{80}$ [6], the ground state assumes $J_z = \pm 8$ with a large nominal magnetic moment $\mu = 10\ \mu_B$, where the quantization axis aligns along the N-Ho axis. Point charge model calculations of the ligand field splittings indicate an energy difference $\Delta E/k_B$ of 300 K between the first excited state $J_z = \pm 7$ and the ground state $J_z = \pm 8$. Therefore, in the temperature range of our experiment, the magnetism is described with a single pseudospin $J_z = \pm 8$ [2]. Such axial anisotropy is found as well for Dy [9,10] and for Tb [11]. A magnetic field $\vec{B}$ exerts a torque $\vec{T} = \vec{\mu} \times \vec{B}$ on the Ho atom. The anisotropy of the ligand field, however, hinders the Ho magnetic moment from freely following the magnetic field, and the torque is transferred to the N-Ho bond that acts as a lever for the torque on the endohedral unit, and the carbon cage. The free rotation of the endohedral units and the molecules is hindered by the nonisotropic carbon cages that impose preferred endohedral orientations [2].

For the given magnetic moment density, magnetic dipole interaction between different molecules may be neglected above temperatures of 1 K [12].

A priori it cannot be decided on whether the endohedral units rotate with the crystal, with the cage, or within the cage. The reproducibility of the experiment excludes macroscopic changes in the sample, while the length of the lever, the lower coordination, and the activation energy E_A that we determine rather favor a picture where the endohedral unit moves inside the cage in an otherwise frozen sample. This is also in line with the higher temperatures at which the onset of molecular rotation in solid C_{60} was observed [4]. Based on molecular dynamics simulations the motion of the endohedral unit is a thermally activated hopping between symmetrically equivalent sites, i.e., conformations, in the C_{80} cage [2]. This picture is also corroborated by nuclear magnetic resonance experiments [13,14]. In Fig. 1(b) a simplified, one-dimensional scheme of a potential energy landscape is shown, where two minima are separated by E_A. The first minimum corresponds to conformations with the magnetic moment perpendicular to the magnetic field ($\theta = \pi/2$), while the second minimum is separated by the angle between two neighboring conformations $\Delta\theta$. In this second minimum, the two magnetic moments are split by a Zeeman energy of $\vec{\mu} \cdot \vec{B} = 2E_Z \sin(\Delta\theta)$, where $E_Z = \mu B$. At low temperatures the two states are not populated equally and the B field imposes a drag toward small polar angles, i.e., causes an orientation of the endohedral units. If, however, the activation energy $E_A \gg k_B T$, the system may not assume thermal equilibrium in the accessible time frame. In the top panel of Fig. 1(c) the polar angle dependence of the Zeeman energy is depicted for the two zero field ground states $\pm J_z$ with the energy scale E_Z. In the lower panel, the density of the moments as a function of the polar angle is shown for the isotropic distribution ($k_B T \gg E_Z$) and for $k_B T/E_Z = 1/2$. The statistical mechanics problem of the determination of the density and the corresponding average magnetic moment may be solved analytically. In Fig. 1(d) the isotropic and the equilibrium magnetizations are shown as a function of temperature. For the green equilibrium curve, the moments will orient collinear to the magnetic field at zero Kelvin. On the other hand, the saturation magnetization for the isotropic distribution of the moments reaches only half of the collinear case [15]. Therefore, we expect a magnetization between the equilibrium and the isotropic case [gray area in Fig. 1(d)], depending on whether the sample is cooled in zero field or in an externally applied magnetic field.

Figure 2(a) shows the effect of field induced orientation of Ho magnetic moments as expressed by the magnetic moment m of the sample. The black trace is the zero-field cooled magnetic moment m_z during warm-up in an applied field $\mu_0 H = 7$ T. The red trace, on the other hand, is the magnetic moment m_i as observed when the sample is cooled and warmed-up in an externally applied field ($\mu_0 H = 7$ T). Clearly, below a certain temperature, the zero-field cooled sample displays a lower magnetization than the in-field cooled sample. The effect depends on the applied magnetic field, and as we see later on the cool-down and warm-up rate $\pm\beta$ that was set for the data in Fig. 2 to $\pm\beta = 5 \times 10^{-2}$ K/s. Figure 2(b) shows the ratio of the magnetic moment between in-field and zero-field cooled sample m_i/m_z for different external magnetic fields. Above about 60 K the ratio m_i/m_z is one. Below this characteristic temperature, the hopping rates of the endohedral units drop, such that the equilibrium magnetization for the given temperature may not be obtained during the

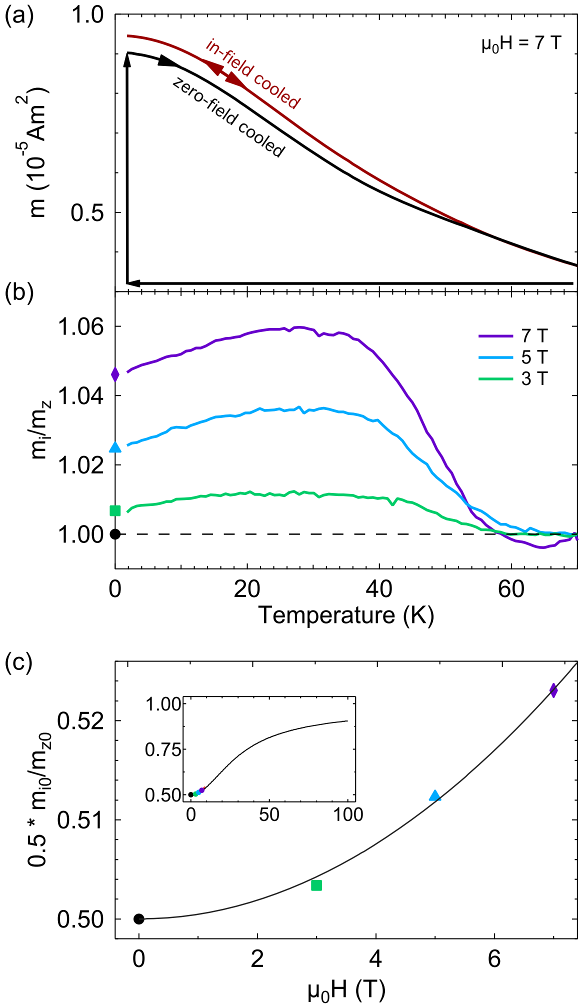

FIG. 2. (a) Temperature dependence of the magnetic moment m for zero-field cooled (black) and in-field cooled (red) $HoLu_2N@C_{80}$. (b) Ratio of the magnetic moment for in-field and zero-field cooled m_i/m_z for different externally applied magnetic fields (7 T, 5 T, 3 T). (c) $m_{i0}/m_{z0}/2$ extrapolated to 0 K. From the curvature of the parabola the Zeeman energy:k_BT_F ratio is inferred. Inset: Prediction for higher magnetic fields. Heating and cooling rate $\pm\beta = 5 \times 10^{-2}$ K/s K/s.

duration of the experiment. In the following, we will call this temperature the equilibrium freezing temperature T_F, at which the angular density distribution of the magnetic moments freezes. The zero Kelvin extrapolation $(m_i/m_z)_{T=0}$ increases with the externally applied field in a nonlinear fashion [see Fig. 2(c)]. For fields up to 7 T, we get a parabolic effect. Qualitatively, this can be understood by the effective magnetic torque, which is proportional to the external field and the magnetization that is, near zero, as well proportional to the external field. Using the second term $\propto B^2$ of the series expansion of the model in Fig. 1 $(m_i/2m_z)_{T=0}(B) = 1/2 + (aB)^2/24$ with $a = X_F/B = \mu/k_BT_F$. The experimental value of $a = (107 \pm 1) \times 10^{-3}$ T^{-1}. If we use the full analytical expression for the determination of a we get $(108.9 \pm 0.2) \times 10^{-3}$ T^{-1}. As it is shown in the inset of Fig. 2(c) the theory also predicts the orientation effect for large fields, where the effect flattens and approaches saturation.

If we want to determine T_F, we have to know the magnetic moment μ of the Ho atom. This can be obtained conveniently from the magnetization curves of zero-field cooled samples, as it was demonstrated for other noncollinear single-ion magnets [6,10,11]. The magnetization data in Fig. 3 were recorded at 1.8 K, well below the freezing temperature. If we apply a simultaneous fit to both magnetization curves in Fig. 3, where the number of molecules N and the magnetic moment μ have to assume the same value, and where we allow for the in-field cooled sample a freezing temperature T_F, we get $N = (2.02 \pm 0.005) \times 10^{17}$, $\mu = 9.55 \pm 0.02\ \mu_B$ and $T_F = 52.3 \pm 0.3$ K for $\beta = 5 \times 10^{-4}$ K/s. From data of a $TbSc_2N@C_{80}$ sample [16], we get $\mu = 9 \pm 0.02\ \mu_B$ and $T_F = 60.3 \pm 0.3$ K for $\beta = 5 \times 10^{-2}$ K/s. The nonisotropic angular distribution of the magnetic moments for the in-field cooled sample corresponds to the equilibrium distribution at T_F and is responsible for the excess magnetization. Considering that the freezing temperature depends on β (see below) this is in perfect agreement (better than 3%) with the parameter a from the data in Fig. 2. Furthermore, the difference curve between m_i and m_z indicates that the difference between the in field and zero field is not explained by a simple scaling and it is seen that the conformational change model with a field dependent freezing temperature describes the data very well.

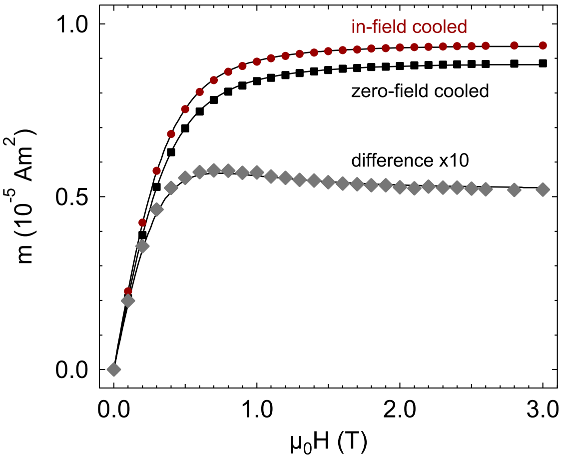

FIG. 3. Magnetization m vs externally applied magnetic field μ_0H of $HoLu_2N@C_{80}$ at 1.8 K (raw data). Both zero-field (black squares) and in-field 7 T (red circles) cooled data were fitted (solid lines) simultaneously with a model of isotropically (randomly) oriented Ho magnetic moment and an equilibrium distribution with a freezing temperature T_F. The fits yield 9.55 μ_B for the Ho magnetic moment and a T_F of 52.3 K for $B = 7$ T and $\beta = 5 \times 10^{-4}$ K/s. Grey diamonds are the difference between zero-field and in-field cooled. The solid line is the difference of the corresponding fits.

In order to determine the activation energy E_A [see Fig. 1(b)] and the attempt frequency ν for the endohedral hop rotation, temperature sweep-rate dependent measurements were performed. Figure 4(a) shows the in-field and zero-field cooled ratio m_i/m_z for three different temperature sweep rates β between 5×10^{-4} K/s and 5×10^{-2} K/s. As expected, for small β's the endohedral unit has more time to adopt equilibrium during in-field cooldown, resulting in smaller T_F's as shown in Fig. 4(b), and larger endohedral orientation. The T_F's are determined from magnetization curves at 1.8 K for corresponding β's as described above.

E_A and ν are obtained from a first order kinetics model. In this model, we assume that during a time interval Δt the equilibrium is approached exponentially:

$$m(t + \Delta t) = m(t) + \Delta m_E[1 - \exp(-\Delta t/\tau)], \qquad (1)$$

where $\Delta m_E = m_E(t + \Delta t) - m(t)$ is the deviation of the magnetization $m(t)$ at time t from the equilibrium magnetization m_E. The time constant τ is the average time between two hops and is described by a single barrier E_A. It has the form $\tau = (\nu \exp(-E_A/k_B T))^{-1}$, where ν is the attempt frequency and k_B is the Boltzmann constant. The best fit to the $T_F(\beta)$ data yields a barrier $E_A/k_B = (2145 \pm 20)$ K and $\nu = 1.8 \times 10^{14 \pm 0.15}$ s^{-1} where the confidence intervals are strongly correlated and taken at levels 10% above the χ^2 minimum between experiment and theory. The ratio between E_A and E_Z at 7 T is 47 which rationalizes the relatively high freezing temperatures.

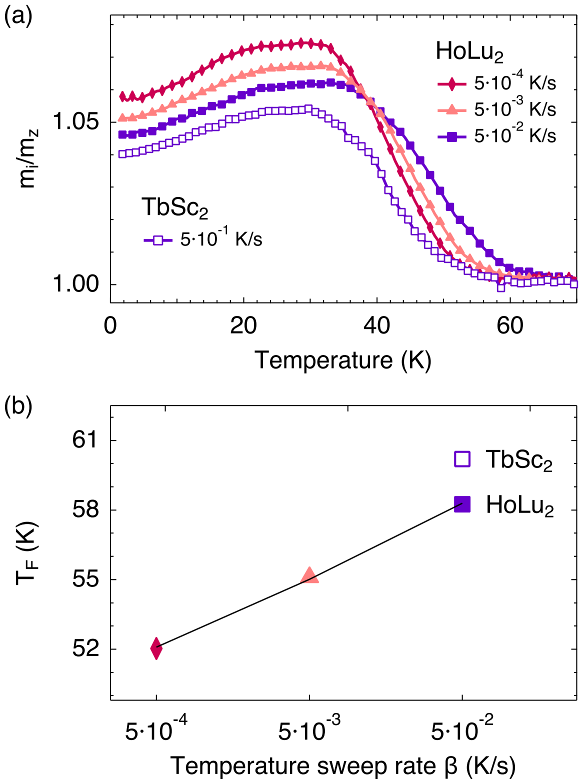

FIG. 4. (a) Ratio of magnetic moment for in-field and zero-field cooled m_i/m_z at different temperature sweep rates β for HoLu$_2$ (full symbols) and TbSc$_2$ (open symbols). (b) Freezing temperatures $T_F(\beta)$ [with corresponding symbols and colors from (a)] determined from fits of magnetization curves of the in-field cooled samples. The solid line is the best fit of first order kinetics for HoLu$_2$—with a barrier height $E_A/k_B = (2145 \pm 20)$ K and an attempt frequency $\nu = 1.8 \times 10^{14 \pm 0.15}$ s^{-1}.

The activation energy for the onset of endohedral rotation in C$_{80}$ for HoLu$_2$N (185 meV) compares well with Lu$_3$N (186 meV) as obtained from NMR [17], and studies for Sc$_3$N (78–150 meV) [3] This suggests an increase of E_A with the size of the endohedral cluster. The prefactor ν that is needed as well for a complete kinetic description is larger than the highest molecular vibration frequencies. This is not an inconsistency, large kinetic prefactors up to 10^{19} s^{-1} were, e.g., observed in desorption of alkane molecules on surfaces [18–20]. This may be an indication, that the one-dimensional two level picture as sketched in Fig. 1(b) is too simple. Rather, the large ν hints to the many degrees of freedom that are involved in the hopping of endohedral units in C$_{80}$ [2]. The extracted kinetic parameters will allow the test of temperature dependent molecular dynamics simulations, and the study of steric effects due to different rare earth ion sizes. For example, the difference in freezing temperature between HoLu$_2$ and TbSc$_2$ in Fig. 4 indicates—under the assumption of the same prefactor—a 3.5% higher activation energy for the Tb compound. The kinetic parameters are also needed if the orientation effect shall be enhanced by high magnetic field pulses, as well as if the effect shall be applied for the orientation of the easy axis in endohedral single molecule magnets.

In conclusion, we have shown that endohedral units like HoLu$_2$N or TbSc$_2$N may be rotated inside C$_{80}$ molecules by the application of magnetic fields. The Zeeman energy enables the rotation and its measurement of the effect in the magnetization. The ratio X_F between the Zeeman energy and thermal energies at freezing controls the degree of orientation, where T_F is governed by a characteristic time τ that describes the equilibration time. The presented conformational change model may be applied to other endohedral molecules containing a magnetic moment, and the corresponding activation energies will provide insight into the relation between the size of the endohedral cluster and its binding.

We gratefully acknowledge financial support from the Swiss National Science Foundation (SNF Projects No. 206021_150784, No. 200021L_147201, and No. 200020_153312), the European Research Council (ERC) under the European Union's Horizon 2020 research and innovation programme (Grant No. 648295 "GraM3") and the Swedish Research Council (Grant No. 2015-00455) and Sklodowska Curie Actions co-founding Project No. INCA 600398.

[*] Corresponding author.
aram@physik.uzh.ch
[†] Center for Artificial Low Dimensional Electronic Systems, Institute for Basic Science (IBS), Pohang, Republic of Korea.
[‡] greber@physik.uzh.ch

[1] K. Binnemans, Y. G. Galyametdinov, R. Van Deun, D. W. Bruce, S. R. Collinson, A. P. Polishchuk, I. Bikchantaev, W. Haase, A. V. Prosvirin, L. Tinchurina, I. Litvinov, A. Gubajdullin, A. Rakhmatullin, K. Uytterhoeven, and L. Van Meervelt, Rare-earth-containing magnetic liquid crystals, J. Am. Chem. Soc. **122**, 4335 (2000).

[2] Y. Zhang, D. Krylov, S. Schiemenz, M. Rosenkranz, R. Westerström, J. Dreiser, T. Greber, B. Büchner, and A. Popov, Cluster-size dependent internal dynamics and magnetic anisotropy of Ho ions in $HoM_2N@C_{80}$ and $Ho_2MN@C_{80}$ families ($M = Sc$, Lu, Y), Nanoscale **6**, 11431 (2014).

[3] T. Huang, J. Zhao, M. Feng, A. A. Popov, S. Yang, L. Dunsch, and H. Petek, A multi-state single-molecule switch actuated by rotation of an encapsulated cluster within a fullerene cage, Chem. Phys. Lett. **552**, 1 (2012).

[4] P. A. Heiney, J. E. Fischer, A. R. McGhie, W. J. Romanow, A. M. Denenstein, J. P. McCauley Jr., A. B. Smith, and D. E. Cox, Orientational ordering transition in solid C_{60}, Phys. Rev. Lett. **66**, 2911 (1991).

[5] N. Ishikawa, M. Sugita, T. Ishikawa, S. Y. Koshihara, and Y. Kaizu, Mononuclear lanthanide complexes with a long magnetization relaxation time at high temperatures: A new category of magnets at the single-molecular level, J. Phys. Chem. B **108**, 11265 (2004).

[6] J. Dreiser, R. Westerström, Y. Zhang, A. A. Popov, L. Dunsch, K. Krämer, S. Liu, S. Decurtins, and T. Greber, The metallofullerene Field-induced single-ion magnet $HoSc_2N@C_{80}$, Chem. Eur. J. **20**, 13536 (2014).

[7] F. Donati, S. Rusponi, S. Stepanow, C. Wäckerlin, A. Singha, L. Persichetti, R. Baltic, K. Diller, F. Patthey, E. Fernandes, J. Dreiser, Ž. Šljivančanin, K. Kummer, C. Nistor, P. Gambardella, and H. Brune, Magnetic remanence in single atoms, Science **352**, 318 (2016).

[8] F. D. Natterer, K. Yang, W. Paul, P. Willke, T. Choi, T. Greber, A. J. Heinrich, and C. P. Lutz, Reading and writing single-atom magnets, Nature (London) **543**, 226 (2017).

[9] R. Westerström, J. Dreiser, C. Piamonteze, M. Muntwiler, S. Weyeneth, H. Brune, S. Rusponi, F. Nolting, A. Popov, S. Yang, L. Dunsch, and T. Greber, An endohedral single-molecule magnet with long relaxation times: $DySc_2N@C_{80}$, J. Am. Chem. Soc. **134**, 9840 (2012).

[10] R. Westerström, J. Dreiser, C. Piamonteze, M. Muntwiler, S. Weyeneth, K. Krämer, S.-X. Liu, S. Decurtins, A. Popov, S. Yang, L. Dunsch, and T. Greber, Tunneling, remanence, and frustration in dysprosium-based endohedral single-molecule magnets, Phys. Rev. B **89**, 060406 (2014).

[11] F. Liu, C.-L. Gao, Q. Deng, X. Zhu, A. Kostanyan, R. Westerström, S. Wang, Y.-Z. Tan, J. Tao, S.-Y. Xie, A. A. Popov, T. Greber, and S. Yang, Triangular monometallic cyanide cluster entrapped in carbon cage with geometry-dependent molecular magnetism, J. Am. Chem. Soc. **138**, 14764 (2016).

[12] F. L. Pratt, E. Micotti, P. Carretta, A. Lascialfari, P. Arosio, T. Lancaster, S. J. Blundell, and A. K. Powell, Dipolar ordering in a molecular nanomagnet detected using muon spin relaxation, Phys. Rev. B **89**, 144420 (2014).

[13] J. Zhang and H. Dorn, NMR studies of the dynamic motion of encapsulated ions and clusters in fullerene cages: A wheel within a wheel, Fullerenes, Nanotubes, Carbon Nanostructures **22**, 35 (2014).

[14] T. Heine, K. Vietze, and G. Seifert, ^{13}C NMR fingerprint characterizes long time-scale structure of $Sc_3N@C_{80}$ endohedral fullerene, Magn. Reson. Chem. **42**, S199 (2004).

[15] J. Dreiser, K. S. Pedersen, C. Piamonteze, S. Rusponi, Z. Salman, M. E. Ali, M. Schau-Magnussen, C. A. Thuesen, S. Piligkos, H. Weihe, H. Mutka, O. Waldmann, P. Oppeneer, J. Bendix, F. Nolting, and H. Brune, Direct observation of a ferri-to-ferromagnetic transition in a fluoride-bridged $3d-4f$ molecular cluster, Chem. Sci. **3**, 1024 (2012).

[16] R. Stania, Ph.D. thesis, Universität Zürich, 2016.

[17] W. Fu, X. Wang, H. Azuremendi, J. Zhang, and H. C. Dorn, ^{14}N and ^{45}Sc NMR study of trimetallic nitride cluster $(M_3N)^{6+}$ dynamics inside a icosahedral C_{80} cage, Chem. Commun. (Cambridge) **47**, 3858 (2011).

[18] C. T. Campbell, L. Árnadóttir, and J. R. V. Sellers, Kinetic prefactors of reactions on solid surfaces, Z. Phys. Chem. (Muenchen, Ger.) **227**, 1435 (2013).

[19] A. J. Gellman and K. R. Paserba, Kinetics and mechanism of oligomer desorption from surfaces: *n*-Alkanes on graphite, J. Phys. Chem. B **106**, 13231 (2002).

[20] K. R. Paserba and A. J. Gellman, Effects of conformational isomerism on the desorption kinetics of *n*-alkanes from graphite, J. Chem. Phys. **115**, 6737 (2001).

5. $Dy_2GdN@C_{80}$ and $Dy_2ScN@C_{80}$

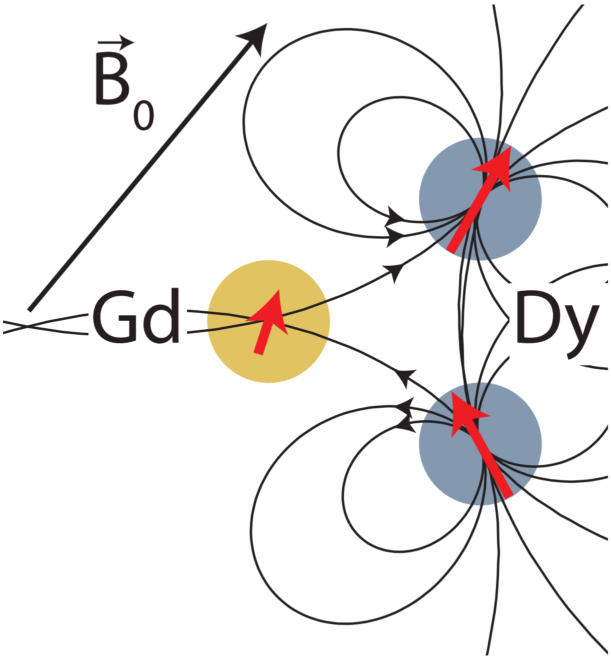

Figure 5.1. Sketch of the endohedral unit of $Dy_2GdN@C_{80}$, cut parallel to the endohedral plane containing the magnetic ions. $\vec{B}_0$ is the external magnetic field. While the Dy magnetic moments align axially to the central nitrogen ion, the Gd magnetic moment is influenced by the external magnetic field and the magnetization imposed by the two Dy neighbors.

5.1. Introduction

In the previous chapter, we looked at the influence of the diamagnetic component in the single paramagnetic ion endohedral unit of $HoLu_2N@C_{80}$ and $HoSc_2N@C_{80}$ (Chapter 4). In this chapter, we explore the interplay of the two different paramagnetic species in $Dy_2GdN@C_{80}$ as shown in Fig. 5.1 and compare it with a molecule containing two paramagnetic ions of the same species $Dy_2ScN@C_{80}$.

The magnetization dynamics is studied using AC susceptometry and DC time-dependent magnetization measurements in the temperature range between 400 mK and 25 K. The lowest temperature was achieved using a continuous flow ^{3}He cryostat. At the end of the chapter, the draft of the upcoming paper on the comparison of $Dy_2GdN@C_{80}$ and $Dy_2ScN@C_{80}$ is presented. The characteristic relaxation times τ of $Dy_2GdN@C_{80}$ are compared with $Dy_2ScN@C_{80}$.

In the draft, the magnetization of $Dy_2GdN@C_{80}$ is disentangled to its components originating from Dy and Gd by comparing field dependent magnetization of the molecule measured with X-ray magnetic circular dichroism (XMCD) (element specific) and SQUID (integral magnetization). This comparison is complimented with XMCD sum rule analysis. The sample preparations for SQUID and X-ray measurements are discussed in Appendix B.

$Dy_2GdN@C_{80}$ (Fig. 5.1) represents another member of nitride-cluster fullerenes (NCFs) [19–21]. Three triple ionized paramagnetic ions, two Dy^{3+} and one Gd^{3+}, are coupled via a negatively charged nitrogen N^{3-} in a C_{80}^{-6} cage. Previous studies on $Dy_2ScN@C_{80}$ showed a strong anisotropy of the Dy moments and an opening of a hysteresis loop and long magnetization relaxation times [24].

The ligand field of the central negative nitrogen lifts the Hund's ground state $^6H_{15/2}$ of Dy^{3+}. For Gd^{3+} $^8S_{7/2}$ no ligand field splitting is expected because the half filled $4f^7$ shell of Gd^{3+} has a spherical symmetry. In the ground state of the ligand field, the maximum $J_z = \pm 15/2$ is favored for Dy. Dy being axially symmetric has a nominal magnetic moment of $\mu = 10\ \mu_B$ $(2S_z + L_z)$ which points along the Dy-N axis. In contrary, Gd has an isotropic moment of $\mu = 7\ \mu_B$ which is allowed to point in the direction of the total magnetic field at the site of the Gd atom. The total magnetic field is given by the sum of the external field, the dipolar field and the exchange field B_x of the two Dy neighbors. The B_x is defined as the ratio of the exchange energy and the magnetic moment of the ion. The exchange interaction depends on the spatial and energy overlap. For Gd the $B_x = 0$ as there is no energy overlap with the two Dy ions.

The ground state of the system in the absence of an external magnetic field is shown in Fig. 5.9 (neglecting B_x). The two Dy ions do energetically favor a ferromagnetic configuration. This configuration induces a dipolar field of 180 mT parallel to the Dy-Dy axis at the site of the Gd ion inducing a preferred orientation for the Gd magnetic moment. While the excited state, the antiferromagnetic configuration of Dy moments, induces a stronger dipolar field of $\approx$ 720 mT perpendicular to the Dy-Dy axis. The goal of the XMCD element specific magnetization measurements is to identify the deviations of the endohedral Gd moments from those of free ions, which is described by the Brillouin function.

5.2. Field and Temperature Dependent Magnetization

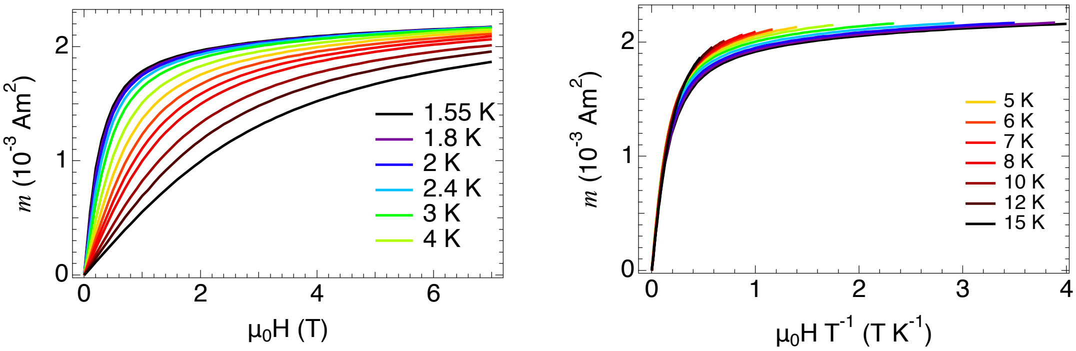

Figure 5.2. (a) Field dependent magnetization m of $Dy_2GdN@C_{80}$ measured between 1.8 K and 15 K 17 steps. (b) The reduced magnetization $Dy_2GdN@C_{80}$ with corresponding color code. The average field scan rate was 5.4 mT/s between 5 and -5 T.

Field-dependent magnetization m and reduced magnetization $m(X = \frac{\mu_0 H}{k_B T})$ for $Dy_2GdN@C_{80}$ are shown in Fig. 5.2. The measurements were performed with a SQUID magnetometer (Sec. 2.2) in the temperature range between 1.55 K and 15 K in 17 steps and field scan rate of 5.4 mT/s. A diamagnetic background of -5.8×10^{-8} Am^2/T was inferred both from temperature dependent magnetization measurements (Sec. 6.5) and the χ^2 mapping discussed at the end of the chapter (Fig. 5.10 inset). The deviation of the reduced magnetization from a single line is an indication of the non-temperature dependent interactions. The reduced magnetizations of a Brillouin function overlap for different temperatures. The deviation from temperature scaling in $Dy_2GdN@C_{80}$ is demonstrated in Fig. 5.2 and is an indication of the interaction, dipolar and exchange, of the paramagnetic ions in the endohedral unit.

As shown in Fig. 5.3 (a) $Dy_2GdN@C_{80}$ shows a tiny hysteresis with a coercive field of $\approx$ 10 mT at 1.9 K with a scan rate of 5.4 mT/s. The hysteresis stays open until 2.5 K. At below 1.9 K, the hysteresis opens further and reaches a coercive field of $\approx$ 200 mT at 420 mK (see Fig. 5.11).

To understand which atomic species, Dy or Gd, have the most impact on the hysteresis, element-specific magnetization were measured at X-Treme beamline, SLS

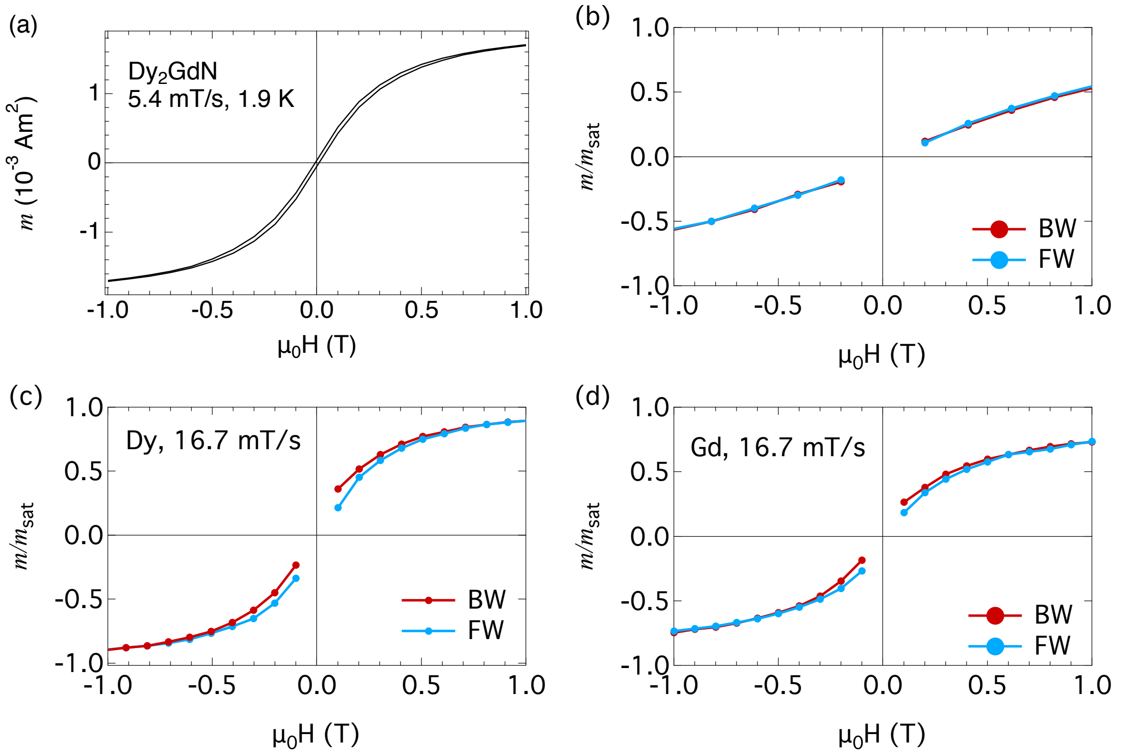

Figure 5.3. (a) Field dependent magnetization measured with a SQUID magnetometer at 1.9 K with field scan rate of 5.4 mT/s. XMCD magnetization of (b) GdCl, (c) endohedral Dy and (d) endohedral Gd. The symbols are the size of the error bars.

(Sec. 2.3). The XMCD of endohedral Gd and Dy along with GdCl are shown in Fig. 5.3. The curves were constructed from field dependent spectra (Fig. 5.10) $[(I^+_{E_2} - I^+_{E_1}) - (I^-_{E_2} - I^-_{E_1})]$, where E_1 and E_2 are the pre-edge and XMCD-max photon energies. For Gd E_1 and E_2 are 1173 eV and 1182.6 eV respectively, and for Dy they are 1184.5 eV and 1291.5 eV. The temperature of the XAS and XMCD measurements were determined to be 1.95 ± 0.05 K using a χ^2 mapping of XMCD data and SQUID magnetization which is discussed in details in Sec. 5.7 for $Dy_2GdN@C_{80}$ and 3.7 K for $GdCl_3$.

XMCD magnetization has an advantage that the magnetization measurements can be performed while changing the magnetic field in contrast to SQUID magnetometry where the measurements are performed after the stabilization. However, it also a disadvantage as well. The X-ray radiation destroys the magnetization state of the spins [24, 71, 72].

Both endohedral Dy and Gd show a small opening of magnetization around zero field as shown in Fig. 5.3 (c) and (d) although Dy has a slightly bigger hysteresis. The smaller hysteresis of Gd compared to Dy could be explained by Gd being more prone to the X-ray induced demagnetization [71]. The field scan rate for XMCD

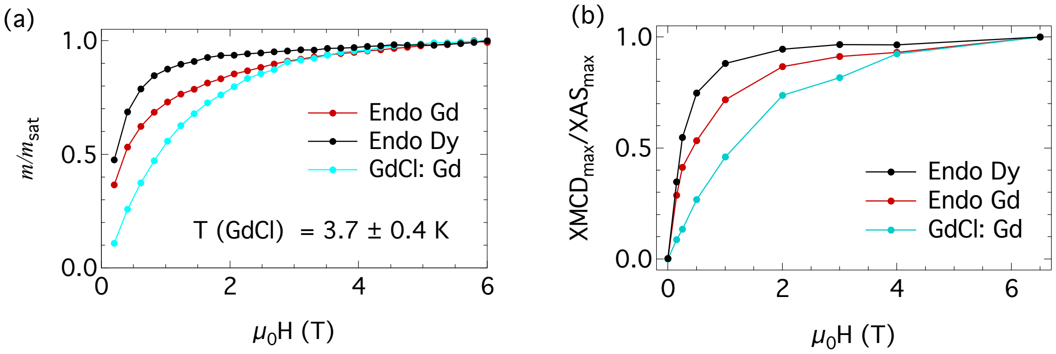

Figure 5.4. (a) XMCD magnetization of endohedral Dy and Gd, and $GdCl_3$. A Brillouin function to $GdCl_3$ reveals a temperature of 3.7 ± 0.4 K. (b) The maximum of XMCD normalized over the maximum of XAS measured at 0.15 T, 0.25 T, 0.5 T, 1 T, 2 T. 3 T, 4 T and 6.5 T magnetic field values. The data was normalized to one for 6.5 T.

measurements was 16.7 mT/s. As a comparison for measurement accuracy the magnetization curve of $GdCl_3$ is shown in Fig. 5.3. As expected from an isotropic spin, which follows a Brillouin function, there is no visible opening.

Figure 5.4 shows field dependent XMCD magnetization of endohedral Dy and Gd, and Gd of the $GdCl_3$. The magnetization curves are normalized to one at 6.5 T. The magnetization of Dy increases faster at smaller field values followed by a small slope. Endohedral Gd, on the other hand, does not increase that fast but at higher fields, it has a bigger slope. There is a significant difference between endohedral Gd and Gd in $GdCl_3$. As discussed in the next paragraph one of the reasons is the higher temperature of $GdCl_3$. However, endohedral Gd does not follow a Brillouin function also if the temperature is left a free parameter as shown in Sec. 5.7.

$GdCl_3$ was intended to be used as a thermometer. The temperature could be extracted by fitting a Brillouin function with corresponding parameters. However, the fits indicate at a temperature of 3.7 ± 0.4 K which is not the same value as obtained for the molecules on the same sample holder. As seen from Fig. B.4, the $GdCl_3$ sample has a visible thickness. $GdCl_3$ could be heated from X-rays more than the endofullerenes because of different thermal contact or energy absorption. The power of the X-ray beam ≈ 40 μW on ≈ 3 mm^2 was calculated from the beam flux and energy [42].

XAS and XMCD spectra of $Dy_2GdN@C_{80}$ were measured at applied field values of 0.15 T, 0.25 T, 0.5 T, 1 T, 2 T. 3 T, 4 T, and 6.5 T for the $M_{4,5}$ edges of endohedral Gd and Dy, and Gd of the $GdCl_3$. The maximum of XMCD normalized over the maximum of XAS for the previously mentioned magnetic field values is shown in Fig. 5.4. This also follows the trend of the magnetization curves.

The polarization dependent XAS and XMCD spectra were used for sum rule analysis discussed in the next section.

5.3. Sum Rules

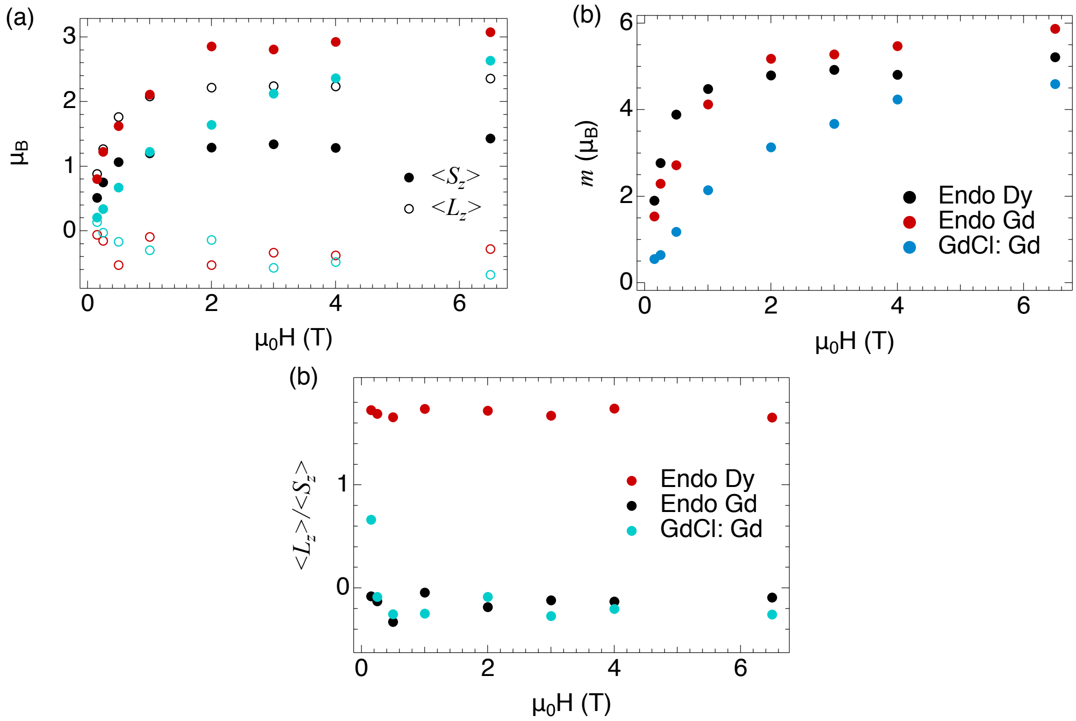

Figure 5.5. Sum rule analysis of endohedral Dy and Gd, and $GdCl_3$ performed for 0.15 T, 0.25 T, 0.5 T, 1 T, 2 T. 3 T, 4 T and 6.5 T magnetic field values: (a) spin $\langle S_z \rangle$ and orbital $\langle L_z \rangle$ magnetic moments, (b) average magnetic moments m $(2\langle S_z \rangle + \langle L_z \rangle)$ and (c) the $\langle L_z \rangle / \langle S_z \rangle$ ratio. The temperature of endofullerenes was 1.95 K and $GdCl_3$ 3.7 K. The color coding is the same for all the three graphs.

Figure 5.5 shows the sum rule analysis performed for endohedral Dy and Gd, and $GdCl_3$ for 0.15 T, 0.25 T, 0.5 T, 1 T, 2 T. 3 T, 4 T and 6.5 T magnetic field values [38, 39]. The temperature for endofullerenes was ≈ 1.95 K as obtained from χ^2 mapping (Sec. 5.7) and 3.7 K for $GdCl_3$ calculated from Brillouin fits of the magnetization data.

Figure 5.5 (a) shows the average expectation values for spin $\langle S_z \rangle$ and orbital $\langle L_z \rangle$ magnetic moments. The background XAS spectra at the corresponding field values were subtracted, and the sum rule analysis was performed. The TEY of XAS spectra were normalized by the current on a golden mesh placed on the beam path (Sec. 2.3). Neither the gold mesh current normalization with absorption coefficient nor the Teramura correction for the magnetic dipole operator $\langle T_z \rangle$ were performed [40].

The average magnetic moments m $(2\langle S_z\rangle + \langle L_z\rangle)$ are shown in Fig. 5.5 (b). They show the same behavior as the XMCD magnetization curves (Fig. 5.4). The magnetic moment of endohedral Dy gets very close to its theoretical value 5 μ_B of isotropically distributed spins 10 μ_B. The moment of $GdCl_3$ is smaller than endohedral Gd, most likely because of higher temperature.

5.4. AC Susceptibility

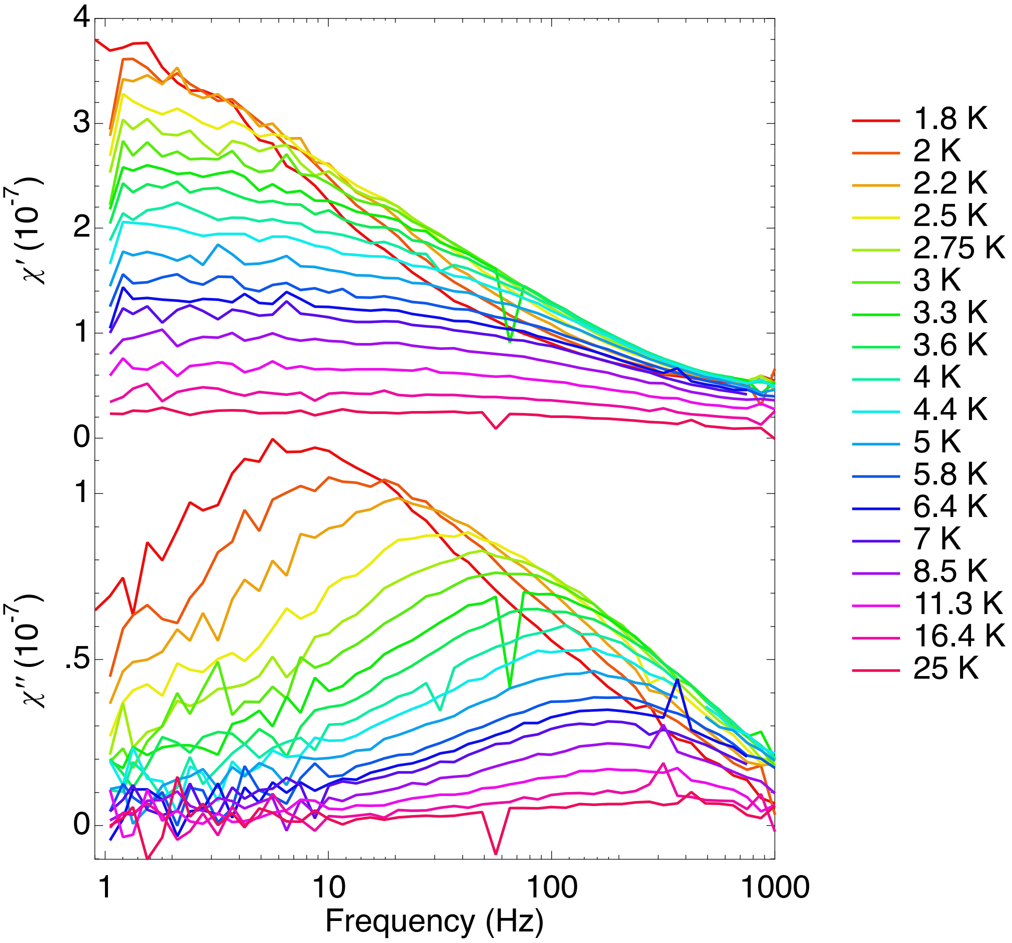

Figure 5.6. Real (in-phase) (top) and imaginary (out-of-phase) (bottom) part of AC susceptibility of $Dy_2GdN@C_{80}$ measured at zero (< 0.5 mT) applied magnetic field in the temperature range of 1.8 K to 25 K in 18 steps. AC driving field amplitude was 0.25 mT.

The fast relaxation of magnetization is possible to study with AC susceptometry (Sec. 2.2.2). Figure 5.6 shows the real χ' and imaginary χ'' components of the AC susceptibility of $Dy_2GdN@C_{80}$ at zero static magnetic field in the temperature range between 1.8 K and 25 K. The measurements started after oscillating the magnetic field to zero from high field values to achieve the smallest remnant field (< 0.5 mT).

χ' and χ'' show the typical behavior of a resonance discussed in detail in Sec. 2.2.2. The width of the χ'' curves is an indication of a distribution of relaxation times τ instead of one. The magnetization relaxation times τ extracted from Fig. 5.6 (Sec. 5.6) are shown in Fig. 5.8.

What sets apart the AC susceptibility measurements of $Dy_2GdN@C_{80}$ from the other two paramagnetic ion containing molecules studied in this thesis $Ho_2LuN@C_{80}$ and $Tb_2ScN@C_{80}$, is the relatively weak temperature dependence. A signal can be measured in a wider temperature range than for other molecules.

The magnetization relaxation times τ shown in Fig. 5.8 were extracted from the AC susceptibility measurements by performing a simultaneous fit to the real χ' and imaginary χ'' components to Eq.'s 2.5 and 2.6, respectively.

5.5. Temperature Dependent Magnetization Relaxation

The hysteresis of the magnetization curves indicates slow magnetization relaxation. This allows the study of magnetization dynamics by measuring time-dependent magnetization relaxation shown in the semi-log Fig. 5.7. The measurements were performed in the temperature range between 400 mK and 1.2 K using a ^{3}He cryostat (2.2.1). The decay of magnetization for $Dy_2GdN@C_{80}$ is compared with $Dy_2ScN@C_{80}$ which shows a significantly slower initial decrease of magnetization. $Dy_2ScN@C_{80}$ also has a larger coercive field value as shown in Fig. 5.11.

$Dy_2GdN@C_{80}$ shows a fast decay of magnetization directly after the field reaches zero. The magnetic field was ramped down to 3 mT from 7 T in 350 s. The details of the behavior of the superconducting magnet are discussed in Appendix D. The rate of the decay slows down significantly after one day. The decay shows an unusually strong non-exponential time dependence for SMMs which can be caused by various perturbations. The time-dependent perturbations from the neighboring spins can speed up the initial decay. For dipolar interaction between neighboring spins, the decay shows a square root behavior ($m(t) = m_0[1 - (t/\tau)^{1/2}]$) [49].

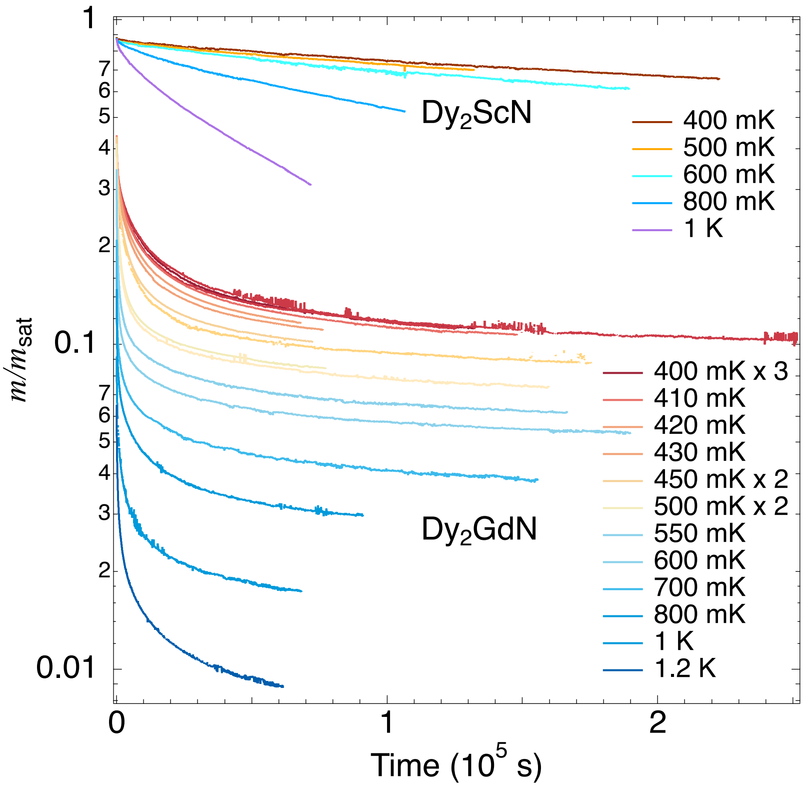

Figure 5.7. Relaxation of magnetization m normalized by saturation magnetization m_{sat} of Dy$_2$ScN@C$_{80}$ and Dy$_2$GdN@C$_{80}$ measured after stabilization of the field. The field was decreased from 7 T to zero in 350 s. Measurements were performed in the temperature range of 400 mK to 1.2 K using a ^{3}He cryostat. The multiplier factor in the legends indicates the number of repeated measurements for given temperature.

The comparison between Dy$_2$GdN@C$_{80}$ and Dy$_2$ScN@C$_{80}$ shows that the additional isotropic Gd has a dramatic effect on the decay. Apparently, perturbations that trigger the decay of the magnetization are mediated via the Gd ions and transferred to Dy as well. This has a catastrophic effect on both the lifetime and coercive field (see Fig. 5.11).

Because it was not possible to achieve a good fit of the time decay of magnetization with neither single or double exponential fits, the magnetization data was fitted with a triple exponential (Eq. 5.1) and the characteristic relaxation times are discussed in the next section.

$$m(t) = m_{0,1}\, e^{t/\tau_1} + m_{0,2}\, e^{t/\tau_2} + m_{0,3}\, e^{t/\tau_3}. \tag{5.1}$$

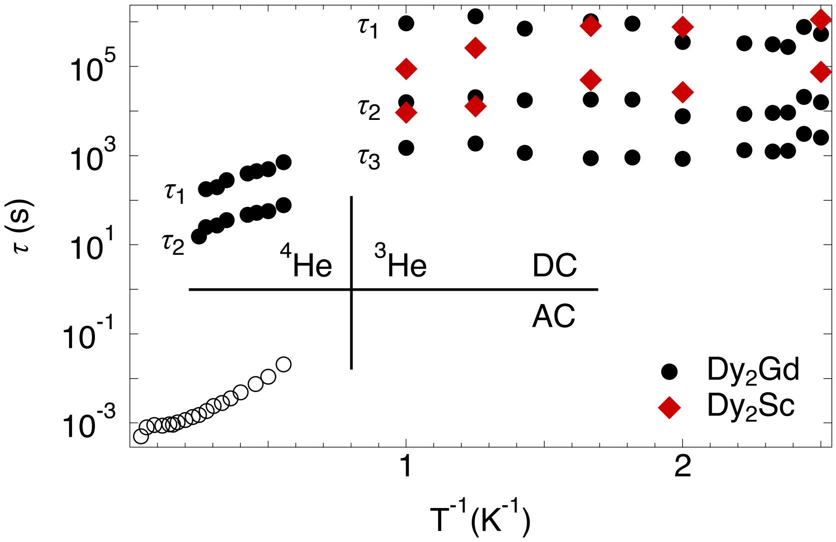

Figure 5.8. Magnetization relaxation time τ as a function of the reciprocal temperature. Full symbols correspond to DC measurements from Fig. 5.7 and open symbols correspond to AC measurements (Fig. 5.6) (black $Dy_2GdN@C_{80}$, red $Dy_2ScN@C_{80}$).

5.6. Magnetization Relaxation Times

The magnetization lifetimes τ of $Dy_2GdN@C_{80}$ and $Dy_2ScN@C_{80}$ are shown in Fig. 5.8. The short τ's for $Dy_2GdN@C_{80}$ (open black circles) were extracted from the AC susceptibility measurements (Fig. 5.6). The longer τ's were taken from exponential fits to the time-dependent magnetization measurements shown in Fig. 5.7.

At the lowest temperature of 400 mK the two longest τ's (τ_1 and τ_2) of $Dy_2GdN@C_{80}$ match fairly well with $Dy_2ScN@C_{80}$. This equality deviates at temperatures above 1 K. However, at 1 K the lifetime of a ^{3}He cycle is much shorter than magnetization lifetime which could induce large errors in the fits (Fig. 5.7).

The dramatic difference in time-dependent magnetization between $Dy_2GdN@C_{80}$ and $Dy_2ScN@C_{80}$ is likely caused by the 3rd and fastest τ_3 which indicates the initial fast decay of magnetization.

5.7. Draft: Dy_2X

Experimental

$Dy_2GdN@C_{80}$ endofullerenes were produced by arc-discharge synthesis using the corresponding metals. In the sample used for this work, there was about 5% $Dy_3N@C_{80}$

present.

The magnetization measurements were performed by means of X-ray circular magnetic dichroism (XMCD) and SQUID magnetometer. XMCD measurements were performed in X-Treme beamline, SLS [42]. The sample was spray-coated on an aluminum substrate from a toluene solution and later introduced into an ultra-high vacuum (UHV) system for XMCD measurements. The SQUID magnetometer used was Quantum Design MPMS3 Vibrating Sample Magnetometer (VSM) with a ^{3}He cryostat. For the magnetization measurements in MPMS3, the sample was drop-cast from toluene solution into a plastic sample holder resulting in a black powder form. A temperature independent diamagnetic background of -5.8×10^{-8} Am^2/T was inferred from temperature dependent magnetization measurements.

Model and Results

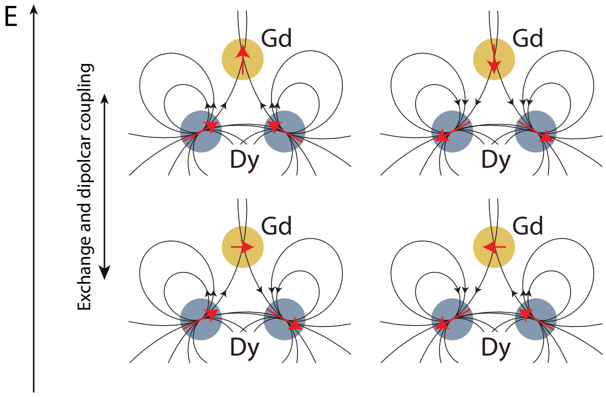

Figure 5.9. The energy levels of $Dy_2GdN@C_{80}$ at an absence of an external magnetic field. At the ground state, the superposition of two ferromagnetically aligned Dy aligned the Gd spin parallel to the Dy–Dy line. In case of antiferromagnetic alignment of the two Dy, the resulting field forces the Gd to point along the Gd–N axis.

.

Figure 5.9 shows the model of the ground state of $Dy_2GdN@C_{80}$ at zero external magnetic field. The endohedral unit, surrounded by C_{80}^{6-} carbon cage, consists of three lanthanide ions—one isotropic Gd^{3+} $^8S_{7/2}$ and two strongly anisotropic Dy^{3+} derived from $^6H_{15/2}$ [23, 24]. The ligand field of the central nitrogen atom N^{3-} lifts the 16-fold degeneracy of the anisotropic Dy^{3+} $^6H_{15/2}$ Hund's ground state [24, 73]. As for $Dy_2ScN@C_{80}$, the ground state assumes $J_z \pm 15/2$ with a large expected magnetic moment $\mu = \pm 10\ \mu_B$. In the ground state, the Gd ion has a theoretical maximum of its magnetic moment of 7 μ_B.

In comparison with $Dy_2ScN@C_{80}$ [24], where only two magnetic ions of the same species were present, here we have a second species (Gd) whose magnetic moment is isotropic and follows the local magnetic field if the exchange between Gd and Dy is neglected. At the Gd site, the two Dy atoms in ferromagnetic configuration create a mean field of 180 mT parallel to the Dy–Dy axis. This implies that Gd should follow the magnetization of the Dy ions in zero field. The antiferromagnetic configuration of the Dy ions, which is an excited state, creates a field of $\approx$ 720 mT at the site of Gd, and this field is perpendicular to the Dy–Dy axis.

Figure 5.10 (a) shows the background subtracted X-ray absorption spectroscopy (XAS) measurements for $Dy_2GdN@C_{80}$ for both Gd and Dy $M_{4,5}$-edges at 6.5 T applied magnetic field with right I^+ and left I^- circularly polarized light. The total electron yield (TEY) from the sample was divided by the gold cross section normalized gold mesh current. The running integral of the total absorption $I_{\text{tot}} = I^+ + I^-$ [Fig. 5.10 (a) middle] was normalized to 1 for better comparison between the spectra of different ions. The resulting X-ray magnetic circular dichroism (XMCD) is shown in the bottom of the graph. For Gd, the running XMCD integral over the two M_4 and M_5 edges equals zero, as Gd^{3+} has a half-filled $4f$ shell with orbital angular momentum equal to zero.

Sum rule analysis [38–40] of the absorption data [Fig. 5.10 (a)] reveals the effective magnetic moments of Gd^{3+} and Dy^{3+} ions in $Dy_2GdN@C_{80}$ at 6.5 T applied magnetic field. From the evaluations (Table 5.1), we obtain $m_z(\text{Gd}) = 5.8 \pm 0.1\ \mu_B$ and $m_z(\text{Dy}) = 4.5 \pm 0.1\ \mu_B$. Although the absolute moment of Dy (10 μ_B) is bigger than the moment of Gd 7 μ_B, the moment of Dy has axial symmetry and can point only towards or away from the central nitrogen. This anisotropy causes the effective moment of Dy to have half of its nominal value of 10 μ_B [23]. In contrast to Dy, the moment of Gd is isotropic and can align itself to the external magnetic field. Thus, the effective moment of half-filled can reach its nominal value of 7 μ_B at saturation.

	$\langle S_z \rangle$	$\langle L_z \rangle$	$\langle J_z \rangle$	$\langle L_z \rangle / \langle S_z \rangle$	μ_z (μ_B)
Dy	1	2.4	3.4	2.4	4.5 ± 0.1
Gd	2.9	-0.05	2.9	-0.02	5.8 ± 0.1

Table 5.1. Expectation values of spin $\langle S_z \rangle$ and orbital $\langle L_z \rangle$ magnetic moments at 6.5 T from the sum rule analysis. $\langle J_z \rangle$ is calculated as $\langle S_z \rangle + \langle L_z \rangle$.

The element specific magnetization curves of endohedral Gd and Dy shown in Fig. 5.10 (b) were constructed from the asymmetry $[(I^+_{E_2} - I^+_{E_1}) - (I^-_{E_2} - I^-_{E_1})]/[(I^+_{E_2} - I^+_{E_1}) +$

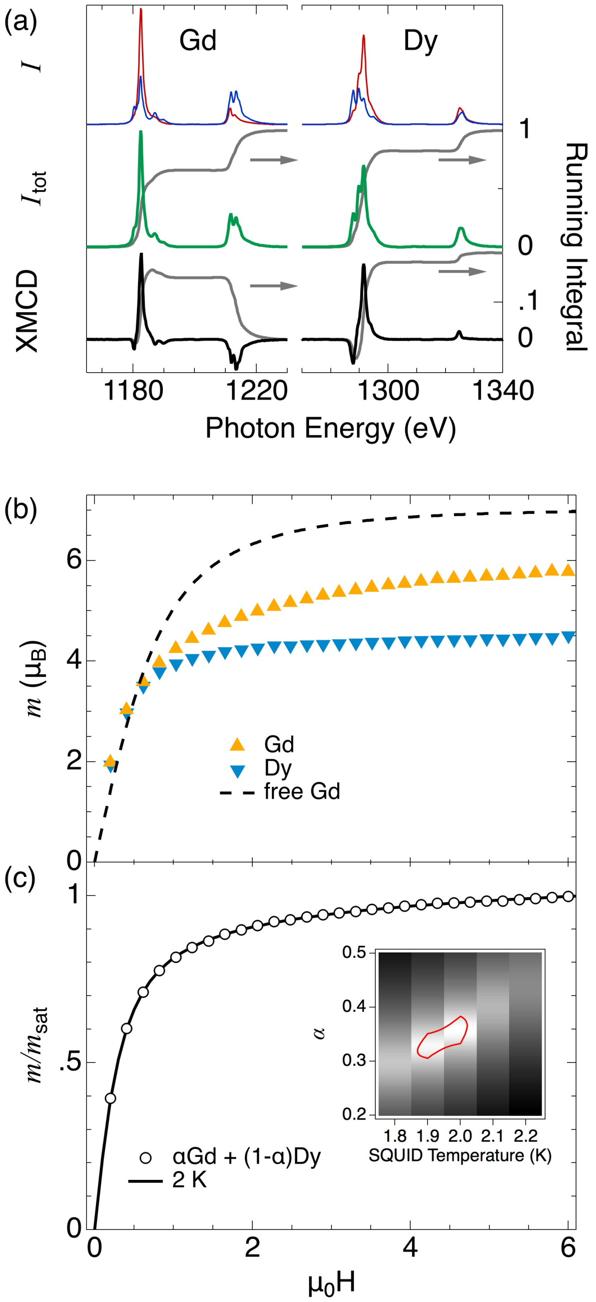

Figure 5.10. (a) Top: Polarization-dependent X-ray absorption spectra (XAS) of $Dy_2GdN@C_{80}$—background subtracted—I^+ (red) and I^- (blue); measured at the Gd and Dy $M_{4,5}$-edges at 6.5 T. Middle: Sum of XAS of both X-ray helicities from the top panel, I_{tot}. Bottom: XMCD spectrum, $I^+ - I^-$.The grey lines are the running integrals for corresponding spectra. (b) Field dependent magnetization m of Dy (down-triangle) and Gd (up-triangle) recorded by XMCD magnetometry. The absolute values are calculated by applying sum rule analysis on the XAS data. Brillouin function corresponding to $g = 2$, $J = 3.5$ and $T = 1.95\ K$, same as Gd. (c) Field dependent magnetization m recorded by SQUID magnetometry at 2 K and the linear combination of XMCD magnetization curves (circles) $\alpha\mathrm{Gd} + (1-\alpha)\mathrm{Dy}$. α is obtained form the χ^2 map of the inset with the lowest χ^2 value at temperature of 2 K. The contour corresponds to the double of the χ^2 minimum.

$(I^-_{E_2} - I^-_{E_1})]$, where E_1 and E_2 are the pre-edge and XMCD-max photon energies. For Gd E_1 and E_2 are 1173 eV and 1182.6 eV respectively, and for Dy they equal 1184.5 eV and 1291.5 eV. The scaling values of the magnetization were taken from the sum rule calculations for the corresponding ions. The magnetization of the endohedral Gd deviates from that of a Brillouin function with $g = 2,\ J = 3.5$ and $T = 1.95\ K$, which corresponds to a non-interacting Gd. This deviation indicates that the endohedral Gd does not behave as a free ion and is subject to intramolecular interactions with the two Dy ions.

The magnetization measured with SQUID shows the sum of both Dy and Gd with contributions from the diamagnetic carbon cage and sample holder:

$$m = m_{\mathrm{Dy}} + m_{\mathrm{Gd}} + m_{\mathrm{dia}}. \tag{5.2}$$

Equation 5.2 also implies that m^{SQUID} and $\mu^{\mathrm{XMCD}}_{\mathrm{Dy,Gd}}$ are measured at the same temperature and fields. If the SQUID and XMCD data are consistent, we may write $m^{\mathrm{SQUID}} = N[\alpha\,\mu^{\mathrm{XMCD}}_{\mathrm{Gd}} + (1-\alpha)\,\mu^{\mathrm{XMCD}}_{\mathrm{Dy}}] + m_{\mathrm{dia}}$, where N is the number of molecules and α is a mixing parameter depending on the endohedral stoichiometry.

From a fit of the temperature dependent m^{SQUID} data to the right side of Eq. 5.2 N, α and T may be determined. The inset of Fig. 5.10 (c) shows the χ^2 map for the mixing parameter α and SQUID magnetization measurements at different temperatures. The χ^2 minimum indicates a temperature of 1.95 ± 0.05 K and $\alpha =$ 0.34 that is within the confidence interval $(1.3 \times \chi^2_{\mathrm{min}})$ of 0.03 consistent with the expectation of 0.32, the nominal stoichiometry of our sample.

The field-dependent magnetization of $Dy_2ScN@C_{80}$ was measured previously but with the lowest temperature of 2 K [24]. Here temperature of 400 mK was obtained using a ^{3}He cryostat. The comparison of the m(H) curve of $Dy_2ScN@C_{80}$ at 400 mK with 2 K data shows only a slight increase in the coercive field (≈ 1 T). However, the shape of the magnetization curve exhibits a bigger change. The 400 mK curve is ”boxier” indicating an increased magnetization lifetime. After saturating the magnetization at 7 T, the moment stays fairly stable until ≈ -0.8 T where is a sharp decrease is seen.

$Dy_2GdN@C_{80}$, in contrast, shows no significant opening of the hysteresis above 2 K. Only the decrease in temperature below 2 K shows visible hysteresis, albeit, the coercive field is much smaller than that of $Dy_2ScN@C_{80}$. As the added second

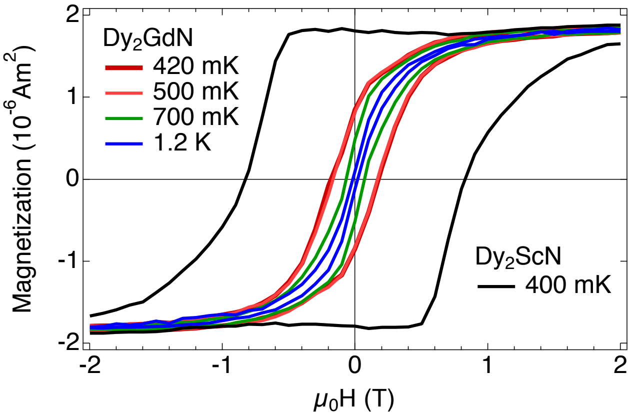

Figure 5.11. Field dependent magnetization m of $Dy_2GdN@C_{80}$ and $Dy_2ScN@C_{80}$. The measurements were performed at 420 mK, 500 mK, 720 mK and 1.2 K for $Dy_2GdN@C_{80}$ and at 400 mK for $Dy_2ScN@C_{80}$ with the field scan rate of 3.8 mT/s. $Dy_2ScN@C_{80}$ shows significantly bigger coercive field in comparison.

species of ions, Gd has an isotropic magnetic moment it could pick up the external perturbations better than the strongly anisotropic Dy.

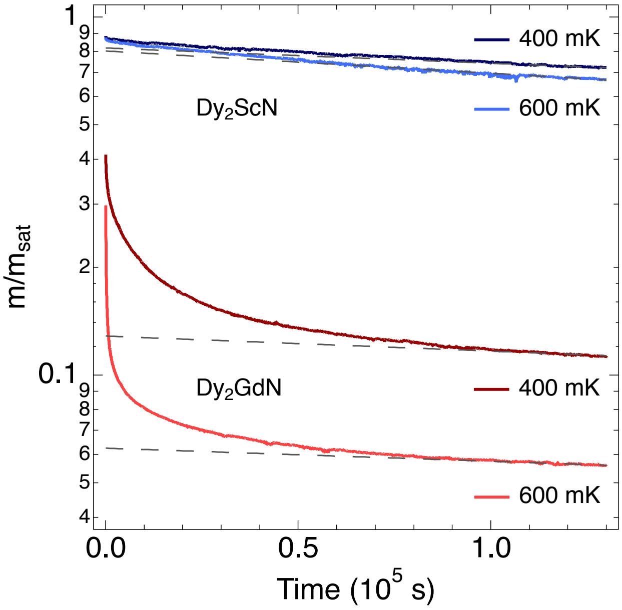

Figure 5.12. Time dependent magnetization of $Dy_2ScN@C_{80}$ and $Dy_2GdN@C_{80}$ measured at 400 mK and 600 mK. The magnetization is normalized by the saturation value. The dashed lines indicate the exponential relaxation ($m_0\, e^{-t/\tau}$) after the initial fast decay. The fit parameters are shown in Table 5.2.

.

The decay of magnetization for both $Dy_2ScN@C_{80}$ and $Dy_2GdN@C_{80}$ at near zero external magnetic field (< 0.5 mT) is shown on a semi-logarithmic scale in Fig. 5.12 at subkelvin temperature using the ^{3}He cryostat. The measurements of magnetization started right after the magnetic field was decreased from 7 T to zero in 350 s. The duration of the measurements was limited by the lifetime of the one-shot ^{3}He system. Figure 5.7 shows additional time dependent magnetization measurements with the longest possible measurement times.

The magnetization of $Dy_2ScN@C_{80}$ displays on a semi-logarithmic graph a linear time dependence one day after ramping the magnet to zero field. This linear behavior means exponential time dependence of magnetization on time fitted by a single exponential function (dashed line in Fig. 5.12). The initial fast decay could be attributed to the inter-molecular interaction between neighboring molecules.

$Dy_2GdN@C_{80}$ also shows a linear decay after one day past the zeroing of the magnetic field with a similar slope (Table 5.2), the time constant τ, as $Dy_2ScN@C_{80}$ for the corresponding temperature. However, the initial decay of magnetization is much faster and bigger than that of $Dy_2ScN@C_{80}$. At 400 mK ≈ 87% of the moments decayed in the first day of the trip to thermal equilibrium.

	Dy_2ScN		Dy_2GdN	
	$m(t=0)/m_{\text{sat}}$	τ (10^6 s)	$m(t=0)/m_{\text{sat}}$	τ (10^6 s)
400 mK	0.82	1.02	0.129	1.04
600 mK	0.804	0.7	0.062	1.19

Table 5.2. Fit (dashed line in Fig. 5.12) values of the function $m(t) = m_0\, e^{-t/\tau}$ for $t > 9 \times 10^4$ s to the data in Fig. 5.12.

6. $Tb_2ScN@C_{80}$

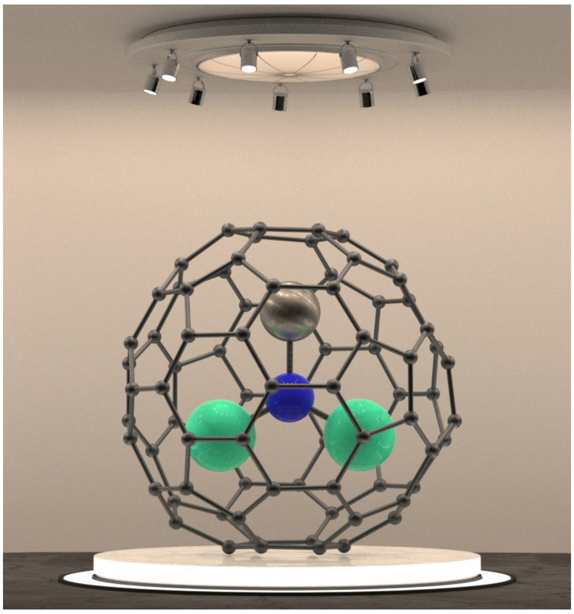

Figure 6.1. The ball-and-stick model of $Tb_2ScN@C_{80}$. The endohedral unit with two triple ionized Tb^{3+} and a Sc^{3+} ions at the corners of a triangle with a nitrogen in the middle inside a C_{80}^{-6} fullerene. Image courtesy: Rasmus Westerström.

6.1. Introduction

In previous chapters we looked into the influence of the diamagnetic component in the single paramagnetic ion endohedral unit at the example of $HoLu_2N@C_{80}$ and $HoSc_2N@C_{80}$ (Chapter 4), also we have studied the influence of two different paramagnetic species on each other in $Dy_2GdN@C_{80}$ and compared it with $Dy_2ScN@C_{80}$. Here we study the effect of the change of the paramagnetic ion to Tb in a double paramagnetic ion system $Tb_2ScN@C_{80}$.

$Tb_2ScN@C_{80}$ is another member of the nitride-cluster fullerenes (NCFs) with its model shown in Fig. 6.1 [19–21]. The synthesis of the molecules was presented earlier [74]. The endohedral unit consisting of two triple ionized Tb^{3+} and Sc^{3+} ions

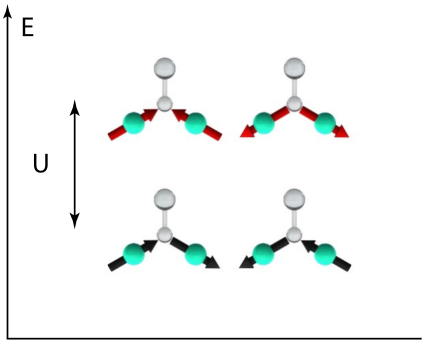

Figure 6.2. The ground state energy levels for $Tb_2ScN@C_{80}$ at zero external magnetic field. The energy U is the sum of dipolar and exchange interactions.

with central nitrogen is encapsulated in a C_{80}^{-6} cage carrying a nominal charge of -6. Previous studies of $Tb_3N@C_{80}$ and $Ho_3N@C_{80}$ indicate a strong ligand field on the individual, ferromagnetically coupled R moments within the (R_3N) cluster with H/T [21].

The ligand field of the central negative nitrogen lifts the Hund's ground state $^7F_6$ degeneracy of Tb. In this ligand field, the maximum $J_z = \pm 6$ forms the ground state. This leads the magnetic moment of terbium to point along the Tb-N axis as for the other ions studied above. In this scenario, the magnetic moment is referred to as pseudospin and is discussed in more details in Chapter 3. Thus, the nominal magnetic moment of Tb in $Tb_2ScN@C_{80}$ is equal to $\mu = 9\ \mu_B$, $2 \times \langle S_z \rangle + \langle L_z \rangle$ where $\langle S_z \rangle = 3$ and $\langle L_z \rangle = 3$.

The two Tb ions in the endohedral unit interact via dipolar and exchange interactions. Following the picture of $Dy_2ScN@C_{80}$ the ground state of $Tb_2ScN@C_{80}$ in zero external magnetic field is shown in Fig. 6.2 [24]. Dipolar interaction favors a ferromagnetic ground state, and if the exchange is also ferromagnetic, then the ground state takes that configuration of the Tb moments. This leads the antiferromagnetic state to be U higher in energy.

The magnetic properties of $Tb_2ScN@C_{80}$ studied by means of X-ray absorption spectroscopy (XAS), X-ray magnetic circular dichroism (XMCD) and SQUID magnetometry are shown in this chapter. The absorption spectroscopy allows the determination of the charge state of the ions. X-ray circular magnetic dichroism (XMCD) allows the study of the average magnetization of the sample and by means of sum rule analysis the expectation value of spin and orbital magnetic moments.

The XMCD magnetization was compared with field dependent magnetization measurements performed in the SQUID. Furthermore, the fits to the SQUID magnetization data reveal the average magnetic moment of the Tb ion which in turn was compared with sum rule analysis. From the fits of field dependent magnetization U can also be determined. The sample was drop-cast in plastic sample holder provided by quantum design. The details of sample preparation both for XMCD and SQUID measurements are discussed in Appendix B.

6.2. X-ray Absorption Spectroscopy and Sum Rules

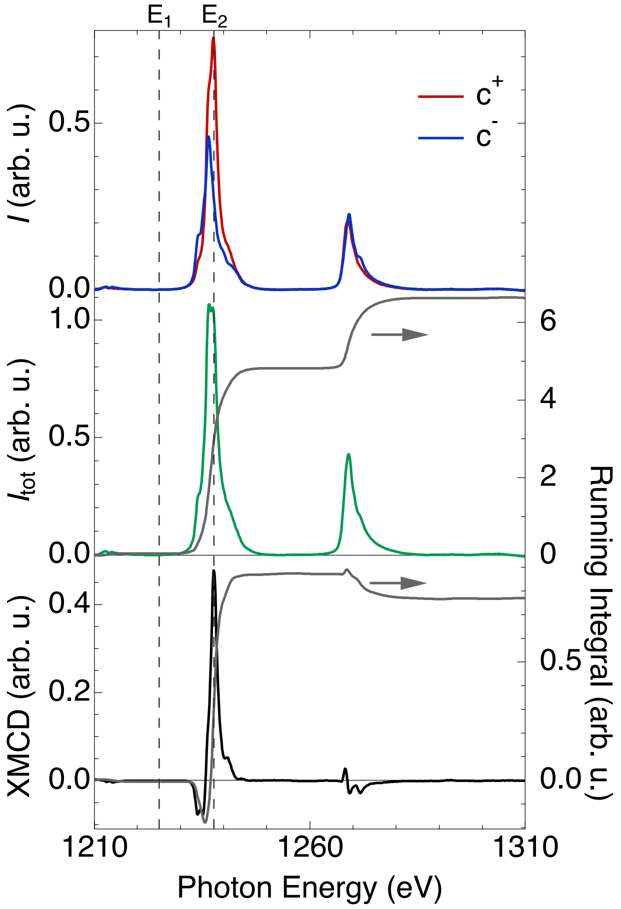

Figure 6.3. Top: Light polarization-dependent X-ray absorption spectra (XAS) of $Tb_2ScN@C_{80}$, background subtracted, I^+ (red) and I^- (blue); measured at the Tb $M_{4,5}$ edge $\mu_0 H = 6.5$ T, $T \approx 2-3$ K. Middle: total XAS I_{tot}: sum of I^+ and I^- from the top panel. Bottom: XMCD spectrum, $I^+ - I^-$. The gray lines are the running integrals for corresponding spectra. $E_1 = 1225$ eV and $E_2 = 1237.7$ eV are the energies used for measuring XMCD magnetization.

Figure 6.3 shows the background subtracted X-ray absorption spectroscopy measurements for $Tb_2ScN@C_{80}$ in the energy range of the $M_{4,5}$-edges of Tb with circularly right and left (I^+ and I^-) polarized light. The spectra were recorded at 6.5 T applied magnetic field and $\approx 2-3$ K in X-Treme beamline, SLS [42]. The temperature is inferred from the comparison of XMCD magnetization data with the SQUID measurements for $Dy_2GdN@C_{80}$ and from a Brillouin fit to the field dependent XMCD magnetization of $GdCl_3$ discussed in Sec. 5.

The total electron yield (TEY) was normalized by the gold-mesh current and the cross-section of gold for the corresponding photon energies. The background subtraction was performed by fitting a polynomial to the absorption spectra using a mask to exclude the peak areas from fitting. More detailed discussion about the XAS is present in Sec. 2.3. The total absorption was constructed by adding the background subtracted spectra for both helicities $I_{\text{tot}} = I^+ + I^-$. XMCD spectrum is the subtraction of I^- from I^+.

Sum rule analysis was performed on the integrals of I_{tot} and XMCD over the $\mathrm{M}_(4,5)$ edges [38–40]. As the 4f electrons of are well isolated, the ratio $\langle S_z \rangle / \langle L_z \rangle$ and $\langle T_z \rangle / \langle S_z \rangle$ is assumed to be the same for Tb^{3+} in different chemical environments where $\langle T_z \rangle$ is the magnetic dipole operator. Thus, the analytically obtained ratio of $\langle T_z \rangle / \langle S_z \rangle$ from [40] was used in [38] for sum rule calculations. The average expectation values are: $\langle S_z \rangle = 1.26$, $\langle L_z \rangle = 2.84$, this leads to $\langle J_z \rangle = 2.67$ and $\mu = 4.01\ \mu_B$. The corresponding expectation values from Hund's rules are: $\langle S_z \rangle = 3$, $\langle L_z \rangle = 3$, $J_z = 6$ and $\mu = 9\ \mu_B$. From an isotropically distributed system of two interacting pseudospins that did not yet reach saturation, the magnetic moment is expected to be slightly smaller than half of the nominal magnetic moment of $\mu = 4.5\ \mu_B$ (Chapter 3). The sum rule analysis shows 10% less moment for Tb which could be attributed to not reaching the saturation magnetization yet and systematic errors in the evaluation of the data.

6.3. Field Dependent Magnetization

Figure 6.4 shows field dependent magnetization of $Tb_2ScN@C_{80}$ recorded by the SQUID magnetometer [Sec. 2.2.1] at 1.55 K, 1.8 K, 2.3 K, 3 K, 4 K, 5 K, 6 K, 8 K and 10 K and the element-specific XMCD magnetization curve $T \approx 2 - 3$ K. The background subtraction of the SQUID magnetization curves is discussed in the next section.

The XMCD magnetization curves were constructed from the difference $(I^+_{E_2} - I^+_{E_1}) - (I^-_{E_2} - I^-_{E_1})$, where $E_1 = 1225$ eV and $E_2 = 1237.7$ eV are pre-edge and maximum of XMCD photon energies shown in Fig. 6.3. The absolute values for XMCD magnetization were taken from the sum rule calculations presented in the previous

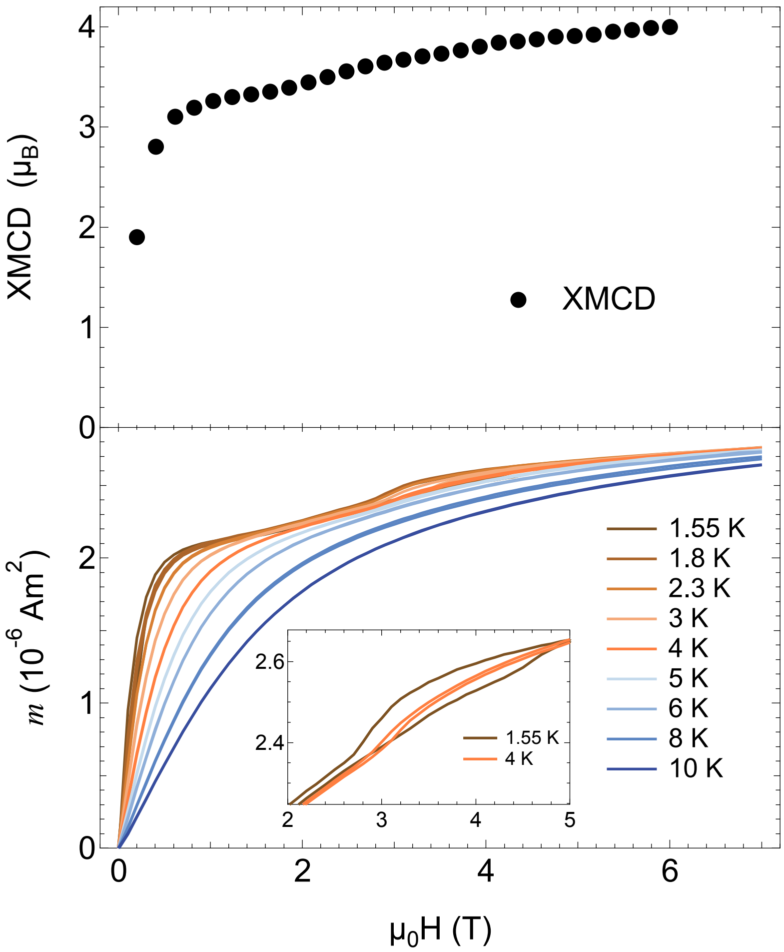

Figure 6.4. Field dependent magnetization of $Tb_2ScN@C_{80}$ measured with XMCD (top) and SQUID magnetometer with a scan rate of 5.1 mT/s (bottom). The background from the SQUID data was inferred from temperature dependent measurements. Inset: A hysteresis between 3 to 5 T.

section. XMCD magnetization data was averaged from three different magnetization curves which went from 6 T to -6 T and back to 6 T. As there was no hysteresis in the XMCD data, the four quarters of the magnetization data was further averaged to one quarter from 0–6 T.

The SQUID magnetization of $Tb_2ScN@C_{80}$ does not show a hysteresis above 1.55 K with the field scan rate of 5.1 mT/s. However, it exhibits an opening in an unusual place, between 3 to 5 T (Fig. 6.4). The opening is still visible at 4 K. Lowering the temperature below 1 K (Fig. 6.5) by means of ^{3}He cryostat opens up a butterfly-like hysteresis similar to $DySc_2N@C_{80}$ [23] and a small remanence at zero field. The corresponding time-dependent subkelvin magnetization studies are shown in the following sections.

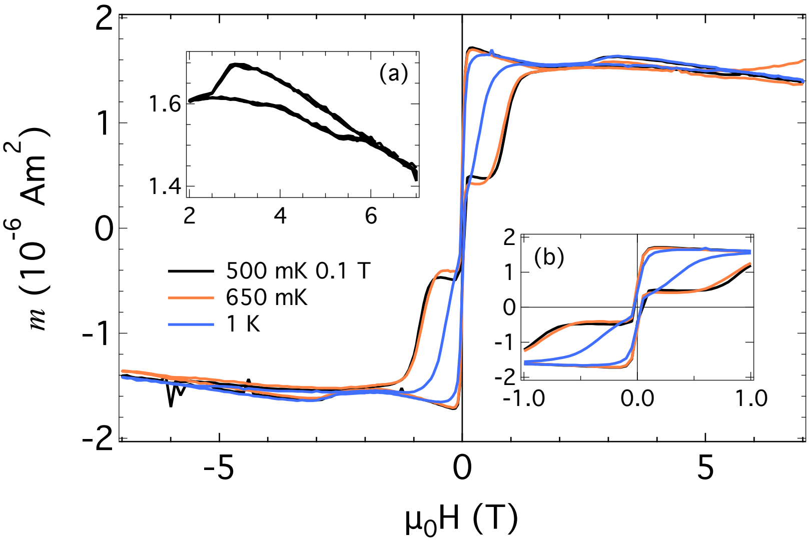

Figure 6.5. Opening of hysteresis (magnified in inset (b)) in the magnetization curve of $Tb_2ScN@C_{80}$ at sub-kelvin temperature measured with He3 insert. Inset (a) shows the magnified hysteresis between 3–5 T. The structure is more defined that in Fig. 6.4

.

The dolphin shaped hysteresis between 3–5 T shows sharper transitions at its ends 3 and 5 T, respectively, as the temperature is lowered below 1 K as shown in Fig. 6.5 inset (a). The opening becomes more prominent.

6.4. Field induced reorientation

The possibility of a conformational change induced by external magnetic field, reorienting the endohedral unit inside the cage, was already shown in Sec. 4.7 and [59]. Also, the detailed theoretical model was presented in Sec. 3. Figures 6.6 and 6.7 are measured by following to a similar procedure as in [59].

Figure 6.6 shows the background subtracted magnetization curve of $Tb_2ScN@C_{80}$ for zero-field (black) and in-field (red) cooled sample measured at $T = 1.8$ K. The sample is cooled to $T = 1.8$ K in zero field ($< 0.5\ mT$) from room temperature for the zero-field measurements. The magnetic field was oscillated to zero, prior cooling, to achieve the smallest possible remnant magnetic field inside the sample space.

After measuring the field dependent magnetization of the zero-field cooled sample, a magnetic field of 7 T was applied, and the temperature dependent magnetization of the zero-field cooled sample m_z was measured from 1.8 K to 300 K (Fig. 6.7 black). At 300 K, the field was kept at 7 T and the magnetization was measured while cooling

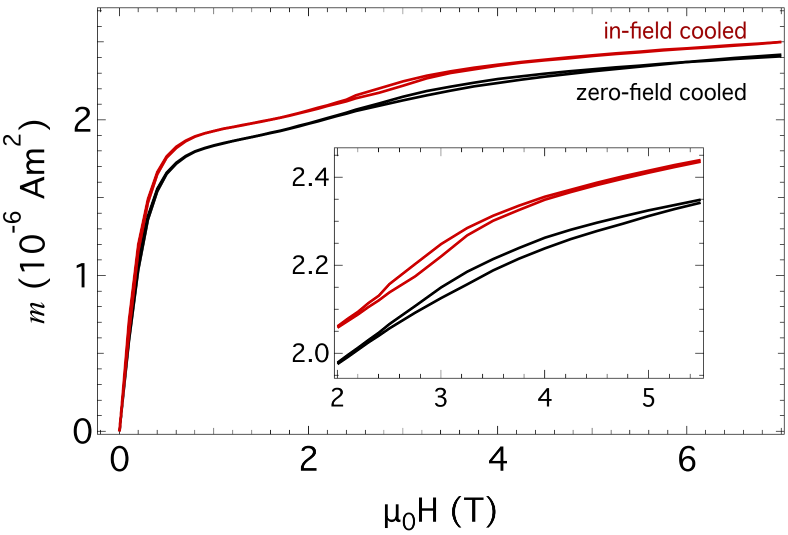

Figure 6.6. Field dependent magnetization m of zero-field (black) and in-field 7 T (red) cooled $Tb_2ScN@C_{80}$. Inset: The shrinking of the hysteresis between 3 − 5 T after in-field cooling.

form 300 K to 1.8 K. After reaching 1.8 K, the field-dependent magnetization of the in-field cooled sample was measured (Fig. 6.6 red). It is followed by the second run of temperature dependent magnetization measurements of the in-field cooled sample, now during warmup from 1.8 K to 300 K. Measurements of in-field magnetization m_i both while cooling and warming overlap.

As seen from Fig. 6.6, in field cooling increases the saturation magnetization by 3.7% at 1.8 K for $Tb_2ScN@C_{80}$ whereas for $HoLu_2N@C_{80}$ the increase is 4.7% and for $TbSc_2N@C_{80}$ it is 4% as seen in Fig. 4 in Sec. 4.7 [59]. The temperature sweep rate during the measurements was 5×10^{-2} Ks^{-1}.

Besides the increase in saturation magnetization, there is another effect occurring in $Tb_2ScN@C_{80}$. Figure 6.6 shows a change of the shape of the hysteresis between 2.5 T and 5 T. The hysteresis closes at a smaller field for the in-field cooled sample. This leads to a decrease of the area enclosed by the hysteresis of the zero-field cooled by a factor of 2.3 compared to in-field cooled sample. This could be caused by the alignment of Tb moment due to in-field cooling which leads to the depopulation of the "non-active" Tb_2 which are at $\theta = 90°$ relative the external magnetic field.

The freezing temperature T_F is the lowest temperature where hop-rotation of the endohedral unit between the neighboring lowest energy states is possible within the measurement timescale. The T_F can be extracted from the ratio m_i/m_z of temperature dependent magnetization of in-field m_i and zero-field m_z cooled samples

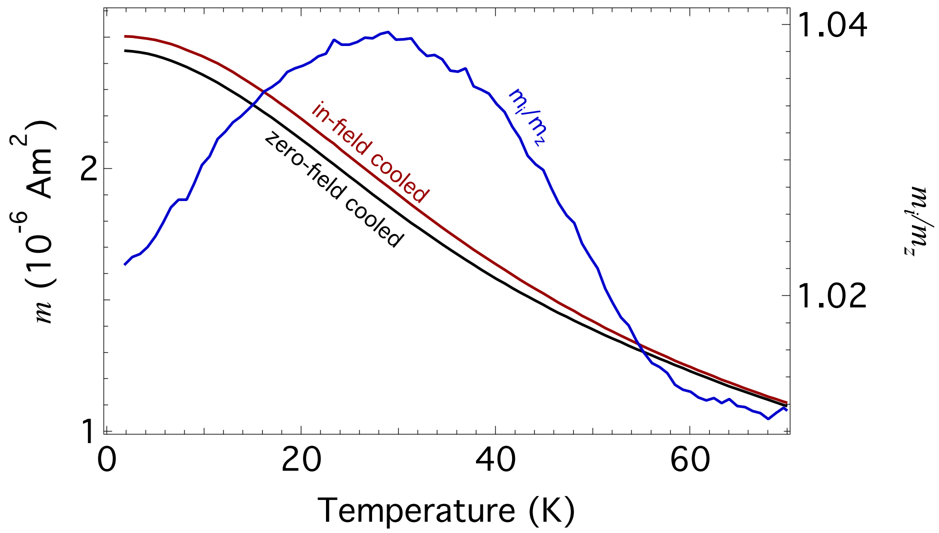

Figure 6.7. Temperature dependence of the magnetic moment m of $Tb_2ScN@C_{80}$ after zero-field m_z (black) and in-field m_i (red) cooling. The ratio of m_i/m_z (blue) increases below the freezing temperature T_F.

shown in Fig. 6.7. For $Tb_2ScN@C_{80}$ with a temperature sweep rate $\beta = 5 \times 10^2$ Ks^{-1} the $T_F \approx 60$ K. Above the T_F the ratio $m_i/m_z \approx 1$ indicating a free hoop-rotation of the endohedral unit. Whereas, below T_F the field orientation is visible in a m_i/m_z ratio greater than one.

The ratio m_i/m_z for $Tb_2ScN@C_{80}$ in Fig. 6.7 is phenomenologically similar to $HoLu_2N@C_{80}$ and $TbSc_2N@C_{80}$ [Fig. 4 in Sec. 4.7] though, with some differences. Although the $T_F \approx 60$ K, the magnitude of the effect depends on atoms of the endohedral unit. More detailed studies of the effect of in-field cooling depending on β, field strength and paramagnetic ion of the endohedral unit is presented in the paper [59] with its corresponding Chapter 4. The theoretical model is outlined in Chapter 3.

6.5. Background Estimation

The determination of the diamagnetic background is crucial for modeling of the paramagnetic properties of a system. In contrast to XMCD magnetization measurements, the magnetization measured in SQUID magnetometers carries, as well as the magnetic information of the background, the diamagnetism of the sample and sample holder. The smallest value for background was estimated from magnetization × temperature *versus* temperature graphs $m \times T$ *versus* T. Referring to Curies law,

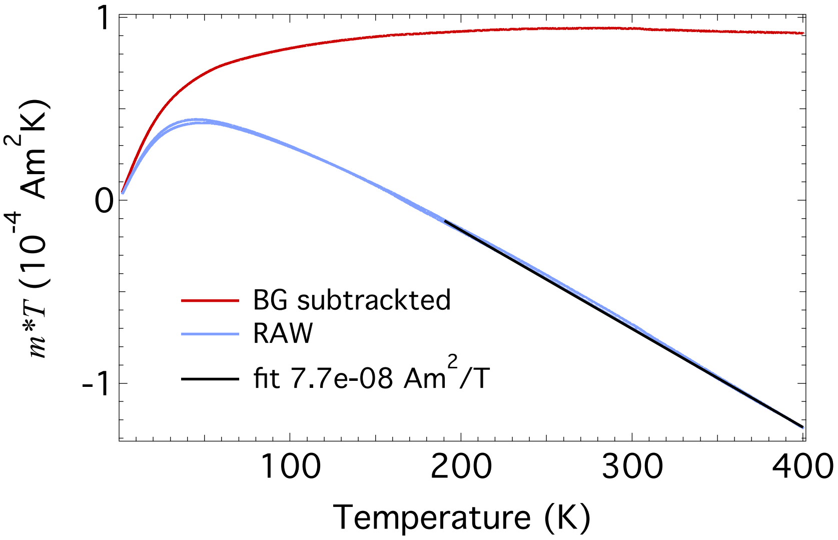

Figure 6.8. Magnetization $m\times$temperature T vs T for the RAW and background subtracted data. Background was inferred from the slope of the linear fit performed on the temperature range of $\approx$ 200 K to 400 K.

$m = \frac{A}{T} - D$ follows $mT = A - DT$, where m is the measured magnetic moment, A the Curie constant, D the diamagnetic component and T is the temperature.

The Curie constant A describes the paramagnetic component and is always positive, even if A should change with temperature due to the population of the magnetic states that are split due to ligand field.

6.6. Time dependent measurements: AC susceptibility and magnetization relaxation

To access the lifetime of magnetization, time-dependent measurements were carried out. As above 1.8 K $Tb_2ScN@C_{80}$ shows no hysteresis, the magnetization lifetime was measured by AC susceptibility measurements [Sec. 2.2.2].

Figure 6.9 shows the real (in-phase) χ' and imaginary (out-of-phase) χ'' part of AC susceptibility for $Tb_2ScN@C_{80}$ measured with the MPMS3 [Sec. 2.2.1]. The measurements were performed in the temperature range between 1.8 K and 30 K at zero (< 0.5 mT) DC magnetic field with a driving AC field amplitude of 1 mT up the frequencies of 10 Hz and 0.25 mT afterward. Typically, larger driving amplitudes result in smaller measurement error, but due to the limitations of the machine it is

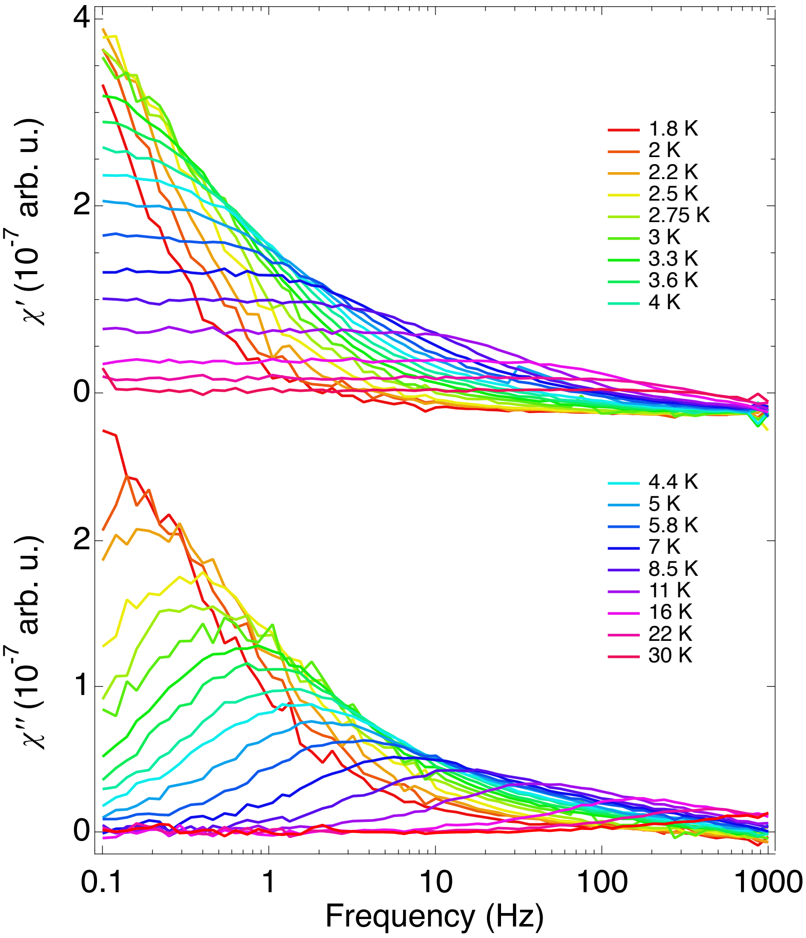

Figure 6.9. AC: Real (in-phase) χ' and imaginary χ'' (out-of-phase) component of AC susceptibility for $Tb_2ScN@C_{80}$ measured at near zero (< 0.5 mT) DC magnetic field.

not possible to use 1 mT driving AC field throughout the whole range of frequencies and the switching point should be chosen away from the peak in χ''.

The χ' and χ'' were simultaneously fitted with equations 2.5 and 2.6. From the fits, the magnetization relaxation time τ was obtained. The best fit results for τ are shown in the next section.

Figure 6.10 shows the time dependent magnetization of $Tb_2ScN@C_{80}$ measured with DC magnetometer below 1.5 K. The decrease in temperature increased the relaxation time allowing it to be measured with DC magnetometry. The magnetic field was saturated to 7 T and then decreased to 3 mT in 350 s. The end field of 3 mT was chosen to get closest to zero field in the sample space due to the properties of the machine. The increase in the magnetic moment seen after reaching the smallest value is due to the behavior of the superconducting magnet. The magnetic field slowly increases with time after the field was ramped down from 7 T to zero. Further

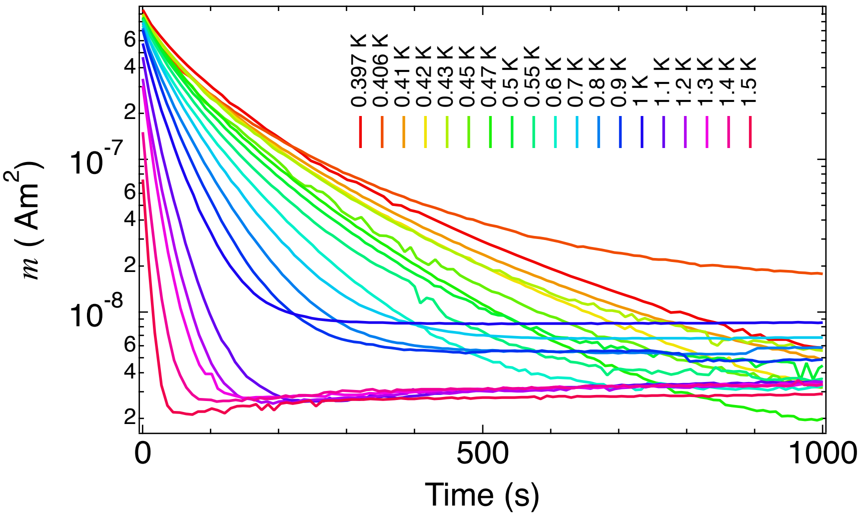

Figure 6.10. DC: Magnetization m relaxation curves for $Tb_2ScN@C_{80}$ measured after stabilization of field—from 7 T to 3 mT. The slow increase of m for higher temperatures is due to the increase of magnetic field from the superconducting magnet.

discussion about the superconducting magnet used in the MPMS3 is presented in Appendix D.

Below $T = 1.5$ K the lifetime of the magnetization was extracted from time-dependent relaxation the of magnetization (Fig. 6.10) by fitting a double exponential function. The best-fit parameters are shown and discussed in the next section.

It was already discussed in Sec. 4 that the application of a constant magnetic field increases the magnetization lifetime for $HoLu_2N@C_{80}$. Here, in Fig. 6.11 we show field dependent magnetization relaxation for $Tb_2ScN@C_{80}$. In Fig. 6.11 left the magnetic field was decreased from 7 T to the corresponding field value. Whereas, in the right panel the field was increased from 0 T. The field sweep rate was 20 mT/s.

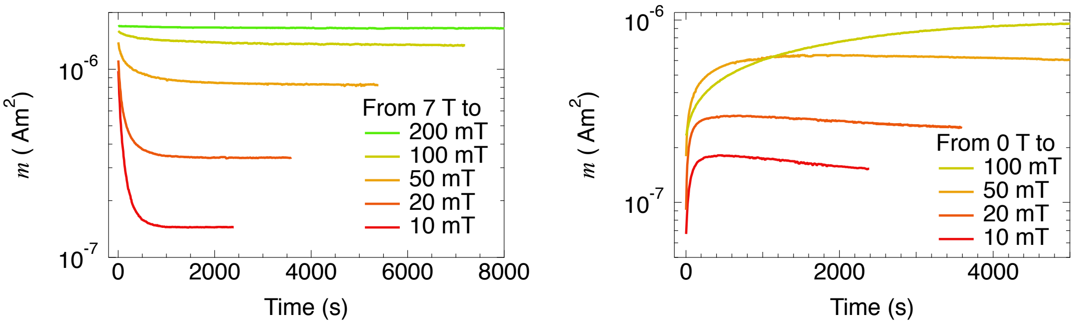

Figure 6.11. Field dependent magnetization relaxation of $Tb_2ScN@C_{80}$. The measurement started when the field stabilized after it was decreased (left) or increased (right) from 7 T (left) or 0 T (right) to the corresponding value.

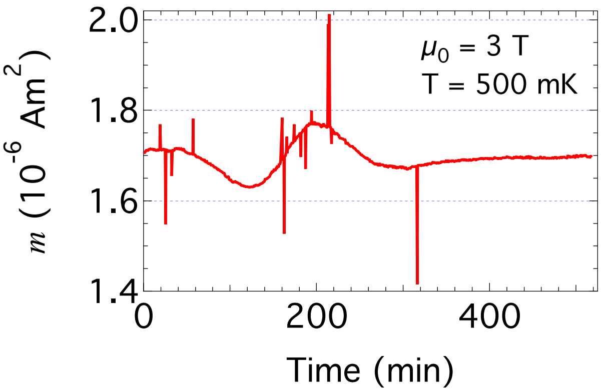

Figure 6.12. Oscillation of magnetization after the magnetic field is decreased from 7 T to 3 T.

The decrease in moment m in Fig. 6.11 after reaching saturation at given field is connected with the behavior of the superconducting magnet further discussed in Appendix D.

As expected, the magnetization relaxation time τ increases with increasing magnetic field (Fig. 6.11 and 6.14). The time-dependent magnetization data is fitted with a double exponential to extract the characteristic lifetime shown in the next section. From Fig. 6.11 left it is visible that already in a field of 200 mT the relaxation time of the moment is significantly larger compared to smaller fields.

An interesting oscillation of magnetization was noticed when the magnetic field was decreased after saturation at 7 T to 3 T, the region of high field hysteresis, as shown in Fig. 6.12. The magnetization stays constant for 20 min and then it is followed by one cycle of oscillation about the equilibrium position with an amplitude of 7×10^{-8} Am^2 $= 7.5 \times 10^{15}$ μ_B. The exact reasons for this phenomena are not known yet.

6.7. Lifetime of Magnetization

The extracted magnetization relaxation times τ for $Tb_2ScN@C_{80}$ and $TbSc_2N@C_{80}$ [67] is shown in Fig. 6.13. The figure demonstrates complex kinetics for $Tb_2ScN@C_{80}$ molecules with two interacting moments. The temperature dependence of τ shows a combination of three linear parts for different temperature ranges. As discussed earlier in Sec. 2.4, a linear temperature trend in the Arrhenius plot corresponds to an Orbach process. Orbach process corresponds to magnetic moments which have to

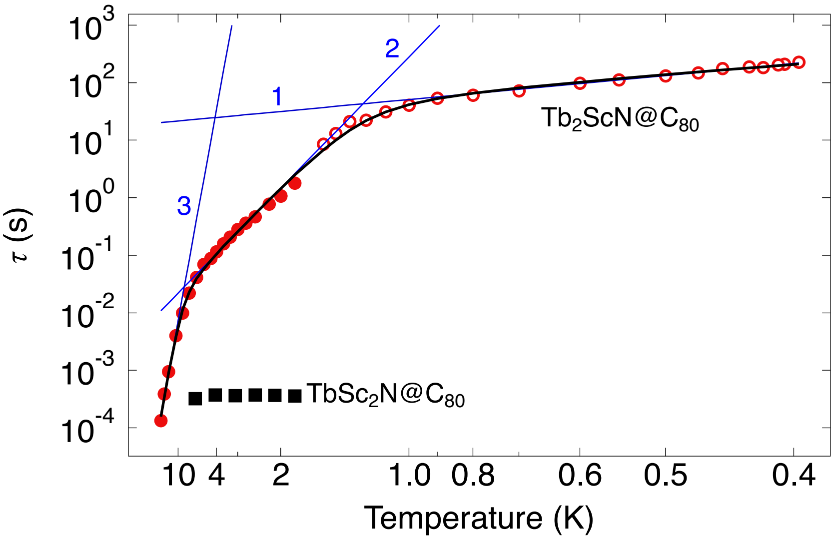

Figure 6.13. Temperature dependent relaxation times τ of $Tb_2ScN@C_{80}$ (red) and $TbSc_2N@C_{80}$ (black) [67] extracted from AC susceptibility measurements (full symbols) [Fig. 6.9] and the larger τ of the double exponential fit of relaxation curves (open symbols) [Fig. 6.10]. The data of $Tb_2ScN@C_{80}$ was fitted with three Orbach processes [Eq. 6.1]—the blue lines 1, 2, 3 show the behavior for the individual processes. Each one of the three Orbach processes is dominant at a certain temperature range.

traverse over an energy barrier which is mediated by phonons. This process requires energy, thus it is temperature dependent.

The temperature dependent relaxation times τ's were fitted with three Orbach processes (Eq. 6.1)

$$\tau^{-1} = \sum_{i=1}^{3} \tau_{0,i}^{-1}\, e^{-\Delta_{\mathrm{eff},i}/kT}, \tag{6.1}$$

where τ_0 is the prefactor and Δ_{eff} is the effective energy barrier.

The best fit parameters of Eq. 6.1 are shown in the Table 6.1.

No	τ_0 (s)	$\Delta_{\mathrm{eff}}/k_B$ (K)
1	19.711 ± 3.05	1 ± 0.1
2	$(7.7 \pm 0.1) \times 10^{-3}$	10.5 ± 0.3
3	$(2.6 \pm 0.5) \times 10^{-5}$	56.4 ± 3

Table 6.1. The best fit parameters of triple Orbach process (Eq. 6.1) for the magnetization relaxation times τ shown on Fig. 6.13. The indices corresponds to the numbers of individual Orbach processes in the Fig. 6.13.

The fit indicates three relaxations processes with different energy barriers which dominate at different temperatures. The blue curves demonstrate the behavior of individual processes in the absence of other relaxations.

Below ≈ 1.1 K the process №1 is dominating as seen from the Fig. 6.13 with correspondingly numbered blue curve. The possible cause of this process is the dipolar interaction of spin between neighboring molecules. The dipolar interaction energy is proportional to the density of magnetic moments [75]. Following the calculation in the paper, the dipolar interaction energy is estimated to 1.2 K which is in good consistency with our results.

Above ≈ 1.1 K process №2 starts to dominate over №1 due to a larger barrier. The energy barrier of the second Orbach (Fig. 6.13 №2) could be the interaction of the two Tb ions inside the cage. The interaction is likely the exchange between the Tb's as previously seen for the Dy ions inside $Dy_2ScN@C_{80}$ [24] where the interaction energy was 0.73 meV (8.47 K). However, due to a different prefactors of $Dy_2ScN@C_{80}$ there is a dramatic difference in the relaxation times: $Dy_2ScN@C_{80}$ at 2 K: 2×10^3 s [24], 0.5 K: 7.7×10^5 s (Sec. 5), and for $Tb_2ScN@C_{80}$ at 2 K: 1 s, 0.5 K: 131 s.

The explanation of the third process №3 is slightly more complicated. There can be several reasons for it. Similar to $Dy_2ScN@C_{80}$ that shows a second energy barrier of similar height 4.3 meV (50 K) which was thought to correspond to the higher excited states [24]. The vibrational states of the fullerene cage also have similar energy range.

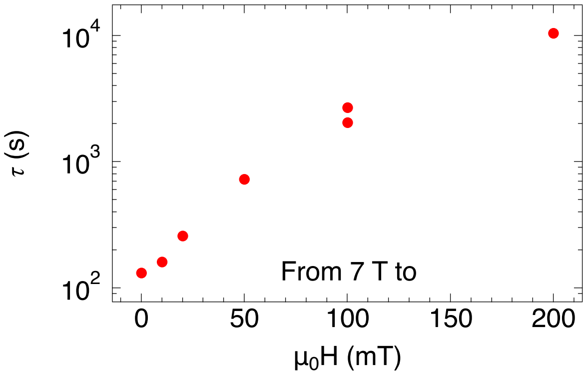

Figure 6.14. Field dependent magnetization relaxation times 7 T to field.

In Chapter 4 the influence of DC magnetic field of 200 mT on the relaxation time τ for a single paramagnetic ion in $HoLu_2N@C_{80}$ was studied. Here, in Fig. 6.14 the field dependence of τ for $Tb_2ScN@C_{80}$ is shown. As expected, the magnetization lifetime increase with increasing magnetic field.

A. Sample Holder

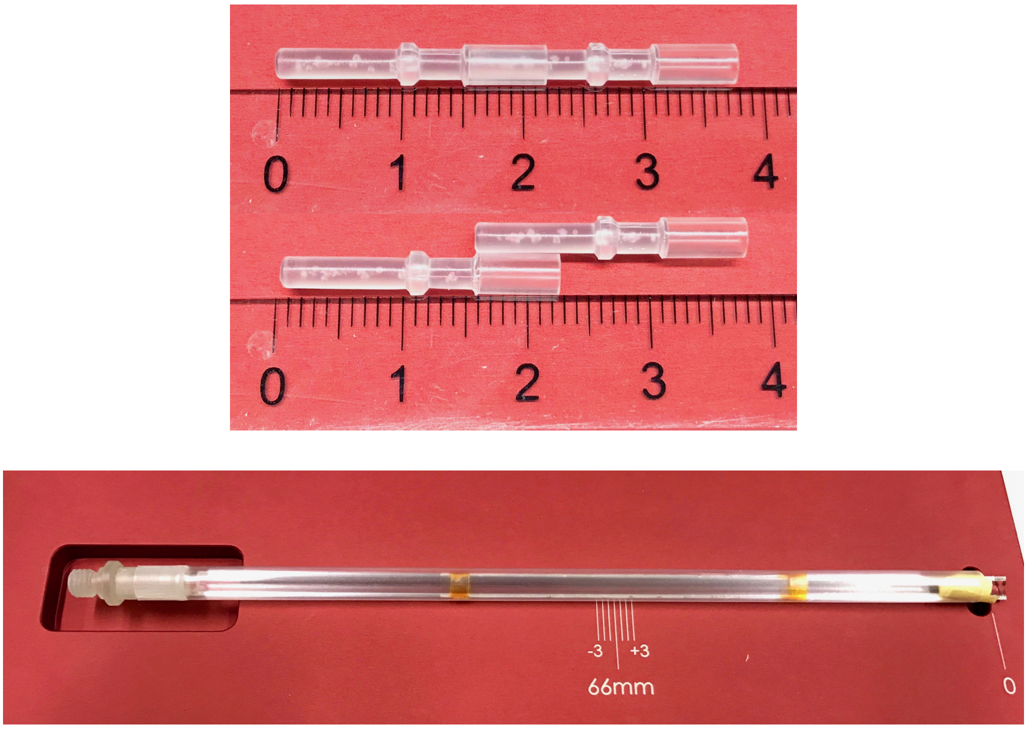

Figure A.1. Top: The plastic powder sample holder provided by Quantum Design. The sample is deposited in the capsule and covered with the foot of the other one (Appendix B).Bottom: Quartz paddle (from QD) with on top 47 mm long suprasil quartz sample holder fixed with thin kapton tape. The suprasil sample holder can also be secured on the quartz paddle with GE varnish. Everything is in a plastic drinking straw to contain any loose object.

In order to perform accurate magnetization measurements of the sample, the effects of the background should be taken into account. There can be many different sources of signals other than the sample [76]. One of them being the sample holder used. For the measurements of the magnetization for this thesis, the plastic powder sample holder provided by Quantum Design was used shown in Fig. A.1. The preparation of the sample is discussed later in the Appendix B.

As discussed earlier in the Sec. 2.2.1 the SQUID detection coils do not detect homogeneous or linear signal. As seen from the Fig. A.1 the used sample holder is

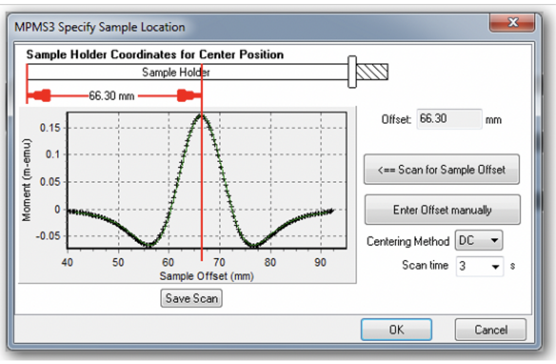

MPMS3 Specify Sample Location

Sample Holder Coordinates for Center Position

Offset: 66.30 mm

Centering Method: DC

Scan time: 3 s

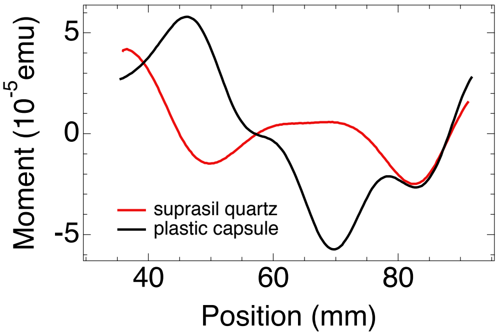

Figure A.2. Left: The centering scan of a paramagnetic point-size (< 5 mm) sample. The measured magnetic moment by the detection coils when the sample moves through the entire length of the sample transport's vertical travel path. Right: The centering scan of a 47 mm long suprasil quartz sample holder ($\mu_0 H = 0.3$ T) and the plastic sample holder ($\mu_0 H = 0.2$ T, the signal is multiplied by a factor of 1.5) at 1.8 K.

neither particularly homogeneous nor long enough. This is visible in the irregular form of the centering scans (Fig. A.2) and relatively high magnetization (Fig. A.5) of the empty sample holder.

Therefore, a new sample holder with a smaller and more homogeneous background signal is desirable for sensitive magnetization measurements. The length of the new sample holder was designed taking into account the following criteria: the distance between the detection coils, 4 cm, the amplitude of the DC measurements, typically 1 cm. With those considerations, sample holders of 6 cm in length should be sufficient for achieving low background.

However, the length of the sample holder is limited for the usage of Helium-3 system as shown in Fig. A.3. It is advisable to have the sample approximately in the center of the cold finger to avoid background signals from the thermometer and the end of the cold finger.

A suprasil quartz was used to produce the sample holders with the following dimensions $47 \times 4 \times 0.5$ mm^3 as shown in Fig. A.1 bottom. This type of quartz was chosen as it has the smallest amount of iron and other impurities. The sample would be deposited by drop-casting nanoliter-sized droplets of toluene solution in the center of the suprasil. The deposited molecules are then covered with a 4 mm wide kapton tape to keep them in place. More about sample preparation is discussed in the Appendix B.

However, using kapton as a capping should be used with caution. As demonstrated in Fig. A.4, the difference in the thermal expansion constant can cause strain and bending of a 120 μm thick display glass. This is a limiting factor for the thickness

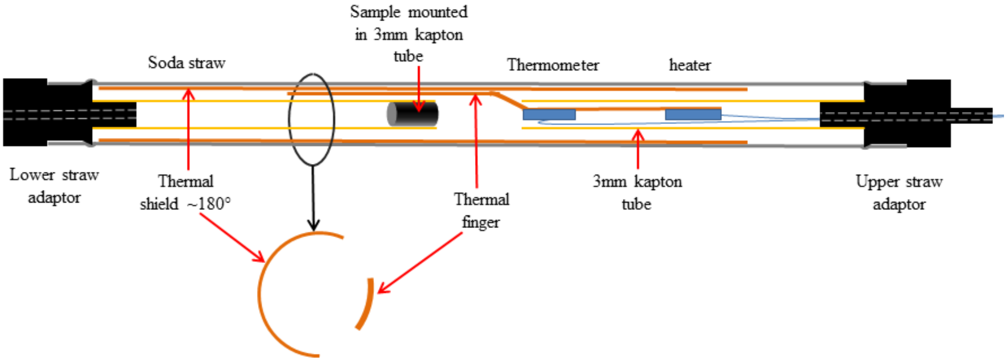

Figure A.3. Schematic representation of the sample region for Helium-3 measurement system. The sample should be located ≈ 25 mm away from the thermometer to reduce the magnetic background of the thermometer, and the thermal finger should extend ≈ 20 mm past the sample. The heater is ≈ 20 mm above the thermometer. Thermal finger keeps the similar temperature for the sample and the thermometer. Schematics from the users manual of the iHelium3 system [77]

of the sample holder. Also, it could result in detaching of the tape and loss of the sample.

Figure A.2 left shows the measured signal of the detection coils when a point paramagnetic sample is scanned through the entire length of the sample transport's vertical path. The center of the main peak indicates the position of the sample. At a certain distance from the center, a paramagnetic sample can show a negative signal due to the properties of the detection coils.

Figure A.2 right shows the centering scans of a 47 mm long suprasil quartz sample holder at an applied field of $\mu_0 H = 0.3$ T and the plastic powder sample holder measured at $\mu_0 H = 0.2$ T and multiplied by a factor of 1.5 to compensate for the field difference. Centering scans of the plastic holder at different applied magnetic fields (Fig. A.5) demonstrate roughly linear dependence on the field. Both measurements were performed at 1.8 K.

Figure A.5 shows the magnetization curves for the plastic powder sample holder at 1.8, 4.5 and 8 K and the 47 mm long suprasil quartz holder at 1.8 K. The plastic

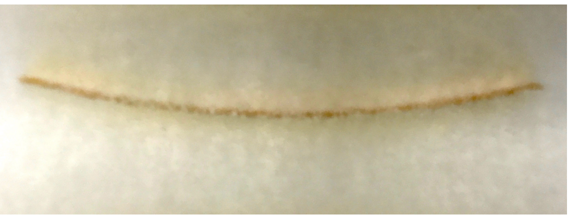

Figure A.4. Bending induced due to the shrinking kapton tape on a thin display glass in liquid nitrogen.

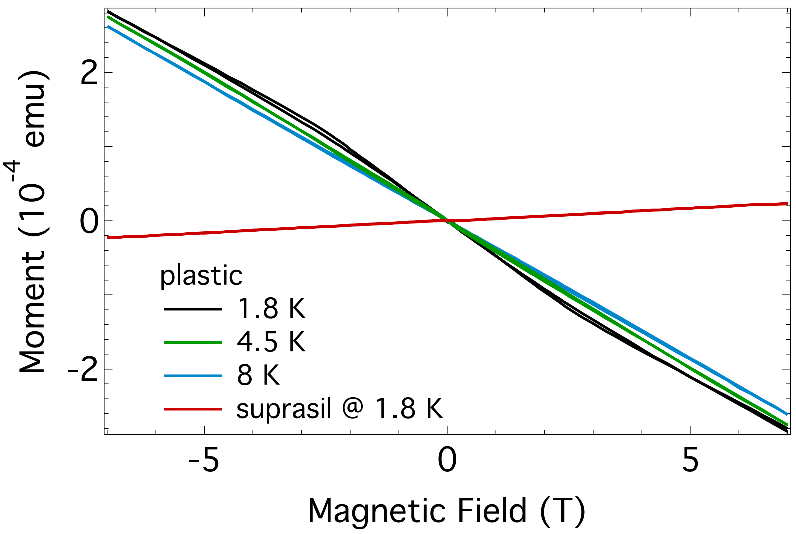

Figure A.5. Magnetization curves for plastic powder sample holder at 1.8, 4.5 and 8 K and suprasil glass with dimensions 47x4x0.5 mm^3 at 1.8 K. Powder sample holder shows a diamagnetic response with a temperature dependent impurities. Suprasil quartz allows the reduction of the background magnetic signal by a factor of 10.

sample holder demonstrates relatively strong diamagnetic signal with a presence of paramagnetic impurities. The impurities deviate the magnetic response of the plastic holder from being linear. This deviation is also temperature dependent.

Suprasil quartz allows the reduction of the background by a factor of 10. This is helpful for sensitive measurement. It would allow the measurements of smaller signals with more accuracy. The response of quartz is paramagnetic despite quartz being a diamagnet. The reason for this are the edge effects. The lack of diamagnetic material is detected as a paramagnetic signal.

Longer quartz paddles should have more homogeneous response depending on the sample position. The homogeneity is very crucial for background subtraction by measuring the sample holder before deposition of the molecules. As it is not easy to deposit molecules very precisely. From the centering scans in Fig. A.2 it is visible that a deviation of 1 mm can change the magnetic moment of the plastic sample holder as it does not have a homogeneous response from the position.

B. Sample Preparation

Endofullerenes are typically transferred in a solution with toluene. The solubility of C_{60} and C_{70} in toluene are $\approx$ 3 mg/ml and $\approx$ 1.5 mg/ml, respectively with a high chance that the solubility depends on the cage size [78, 79]. Therefore, the solubility of C_{80} in toluene can be estimated at $\approx$ 1 mg/ml. From 1 ml of toluene solution typically 0.3 mg SQUID sample was prepared and for X-Treme, $\approx$ 150 μl of toluene solution was typically used. The SQUID magnetometry and X-Ray absorption measurements are performed on specially prepared samples holders.

B.1. MPMS3

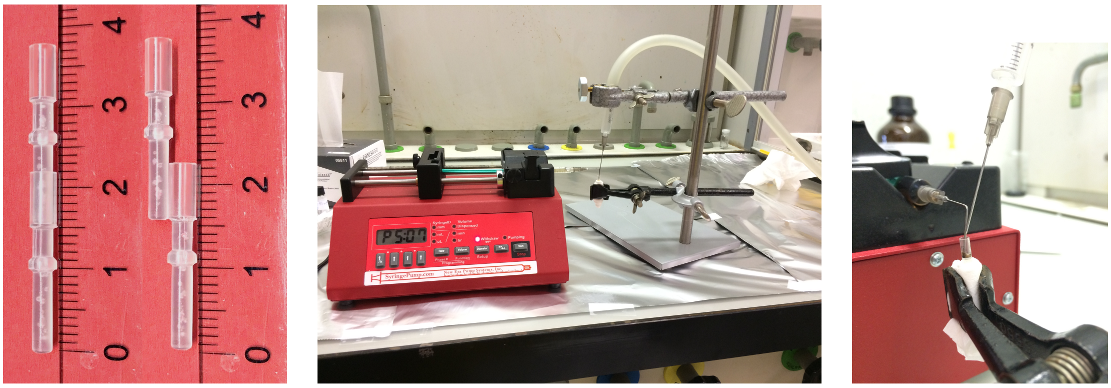

(a) (b) (c)

Figure B.1. (a) The plastic powder sample holder provided by QD. (b) The drop cast system used for sample preparations for SQUID measurements: automated syringe-pump with molecules in a toluene solution filled in a syringe and a nitrogen flow to speed up the evaporation process. The syringe pump was made by New Era Pump Systems Inc., model No: NE-1000. (c) A closer look at the arrangement of the cup part of the sample holder, the needle of a syringe with a molecule solution and the needle for the nitrogen gas.

The SQUID magnetometer used is a Quantum Design (QD) MPMS3 Vibrating Sample Magnetometer (VSM). The sample holders used for this thesis were the plastic powder sample holder [Fig. B.1(a)] provided by QD. The sample holder

Figure B.2. Wetting angle of toluene on a SiO_2 surface 4 ± 1 degree.

consists of two identical pieces. Each of them has a foot at one end and a cup at the other end [Fig. B.1(a) right]. The molecules are deposited in the cup of one of the pieces and covered with the other one as shown in Fig. B.1(a) left.

Figure B.1 shows the deposition system used for sample preparations in this thesis. The molecules were drop-cast from toluene solution into the cup of the sample holder with the help of automated syringe-pump. The deposition process was in steps: the pump did one step, a drop of $\approx 5-7$ μl of the solution, and waited for $\approx 2-3$ min. for the toluene to evaporate before the next drop is deposited. This process leaves the molecules at the bottom and walls of the capsule. The sample preparation was performed under a chemical hood to avoid the inhalation of the toluene vapors. The evaporation process is similar to the coffee stain effect; the liquid evaporates faster from the edges causing a transfer of molecules from the center to the edges and walls of the capsule.

A flow of nitrogen gas was used to speed up the evaporation and thus the deposition process. The evaporation time was decreased from ≈ 20 min to $2-3$ min. The second needle [Fig. B.1 (c)] was used for directing the flow of the nitrogen gas. Typically, the preparation of one sample took two days.

In Appendix A we discussed the development of a new sample holder from suprasil quartz. Figure B.2 shows a droplet of toluene on SiO_2 surface. The wetting angle was estimated to be 4 ± 1 degrees. This limits the droplet size used for drop-casting as the toluene spreads over the surface. If the droplet size is too big, the toluene solution will overflow over the edges of the 4 mm wide quartz holder.

A test with C_{60} was made with an automatic dispensing unit, PipeJet from BioFluidix. Two milliliters of C_{60}/toluene solution was deposited on a SiO_2 surface.

Figure B.3 shows optical microscopy images of the two places where C_{60} was deposited. In the top left panel, the zoomed-out image of the entire sample is shown with the labels indicating higher magnification images shown below. Concentrated areas with many stacking drops are visible next to areas where very few drops overlapped on the same area.

Figure B.3 A1 shows a higher magnification of the low coverage area. Further zooming into the image (Fig. B.3 A2) shows the coffee strain effect of several droplets on top. The edges of which are visible. In Fig. B.3 A3 a trace of a single droplet is visible. This is most likely a monolayer of fullerenes on top of the SiO_2 surface judging from the contrast of covered and uncovered areas and comparing them to those of single-layer graphene. Panels A4a and A4b are the highly concentrated areas of droplets where mountain-like shapes developed.

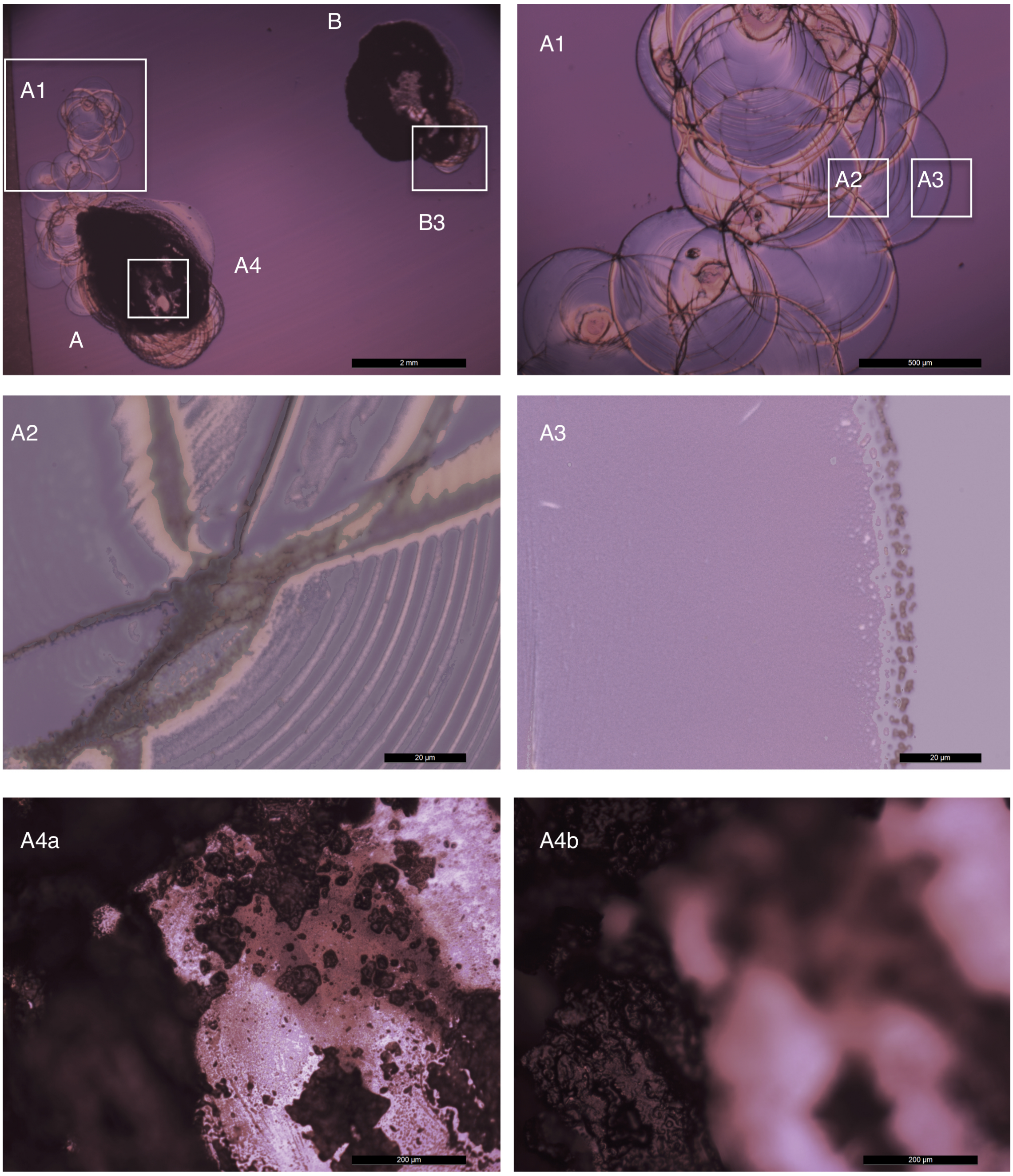

Figure B.3. Optical microscopy images of 2 ml C_{60} deposited on SiO_2 surface with an commercial PipeJet piezo-actuating pump from BioFluidix . Concentrated areas with many stacking drops are visible next to areas where very few drops overlapped on the same area. In panel A3 a monolayer of fullerenes on the surface could be visible.

B.2. X-Treme

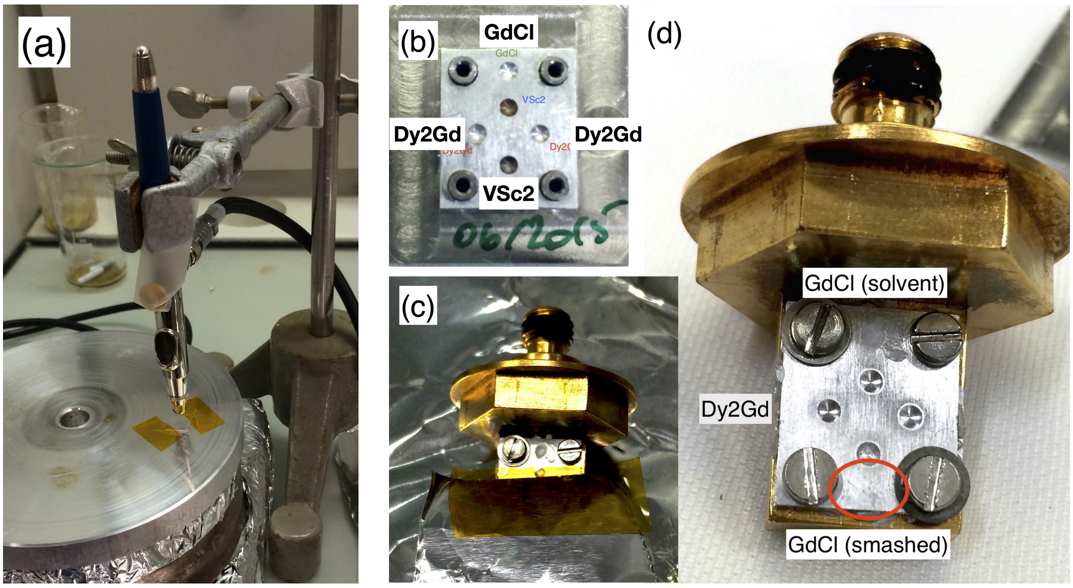

Figure B.4. (a) The use of an airbrush from Harder & Steenbeck fixed on a tripod for spraying the molecules on an aluminum sample holder through a mask. (b) Aluminum sample holder for X-Treme. The dips on the surface allow for deposition of multiple types of molecules through a mask without risk of contamination. (c) Before the drop cast of ethanol solution of $GdCl_3$ on the top dip, the rest of the surface is covered to prevent contamination. (d) The aluminum sample holder mounted on proprietary X-Treme copper sample holder to be introduced into the UHV system.

The aluminum sample holder for X-ray absorption measurements performed at the X-Treme beamline at SLS, PSI is shown in Fig. B.4. Commercial airbrush from Harder & Steenbeck was used to spray the toluene solution of molecules and coat the aluminum sample holder/plate through a mask. Pressurized nitrogen or argon gas was used for the spray-coating. The pre-made dips on the sample plate with a correspondingly marked mask allowed for sample deposition without the risk of contamination.

The sample plate was heated above the boiling temperature of toluene (110.6° C) to prevent the jet of liquid toluene washing already deposited molecules on the surface. At that temperature, each droplet touching the surface was evaporating almost immediately allowing for fast deposition of the molecules.

A thermal paste was used to achieve the lowest temperature for the measurements when mounted on the cold finger for X-ray measurements. The paste, typically silver paste, was applied between the aluminum plate and the copper sample holder to increase the thermal contact.

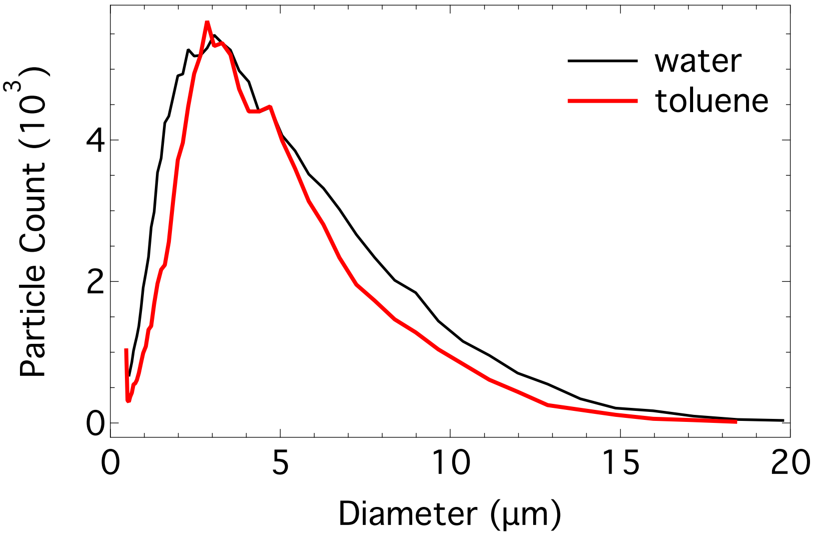

Figure B.5. The particle size distribution sprayed with the airbrush and measured with the APS spectrometer for toluene and water. The measurements were done at the laboratory of Advanced Analytical Technologies, EMPA with the help of Dr. Ari Setyan. The average volume of the sample is 1.4×10^{-17} m^3 = 14 fl.

The pulverization characteristics of the airbrush were studied. Figure B.4 shows the particle size distribution of the pulverized toluene and water (as a comparison) from the airbrush studied with Aerodynamic Particle Sizer 3321 (APS spectrometer) from TSI [80] at the department of Analytical Chemistry, EMPA on June 17, 2014. Pressurized air was used as a gas source.

APS spectrometer provides real-time measurements of particle sizes using two independent methods. Aerodynamic particle size measurements from 0.5 to 20 microns and by the light-scattering intensity in the range of 0.37 to 20 microns.

As seen from the Fig. B.4 both water and toluene show the highest concentration of droplets with the diameter of 3 μm. From this, the volume of liquid in a single droplet can be calculated. The volume of the droplet is 1.4×10^{-14} l = 14 fl (femtoliter). Assuming that the number of C_{60} and C_{80} molecules in 1 fl of toluene is 2.5×10^6, there are 3.5×10^7 molecules in one droplet.

After learning the typical droplet size, we studied the deposited molecules. Figure B.6 shows scanning electron microscopy (SEM) images of $HoSc_2N@C_{80}$ spray-coated with the airbrush on a SiO_2 surface. In the image on the left, patches of monolayer fullerenes are visible with islands of clustered molecules. The scale on shown on the left bottom of the image is 1 μm. The color scale of the image on the right demonstrates what seems to be a layered growth. Steps with different contrast are visible.

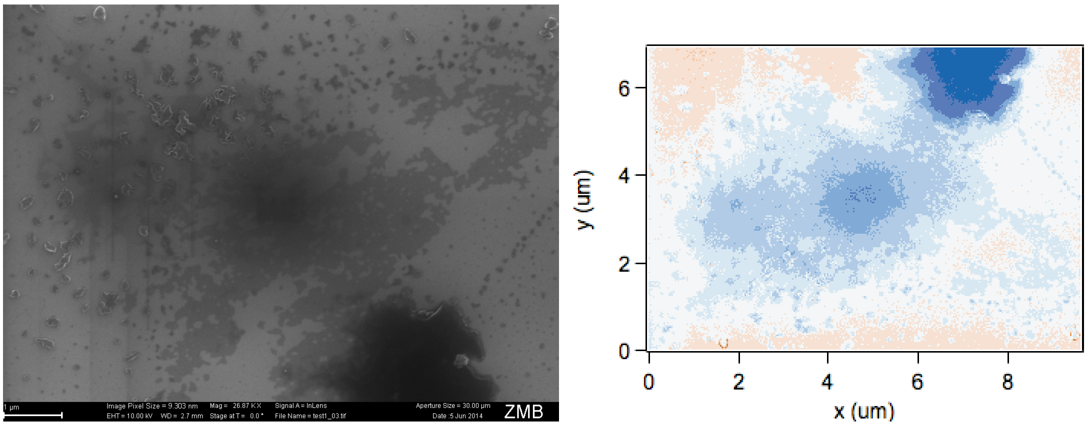

Figure B.6. Left: SEM image of $HoSc_2N@C_{80}$ on a SiO_2 substrate spray-coated from toluene solution. Homogeneous areas, which could be close to a monolayer, with island of multilayer is visible. Right: The color scale demonstrates the layered structure of the spray-coated endofullerenes on the SiO_2.

Figure B.7 shows SEM images of 30 ml $HoLu_2N@C_{80}$ spray coated on aluminum surface with the airbrush. The top left panel is the image of the sample with arrows marking the exact areas of SEM images. Under the fullerenes the stripes of the aluminum surface are visible. On top of that, there are mainly two distinct structures: the flat and thin patches which could be a monolayer of fullerenes on top of the Al and clusters or small spheres of fullerenes glued together. These SEM images are very similar to the structures achieved with spray coating on SiO_2 surface.

The thin monolayer-like patches could be formed from the droplets with smaller diameter while the bigger clusters could be from the droplets of bigger diameter. The effect of coffee stain and clustering inside the droplet could have a larger effect in bigger droplets of toluene.

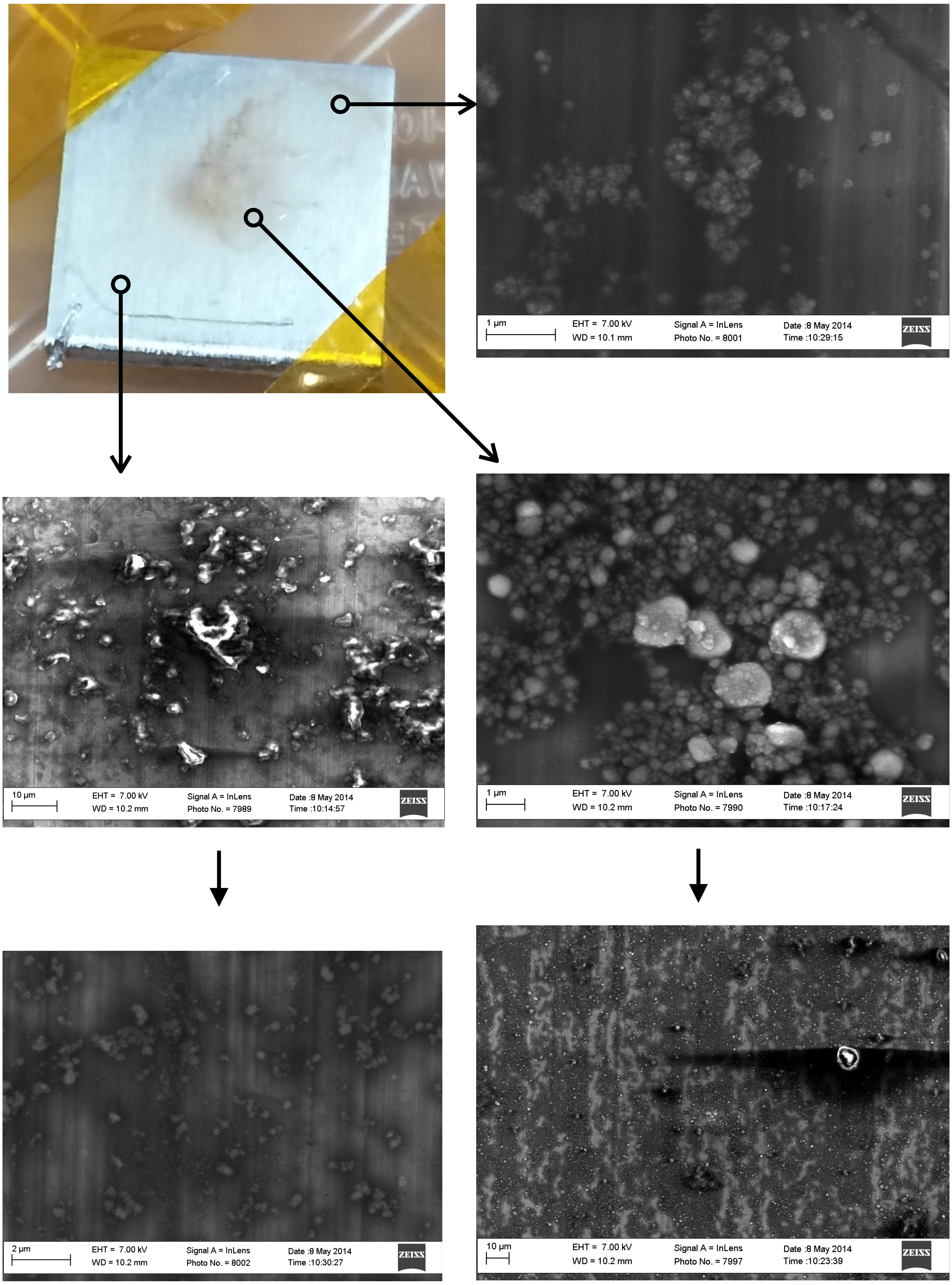

Figure B.7. SEM images of 30 ml of $HoSc_2N@C_{80}$ in toluene solution spray-coated on Al substrate. Arrows show the place on the sample where SEM images are zoomed in. On top of aluminum substrate stripes monolayer and multilayer island of endofullerenes are visible.

C. Calibration of the Magnetic Field Inside the Sample Space

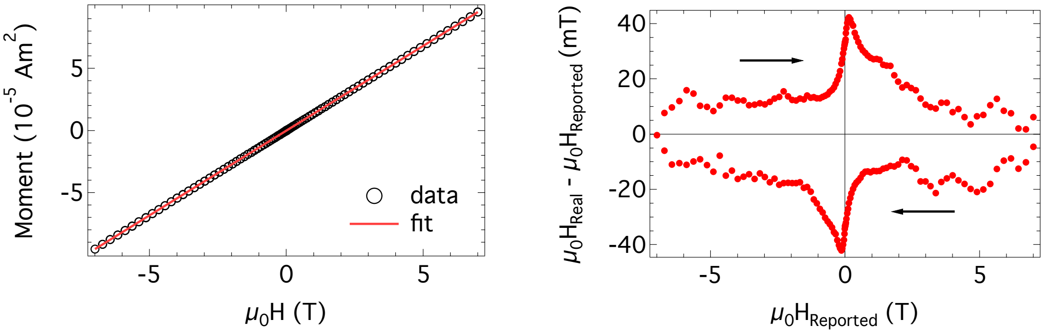

Figure C.1. Left: The magnetization curve of the paramagnetic Pd sample measured at 298 K. The susceptibility of Pd was extracted from the liner fit. Right: The deviation of the reported magnetic field from the real, actual magnetic field sensed by the sample in the sample space. The reported magnetic field is the value shown, reported in the software MultiVu which is calculated from the current values of the power supply. The arrows indicate the field change direction.

The superconducting magnet used in the MPMS3 can generate magnetic fields up to 7 T. The reported magnetic field is calculated from the current flowing through the power supply of the magnet. The actual field experienced by the sample H_{Real} can deviate from the reported field H_{Reported} as much as 40 gausses (4 mT). This error is relevant mainly at small magnetic fields [81].

Two reasons are causing the field error:

1. Magnet remanence: alloys used in the construction of the magnet will permit the magnetic field to enter the superconducting material as threads of quantized magnetic flux when subject to sufficiently large magnetic fields. These flux threads are pinned inside the superconducting material. When the magnetic field is set to zero, some of these flux lines remain and create a small magnetic field.

2. Flux creep and escape: the pinned flux lines will redistribute and drift inside the wire material. At a stable magnetic field value, the flux line drift could cause them

to leave the inside of the wire causing induced currents.

To calibrate the magnetic field inside the sample space a paramagnetic Pd sample provided by Quantum Design was used. It is essential for calibration measurement to perform the same measurement sequence that was used to measure the real sample. The field error depends on the sample history.

The magnetization m of the Pd sample is measured first at 1 T for 5 min and averaged for further calibration purposes ($m(1\ \mathrm{T}) = 1.36246 \times 10^{-5}\ \mathrm{Am}^2$). The magnetic field was set to 1 T by oscillating the field for the best accuracy.

Figure C.1 (a) shows field dependent magnetization of the Pd sample. The average magnetic moment inferred from the linear fit of magnetization $m_{\mathrm{fit}}(1\ \mathrm{T}) = 1.36202 \times 10^{-5}\ \mathrm{Am}^2$ which is slightly different from $m(1\ \mathrm{T})$. The measurements are performed at 298 K.

The real magnetic field felt by the sample in the sample space is calculated by dividing the measured moment m over the $m_{\mathrm{fit}}(1\ \mathrm{T})$. Figure C.1 (b) shows the error of the reported magnetic field. The error is calculated by subtracting the reported magnetic field from the calculated real field.

The error is about 4 mT (40 gausses) at small magnetic fields which decreases at higher field values. The relative error is negligible at high fields. The field error gets critical when near zero field measurements are of interest.

D. Relaxation of the Magnet

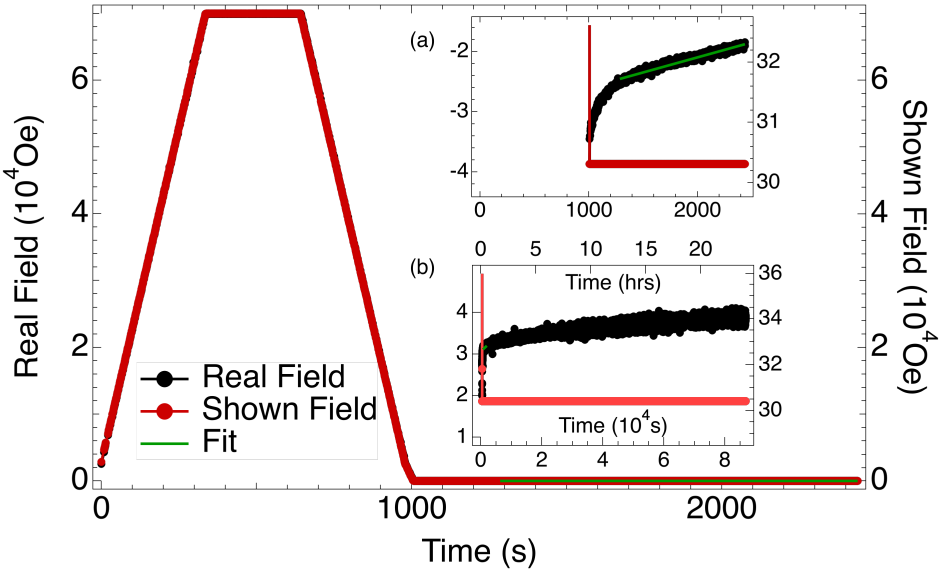

Figure D.1. The real field inside the sample space measured by Pd sample at 298 K by decreasing the saturation or starting field 7 T to 3 mT (30 Oe)—1 T = 10^4 Oe. The real magnetic field is the actual field inside the sample space felt by the sample. The shown magnetic field is the number shown on the MPMS3 software MultiVu. Inset (a): Zoomed part of the graph demonstrates an initial sharp increase of the magnetic field followed by a slow drift. A linear fit to the real field is performed after five minutes of the field stabilization to 30 min. Inset (b): The drift slows down and continues almost linearly for the duration of 24 hours. (The field is shown in Oe instead of T for convenience reasons at small magnetic field values.)

For relaxation measurements, it is essential to know the dependence of the actual magnetic field inside the sample space on the following parameters: the saturation or starting magnetic field B_{st}, the end magnetic field B_{end} and the rate of the field change β. Tests were carried out at 298 K with a Pd sample, provided by QD, which has a linear paramagnetic response. Initially, the magnetic moment $m(1\text{T})$ of Pd was measured at 1 T. Afterward, the measured moment of Pd at different magnetic field values was divided by $m(1\text{T})$ to calculate the actual magnetic field felt by the sample in the sample space.

Figure D.1 shows the measurement sequence where the real field is the actual magnetic field felt by the sample in the sample space. The shown field is the magnetic field value shown on the MPMS3 software MultiVu which is calculated from the current passing through the power supply of the magnet. More details about this issue are discussed in Appendix C. The field is increased to the saturation field or starting field B_{st}, where it stays for 5 min to stabilize, Afterwards, the field is decreased with the chosen field sweep rate β to its end value B_{end} while measuring the magnetic moment of the Pd sample. B_{end} is entered into the software of the magnet.

The inset (a) of the Fig. D.1 demonstrates the behavior of the magnet after the field was stabilized at 3 mT (30 Oe), it exhibits a sharp increase followed by slow up drift which continues for a long time [Fig. D.1 inset (b)] with more details is discussed in the Application Note from Quantum Design [81].

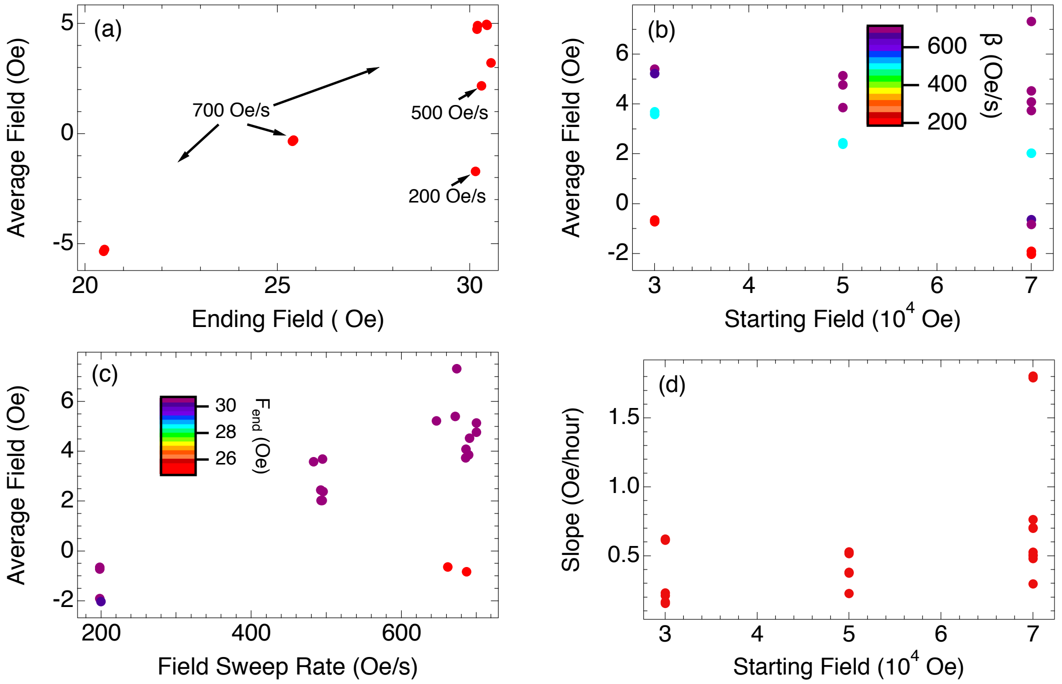

Figure D.2. (a) The average magnetic field between the period of 5 min and 30 min B_{avg} after stabilization of the magnetic field vs the ending field B_{end} or the field that the machine was programmed to ramp down. The two points outside of the linear trend have different field sweep rates. (b) Dependence of the B_{avg} on the starting magnetic field B_{st}. (c) B_{avg} shows a linear trend from the field sweep rate β. The two off values have different B_{end} values as seen in the color scale. (d) The magnetic field drift speed vs the starting field B_{st}. Mostly, the drift is smaller than 0.5 Oe/hour during the first 30 min, and it will slow down even more as seen in Fig. D.1 (b).

A fit is performed on the measured magnetization of the Pd [Fig. D.1 inset (a), green line] starting from five minutes to 30 min after the field is stabilized. Figure D.2 (a) shows the average field B_{avg} during the above mentioned 25 minutes vs the ending field B_{end}. The B_{end} is the value set in the software of the MPMS3 to which it will ramp down from the starting field B_{st}. Most of the data points were measured with field sweep rate β of 700 Oe/s (70 mT/s) but those few points that have different β are labeled with their corresponding β of 500 Oe/s and 200 Oe/s. For the same field sweep rate β a linear dependence of the average field from the ending field is seen.

Figure D.2 (b) shows the B_{avg} vs B_{st} with the color scale showing the speed of the field change in Oe/s. There is no clear dependence of the B_{avg} on the B_{st} but some dependence can be noticed from β.

Figure D.2 (c) shows the dependence of B_{avg} from the field sweep rate beta. From the graph we suppose it to be a linear dependence. The two off points from the primary trend had a different B_{end} value difference from which was demonstrated in the subfigure (a).

The slope of the fit from Fig. D.1 (a) determines the drift speed of the magnetic field. Figure D.2 (d) shows the slope in Oe/h. As seen from the figure the drift is typically slower than 0.5 Oe per hour. This number will slow down over time and as seen in Fig. D.1 (b) over 24 hours the drift was less than 1 Oe.

Bibliography

[1] G. E. Moore, *Craming more components onto integrated circuits*, Electronics **38**, 114–117 (1965).

[2] M. M. Waldrop, *The chips are down for Moore's law*, Nature **530**, 144–147 (2016).

[3] D. Gatteschi, R. Sessoli, and J. Villain, *Molecular Nanomagnets* (Oxford University Press, 2006).

[4] A. Caneschi, D. Gatteschi, R. Sessoli, A. L. Barra, L. C. Brunei, and M. Guillot, *Alternating Current Susceptibility, High Field Magnetization, and Millimeter Band EPR Evidence for a Ground* $S=10$ *State in* $[Mn_{12}O_{12}(CH_3COO)_{16}(H_2O)_4]\cdot 2CH_3COOH\cdot 4H_2O$, J. Am. Chem. Soc. **113**, 5873–5874 (1991).

[5] R. Sessoli, D. Gatteschi, H. L. Tsai, D. N. Hendrickson, A. R. Schake, S. Wang, J. B. Vincent, G. Christou, and K. Folting, *High-Spin Molecules:* $[Mn_{12}O_{12}(O_2CR)_{16}(H_2O)_4]$, J. Am. Chem. Soc. **115**, 1804–1816 (1993).

[6] R. Sessoli, D. Gatteschi, A. Caneschi, and M. A. Novak, *Magnetic bistability in a metal-ion cluster*, Nature **365**, 141–143 (1993).

[7] S. M. Aubin, M. W. Wemple, D. M. Adams, H. L. Tsai, G. Christou, and D. N. Hendrickson, *Distorted* $Mn^{IV}Mn_3^{III}$ *cubane complexes as single-molecule magnets*, J. Am. Chem. Soc. **118**, 7746–7754 (1996).

[8] J. R. Friedman, M. P. Sarachik, J. Tejada, and R. Ziolo, *Macroscopic measurement of resonant magnetization tunneling in high-spin molecules*, Phys. Rev. Lett. **76**, 3830–3833 (1996).

[9] P. Shor, *Algorithms for quantum computation: discrete logarithms and factoring*, Proc. 35th Annu. Symp. Found. Comput. Sci. , 124–134 (1994).

[10] L. K. Grover, *Quantum Computers Can Search Arbitrarily Large Databases by a Single Query*, Phys. Rev. Lett. **79**, 4709–4712 (1997).

[11] M. N. Leuenberger and D. Loss, *Quantum computing in molecular magnets*, Nature **410**, 789–793 (2001).

[12] A. Ekert and R. Jozsa, *Quantum computation and Shor's factoring algorithm*, Rev. Mod. Phys. **68**, 733–753 (1996).

[13] J. Ahn, T. C. Weinacht, and P. H. Bucksbaum, *Information Storage and Retrieval Through Quantum Phase*, Science **287**, 463–465 (2000).

[14] B. Lapo and W. Wolfgang, *Molecular spintronics using single- molecule magnets*, Nat. Mater. **7**, 179 (2008).

[15] J. R. Heath, S. C. O'Brien, Q. Zhang, Y. Liu, R. F. Curl, F. K. Tittel, and R. E. Smalley, *Lanthanum complexes of spheroidal carbon shells*, J. Am. Chem. Soc. **107**, 7779–7780 (1985).

[16] Y. Chai, T. Guo, C. Jin, R. E. Haufler, L. P. Chibante, J. Fure, L. Wang, J. M. Alford, and R. E. Smalley, *Fullerenes with metals inside*, J. Phys. Chem. **95**, 7564–7568 (1991).

[17] H. W. Kroto, J. R. Heath, S. C. O'Brien, R. F. Curl, and R. E. Smalley, *C_{60}: Buckminsterfullerene*, Nature **318**, 162–163 (1985).

[18] J. Zhang, S. Stevenson, and H. C. Dorn, *Trimetallic Nitride Template Endohedral Metallofullerenes: Discovery, Structural Characterization, Reactivity, and Applications*, Acc. Chem. Res. **46**, 1548–1557 (2013).

[19] L. Dunsch and S. Yang, *Metal Nitride Cluster Fullerenes: Their Current State and Future Prospects*, Small **3**, 1298–1320 (2007).

[20] M. N. Chaur, F. Melin, A. L. Ortiz, and L. Echegoyen, *Chemical, Electrochemical, and Structural Properties of Endohedral Metallofullerenes*, Angew. Chemie Int. Ed. **48**, 7514–7538 (2009).

[21] M. Wolf, K.-H. Müller, D. Eckert, Y. Skourski, P. Georgi, R. Marczak, M. Krause, and L. Dunsch, *Magnetic moments in $Ho_3N@C_{80}$ and $Tb_3N@C_{80}$*, J. Magn. Magn. Mater. **290-291**, 290–293 (2005).

[22] L. F. Chibotaru and L. Ungur, *Ab initio calculation of anisotropic magnetic properties of complexes. I. Unique definition of pseudospin Hamiltonians and their derivation*, J. Chem. Phys. **137**, 064112 (2012).

[23] R. Westerström, J. Dreiser, C. Piamonteze, M. Muntwiler, S. Weyeneth, H. Brune, S. Rusponi, F. Nolting, A. Popov, S. Yang, L. Dunsch, and T. Greber, *An Endohedral Single-Molecule Magnet with Long Relaxation Times:* $DySc_2N@C_{80}$, J. Am. Chem. Soc. **134**, 9840–9843 (2012).

[24] R. Westerström, J. Dreiser, C. Piamonteze, M. Muntwiler, S. Weyeneth, K. Krämer, S.-X. Liu, S. Decurtins, A. Popov, S. Yang, L. Dunsch, and T. Greber, *Tunneling, remanence, and frustration in dysprosium-based endohedral single-molecule magnets*, Phys. Rev. B **89**, 060406 (2014).

[25] A. A. Popov, S. Yang, and L. Dunsch, *Endohedral Fullerenes*, Chem. Rev. **113**, 5989–6113 (2013).

[26] R. D. Johnson, M. S. de Vries, J. Salem, D. S. Bethune, and C. S. Yannoni, *Electron paramagnetic resonance studies of lanthanum-containing* C_{82}, Nature **355**, 239–240 (1992).

[27] H. Funasaka, K. Yamamoto, K. Sakurai, T. Ishiguro, K. Sugiyama, T. Takahashi, and Y. Kishimoto, *Preparation of Fullerene Derivatives by Resistive Heating With Graphite Crucible*, Fuller. Sci. Technol. **1**, 437–448 (1993).

[28] M. Jansen, G. Peters, and N. Wagner, *Zur Bildung von Fullerenen und endohedralen Metallofullerenen: Darstellung im Hochfrequenzofen*, Zeitschrift für Anorg. und Allg. Chemie **621**, 689–693 (1995).

[29] K. Yoshie, S. Kasuya, K. Eguchi, and T. Yoshida, *Novel method for* C_{60} *synthesis: A thermal plasma at atmospheric pressure*, Appl. Phys. Lett. **61**, 2782–2783 (1992).

[30] Y. Rubin, *Organic Approaches to Endohedral Metallofullerenes: Cracking Open or Zipping Up Carbon Shells?*, Chem. - A Eur. J. **3**, 1009–1016 (1997).

[31] W. Krätschmer, L. D. Lamb, K. Fostiropoulos, and D. R. Huffman, *Solid* C_{60}*: a new form of carbon*, Nature **347**, 354–358 (1990).

[32] H. Shinohara, H. Yamaguchi, N. Hayashi, H. Sato, M. Inagaki, Y. Saito, S. Bandow, H. Kitagawa, T. Mitani, and H. Inokuchi, *A new characterization*

of lanthanum- and scandium-endohedral metallofullerenes, Mater. Sci. Eng. B **19**, 25–30 (1993).

[33] *Quantum Design, Inc., www.qdusa.com* (2018).

[34] R. L. Fagaly, *Superconducting quantum interference device instruments and applications*, Rev. Sci. Instrum. **77**, 101101 (2006).

[35] C. Gorter and F. Brons, *Magnetic inhibition of susceptibilities at radio frequencies*, Physica **4**, 579–584 (1937).

[36] H. Casimir and F. du Pré, *Note on the thermodynamic interpretation of paramagnetic relaxation phenomena*, Physica **5**, 507–511 (1938).

[37] K. S. Cole and R. H. Cole, *Dispersion and Absorption in Dielectrics I. Alternating Current Characteristics*, J. Chem. Phys. **9**, 341–351 (1941).

[38] P. Carra, B. T. Thole, M. Altarelli, and X. Wang, *X-ray circular dichroism and local magnetic fields*, Phys. Rev. Lett. **70**, 694–697 (1993).

[39] B. T. Thole, P. Carra, F. Sette, and G. van der Laan, *X-ray circular dichroism as a probe of orbital magnetization*, Phys. Rev. Lett. **68**, 1943–1946 (1992).

[40] Y. Teramura, A. Tanaka, B. T. Thole, and T. Jo, *Effect of Coulomb Interaction on the X-Ray Magnetic Circular Dichroism Spin Sum Rule in Rare Earths*, J. Phys. Soc. Japan **65**, 3056–3059 (1996).

[41] J. Stohr and H. C. Siegmann, *Magnetism* (Springer Berlin Heidelberg, 2006).

[42] C. Piamonteze, U. Flechsig, S. Rusponi, J. Dreiser, J. Heidler, M. Schmidt, R. Wetter, M. Calvi, T. Schmidt, H. Pruchova, J. Krempasky, C. Quitmann, H. Brune, and F. Nolting, *X-Treme beamline at SLS: X-ray magnetic circular and linear dichroism at high field and low temperature*, J. Synchrotron Radiat. **19**, 661–674 (2012).

[43] M. Berger, J. Hubbell, S. Seltzer, J. Chang, J. Coursey, R. Sukumar, D. Zucker, and K. Olsen, *XCOM: Photon Cross Section Database, National Institute of Standards and Technology, Gaithersburg, MD.*

[44] J. Kanamori, *4 - Anisotropy and Magnetostriction of Ferromagnetic and Antiferromagnetic Materials - Rado, George T.*, in *Magnetism*, edited by H. B. T. M. Suhl (Academic Press, 1963) pp. 127–203.

[45] C. P. Poole and H. A. Farach, *Handbook of electron spin resonance* (New York (N.Y.): American institute of physics, 1994).

[46] J. M. Zadrozny, M. Atanasov, A. M. Bryan, C.-Y. Lin, B. D. Rekken, P. P. Power, F. Neese, and J. R. Long, *Slow magnetization dynamics in a series of two-coordinate iron(II) complexes*, Chem. Sci. **4**, 125–138 (2013).

[47] A. Amjad, A. Figuerola, A. Caneschi, and L. Sorace, *Multiple Magnetization Reversal Channels Observed in a 3d-4f Single Molecule Magnet*, Magnetochemistry **2**, 27 (2016).

[48] E. Lucaccini, L. Sorace, M. Perfetti, J.-P. Costes, and R. Sessoli, *Beyond the anisotropy barrier: slow relaxation of the magnetization in both easy-axis and easy-plane Ln(trensal) complexes*, Chem. Commun. **50**, 1648–1651 (2014).

[49] L. Thomas, A. Caneschi, and B. Barbara, *Nonexponential Dynamic Scaling of the Magnetization Relaxation in* Mn_{12} *Acetate*, Phys. Rev. Lett. **83**, 2398–2401 (1999).

[50] J. H. Van Vleck, *Paramagnetic Relaxation Times for Titanium and Chrome Alum*, Phys. Rev. **57**, 426–447 (1940).

[51] C. B. P. Finn, R. Orbach, and W. P. Wolf, *Spin-Lattice Relaxation in Cerium Magnesium Nitrate at Liquid Helium Temperatures: a New Process*, Proc. Phys. Soc. **77**, 1223–1223 (1961).

[52] A. A. Manenkov and A. M. Prokhorov, *TEMPERATURE DEPENDENCE OF SPIN-LATTICE RELAXATION TIMES*, J. Exptl. Theor. Phys. **15**, 951–953 (1962).

[53] R. J. Blagg, L. Ungur, F. Tuna, J. Speak, P. Comar, D. Collison, W. Wernsdorfer, E. J. L. McInnes, L. F. Chibotaru, and R. E. P. Winpenny, *Magnetic relaxation pathways in lanthanide single-molecule magnets*, Nat. Chem. **5**, 673–678 (2013).

[54] A. Fort, A. Rettori, J. Villain, D. Gatteschi, and R. Sessoli, *Mixed Quantum-Thermal Relaxation in* Mn_{12} *Acetate Molecules*, Phys. Rev. Lett. **80**, 612–615 (1998).

[55] A. Abragam and B. Bleaney, *Electron Paramagnetic Resonance of Transition Ions* (CLARENDON PRESS, 1970).

[56] R. Orbach, *Spin-Lattice Relaxation in Rare-Earth Salts*, Proc. R. Soc. A Math. Phys. Eng. Sci. **264**, 458–484 (1961).

[57] R. Orbach, *Spin-Lattice Relaxation in Rare-Earth Salts: Field Dependence of the Two-Phonon Process*, Proc. R. Soc. A Math. Phys. Eng. Sci. **264**, 485–495 (1961).

[58] M. Blume and R. Orbach, *Spin-Lattice Relaxation of S-State Ions:* Mn^{2+} *in a Cubic Environment*, Phys. Rev. **127**, 1587–1592 (1962).

[59] A. Kostanyan, R. Westerström, Y. Zhang, D. Kunhardt, R. Stania, B. Büchner, A. A. Popov, and T. Greber, *Switching Molecular Conformation with the Torque on a Single Magnetic Moment*, Phys. Rev. Lett. **119**, 237202 (2017).

[60] Y. Zhang, D. Krylov, S. Schiemenz, M. Rosenkranz, R. Westerström, J. Dreiser, T. Greber, B. Büchner, and A. A. Popov, *Cluster-size dependent internal dynamics and magnetic anisotropy of Ho ions in* $HoM_2N@C_{80}$ *and* $Ho_2MN@C_{80}$ *families (M = Sc, Lu, Y)*, Nanoscale **6**, 11431–11438 (2014).

[61] V. Vieru, L. Ungur, and L. F. Chibotaru, *Key Role of Frustration in Suppression of Magnetization Blocking in Single-Molecule Magnets*, J. Phys. Chem. Lett. **4**, 3565–3569 (2013).

[62] F. Liu, C.-L. Gao, Q. Deng, X. Zhu, A. Kostanyan, R. Westerström, S. Wang, Y.-Z. Tan, J. Tao, S.-Y. Xie, A. A. Popov, T. Greber, and S. Yang, *Triangular Monometallic Cyanide Cluster Entrapped in Carbon Cage with Geometry-Dependent Molecular Magnetism*, J. Am. Chem. Soc. **138**, 14764–14771 (2016).

[63] F. Liu, S. Wang, C.-L. Gao, Q. Deng, X. Zhu, A. Kostanyan, R. Westerström, F. Jin, S.-Y. Xie, A. A. Popov, T. Greber, and S. Yang, *Mononuclear Clusterfullerene Single-Molecule Magnet Containing Strained Fused-Pentagons Stabilized by a Nearly Linear Metal Cyanide Cluster*, Angew. Chemie Int. Ed. **56**, 1830–1834 (2017).

[64] T. Heine, K. Vietze, and G. Seifert, ^{13}*C NMR fingerprint characterizes long time-scale structure of* $Sc_3N@C_{80}$ *endohedral fullerene*, Magn. Reson. Chem. **42**, S199–S201 (2004).

[65] A. A. Popov and L. Dunsch, *Hindered Cluster Rotation and* ^{45}*Sc Hyperfine Splitting Constant in Distonoid Anion Radical* $Sc_3N@C_{80}^{-}$*, and Spatial Spin-Charge Separation as a General Principle for Anions of Endohedral Fullerenes*

with Metal-Localized Lowest Unoccupied M, J. Am. Chem. Soc. **130**, 17726–17742 (2008).

[66] J. Dreiser, R. Westerström, Y. Zhang, A. A. Popov, L. Dunsch, K. Krämer, S.-X. Liu, S. Decurtins, and T. Greber, *The Metallofullerene Field-Induced Single-Ion Magnet* $HoSc_2N@C_{80}$, Chem. - A Eur. J. **20**, 13536–13540 (2014).

[67] R. Stania, *Nanotemplates and Conformations of Tri-Metal Endofullerenes on Surfaces*, Ph.D. thesis, Universität Zürich (2016).

[68] P. A. Heiney, J. E. Fischer, A. R. McGhie, W. J. Romanow, A. M. Denenstein, J. P. McCauley Jr., A. B. Smith, and D. E. Cox, *Orientational ordering transition in solid* C_{60}, Phys. Rev. Lett. **66**, 2911–2914 (1991).

[69] R. D. Shannon, *Revised effective ionic radii and systematic studies of interatomic distances in halides and chalcogenides*, Acta Crystallogr. Sect. A **32**, 751–767 (1976).

[70] L. Ungur, J. J. Leroy, I. Korobkov, M. Murugesu, and L. F. Chibotaru, *Fine-tuning the local symmetry to attain record blocking temperature and magnetic remanence in a single-ion magnet*, Angew. Chemie - Int. Ed. **53**, 4413–4417 (2014).

[71] J. Dreiser, R. Westerström, C. Piamonteze, F. Nolting, S. Rusponi, H. Brune, S. Yang, A. Popov, L. Dunsch, and T. Greber, *X-ray induced demagnetization of single-molecule magnets*, Appl. Phys. Lett. **105**, 032411 (2014).

[72] R. Westerström, A.-C. Uldry, R. Stania, J. Dreiser, C. Piamonteze, M. Muntwiler, F. Matsui, S. Rusponi, H. Brune, S. Yang, A. Popov, B. Büchner, B. Delley, and T. Greber, *Surface Aligned Magnetic Moments and Hysteresis of an Endohedral Single-Molecule Magnet on a Metal*, Phys. Rev. Lett. **114**, 087201 (2015).

[73] S.-D. Jiang, B.-W. Wang, H.-L. Sun, Z.-M. Wang, and S. Gao, *An Organometallic Single-Ion Magnet*, J. Am. Chem. Soc. **133**, 4730–4733 (2011).

[74] Y. Zhang, D. Krylov, M. Rosenkranz, S. Schiemenz, and A. A. Popov, *Magnetic anisotropy of endohedral lanthanide ions: paramagnetic NMR study of* $MSc_2N@C_{80}$-I_h *with M running through the whole 4f row*, Chem. Sci. **6**, 2328–2341 (2015).

[75] F. L. Pratt, E. Micotti, P. Carretta, A. Lascialfari, P. Arosio, T. Lancaster, S. J. Blundell, and A. K. Powell, *Dipolar ordering in a molecular nanomagnet detected using muon spin relaxation*, Phys. Rev. B **89**, 144420 (2014).

[76] M. A. Garcia, E. Fernandez Pinel, J. de la Venta, A. Quesada, V. Bouzas, J. F. Fernández, J. J. Romero, M. S. Martín González, and J. L. Costa-Krämer, *Sources of experimental errors in the observation of nanoscale magnetism*, J. Appl. Phys. **105**, 013925 (2009).

[77] *User guide, iHelium for MPMS3*, QUANTUM DESIGN JAPAN (March 15, 2016).

[78] X. Zhou, J. Liu, Z. Jin, Z. Gu, Y. Wu, and Y. Sun, *Solubility of Fullerene C_{60} and C_{70} in Toluene, o-Xylene and Carbon Disulfide at Various Temperatures*, Fuller. Sci. Technol. **5**, 285–290 (1997).

[79] R. S. Ruoff, D. S. Tse, R. Malhotra, and D. C. Lorents, *Solubility of fullerene C_{60} in a variety of solvents*, J. Phys. Chem. **97**, 3379–3383 (1993).

[80] *TSI particle sizer, www.tsi.com* (2014).

[81] *Application Note 1500-011, Using SQUID VSM Superconducting Magnets at Low Fields*, Quantum Design (1 May 2010).

[82] S. M. Avdoshenko, F. Fritz, C. Schlesier, A. Kostanyan, J. Dreiser, M. Luysberg, A. A. Popov, C. Meyer, and R. Westerström, *Partial magnetic ordering in one-dimensional arrays of endofullerene single-molecule magnet peapods*, Nanoscale (2018).

[83] C. Schlesier, L. Spree, A. Kostanyan, R. Westerström, A. Brandenburg, A. U. B. Wolter, S. Yang, T. Greber, and A. A. Popov, *Strong carbon cage influence on the single molecule magnetism in Dy–Sc nitride clusterfullerenes*, Chem. Commun. **54**, 9730–9733 (2018).

[84] F. Fritz, R. Westerström, A. Kostanyan, C. Schlesier, J. Dreiser, B. Watts, L. Houben, M. Luysberg, S. M. Avdoshenko, A. A. Popov, C. M. Schneider, and C. Meyer, *Nanoscale x-ray investigation of magnetic metallofullerene peapods*, Nanotechnology **28**, 435703 (2017).

[85] F. Liu, D. S. Krylov, L. Spree, S. M. Avdoshenko, N. A. Samoylova, M. Rosenkranz, A. Kostanyan, T. Greber, A. U. B. Wolter, B. Büchner, and

A. A. Popov, *Single molecule magnet with an unpaired electron trapped between two lanthanide ions inside a fullerene*, Nat. Commun. **8**, 16098 (2017).

[86] C.-H. Chen, D. S. Krylov, S. M. Avdoshenko, F. Liu, L. Spree, R. Yadav, A. Alvertis, L. Hozoi, K. Nenkov, A. Kostanyan, T. Greber, A. U. B. Wolter, and A. A. Popov, *Selective arc-discharge synthesis of* Dy_2S*-clusterfullerenes and their isomer-dependent single molecule magnetism*, Chem. Sci. **8**, 6451–6465 (2017).

[87] D. A. Zanin, L. G. De Pietro, Q. Peter, A. Kostanyan, H. Cabrera, A. Vindigni, T. Bähler, D. Pescia, and U. Ramsperger, *Thirty per cent contrast in secondary-electron imaging by scanning field-emission microscopy*, Proc. R. Soc. A Math. Phys. Eng. Sci. **472**, 20160475 (2016).

[88] K. Junghans, C. Schlesier, A. Kostanyan, N. A. Samoylova, Q. Deng, M. Rosenkranz, S. Schiemenz, R. Westerström, T. Greber, B. Büchner, and A. A. Popov, *Methane as a Selectivity Booster in the Arc-Discharge Synthesis of Endohedral Fullerenes: Selective Synthesis of the Single-Molecule Magnet* $Dy_2TiC@C_{80}$ *and Its Congener* $Dy_2TiC_2@C_{80}$, Angew. Chemie Int. Ed. **54**, 13411–13415 (2015).

Acknowledgements

In the following, I would like to express my gratitude to every person which contributed or supported me along the long journey of this PhD. The greatest gratitude goes to my supervisor Prof. Dr. Thomas Greber for the opportunity and his expertise in the collaboration of the project and to Prof. Dr. Jürg Osterwalder for the support from the research group. Rasmus Westerström for the constructive and help along the way and for the lovely illustrations, Cinthia Piamonteze for the essential support and advice during beamtimes and analysis of the XAS and XMCD data and Andrey Zheludev for the guidance and his time as a PhD committee member.

Special thanks to the research group of IFW Dresden, Alexey Popov for the novel materials and the fruitful discussions, Denis Krylov and Stanislav Avdoshenko for involving discussions and Christin Schlesier for the hard work in the synthesis of the molecules.

From the Osterwalder Group of the University of Zürich special thanks go to Carlo Bernard, Roland Stania, Adrian Schuler and Wolf-Dietrich Zabka for the help along the way, beamtime support, and with the German parts of the thesis. Also thanks to Thomas Kälin and the mechanical workshop.

Finally, of course, a great thank you to my family, cousins, and friends for their kind support along the way.

Curriculum Vitae

Name: Aram Kostanyan

Birth: 13.04.1990 in Yerevan, Armenia

Education

4/2014 – 3/2018	PhD in experimental Physics University of Zürich, Switzerland Group of Prof. Dr. J. Osterwalder and Prof. Dr. T. Greber, in collaboration with Paul Scherrer Institute (PSI)—Swiss Lightsource (SLS) Dr. Cinthia Piamonteze PhD thesis: ”C_{80} Endohedral Fullerenes: Rearranging Atoms in a Magnetic Field and Exploring the Interplay of their Spins with Subkelvin Magnetometry and X-rays”
9/2011 – 2/2014	Master of Science in Physics ETH Zürich, Switzerland MSc thesis: ”Lateral Resolution of Near Field-Emission Scanning Electron Microscope (NFESEM): Tip-Sample distance dependence”
9/2006 – 6/2011	Bachelor of Science in Physics Yerevan State University, Yerevan, Armenia
8/2008 – 5/2009	Global UGRAD, IREX—Exchange Program, major in Physics Roanoke College, Salem, Virginia, USA

Working experience

9/2009 – 9/2011	Senior Laborant, Helliotech Laboratory, Yerevan, Armenia

---

Teaching experience

4/2014 – 3/2018	Teaching assistant University of Zürich, Switzerland Taught lab-courses and problem-solving classes in physics for biology and physics student.

Publications

1. **Partial magnetic ordering in one-dimensional arrays of endofullerene single-molecule magnet peapods**

   Stanislav M. Avdoshenko, Fabian Fritz, Christin Schlesier, Aram Kostanyan, Jan Dreiser, Martina Luysberg, Alexey A. Popov, Carola Meyer, and Rasmus Westerström

   Nanoscale (2018)—published on Aug 2018 [82].

2. **Strong carbon cage influenceon the single molecule magnetism in Dy–Sc nitride clusterfullerenes**

   Christin Schlesier, Lukas Spree, Aram Kostanyan, Rasmus Westerström, Ariane Brandenburg, Anja U. B. Wolter, Shangfeng Yang, Thomas Greber, and Alexey A. Popov

   Chem. Commun. 54, 9730–9733 (2018)—published on Jul, 2018 [83].

3. **Switching Molecular Conformation with the Torque on a Single Magnetic Moment**

   Aram Kostanyan, Rasmus Westerström, Yang Zhang, David Kunhardt, Roland Stania, Bernd Büchner, Alexey A. Popov, and Thomas Greber

   Phys. Rev. Lett. **119**, 237202 (2017) [59].

4. **Nanoscale X-ray investigation of magnetic metallofullerene peapods**

   Fabian Fritz, Rasmus Westerström, Aram Kostanyan, Christin Schlesier, Jan Dreiser, Benjamin Watts, Lothar Houben, Martina Luysberg, Stanislav M. Avdoshenko, Alexey A. Popov, Claus M. Schneider, and Carola Meyer

   Nanotechnology **28**, 435703 (2017) [84].

5. **Single molecule magnet with an unpaired electron trapped between two lanthanide ions inside a fullerene**

   Fupin Liu, Denis S. Krylov, Lukas Spree, Stanislav M. Avdoshenko, Nataliya A. Samoylova, Marco Rosenkranz, Aram Kostanyan, Thomas Greber, Anja U.B. Wolter, Bernd Büchner, and Alexey A. Popov

   Nat. Commun. **8**, 16098 (2017) [85].

6. **Mononuclear Clusterfullerene Single-Molecule Magnet Containing Strained Fused-Pentagons Stabilized by a Nearly Linear Metal Cyanide Cluster**

   Fupin Liu, Song Wang, Cong-Li Gao, Qingming Deng, Xianjun Zhu, Aram Kostanyan, Rasmus Westerström, Fei Jin, Su-Yuan Xie, Alexey A. Popov, Thomas Greber, and Shangfeng Yang

   Angew. Chemie Int. Ed. **56**, 1830–1834 (2017) [63].

7. **Selective arc-discharge synthesis of Dy_2S-clusterfullerenes and their isomer-dependent single molecule magnetism**

   Chia-Hsiang Chen, Denis S. Krylov, Stanislav M. Avdoshenko, Fupin Liu, Lukas Spree, Ravi Yadav, Antonis Alvertis, Liviu Hozoi, Konstantin Nenkov, Aram Kostanyan, Thomas Greber, Anja U. B. Woltera, and Alexey A. Popov

   Chem. Sci. **8**, 6451–6465 (2017) [86].

8. **Thirty per cent contrast in secondary-electron imaging by scanning field-emission microscopy**

   Danilo A. Zanin, Lorenzo G. De Pietro, Q. Peter, Aram Kostanyan, Hugo Cabrera, Alessandro Vindigni, Thomas Bähler, Danilo Pescia, and Urs Ramsperger

   Proc. R. Soc. A Math. Phys. Eng. Sci. **472**, 20160475 (2016) [87].

9. **Triangular monometallic cyanide cluster entrapped in carbon cage with geometry-dependent molecular magnetism**

   Fupin Liu, Cong-Li Gao, Qingming Deng, Xianjun Zhu, Aram Kostanyan, Rasmus Westerström, Song Wang, Yuan-Zhi Tan, Jun Tao, Su-Yuan Xie, Alexey A. Popov, Thomas Greber, and Shangfeng Yang

   J. Am. Chem. Soc. **138**, 14764–14771 (2016) [62].

10. **Methane as a Selectivity Booster in the Arc-Discharge Synthesis of Endohedral Fullerenes: Selective Synthesis of the Single-Molecule Magnet $Dy_2TiC@C_{80}$ and Its Congener $Dy_2TiC_2@C_{80}$**

    Katrin Junghans, Christin Schlesier, Aram Kostanyan, Nataliya A. Samoylova, Qingming Deng, Marco Rosenkranz, Sandra Schiemenz, Rasmus Westerström, Thomas Greber, Bernd Büchner, and Alexey A. Popov

    Angew. Chemie Int. Ed. **54**, 13411–13415 (2015) [88].